Chiral Spin Textures in Magnetic Nanostructures

Risalat Amir Khan

Submitted in accordance with the requirements for the degree of

Doctor of Philosophy

The University of Leeds

School of Physics and Astronomy

June 2018

To my friends
To my teachers
in Leeds, Dhaka, Berlin, and Heidelberg

Intellectual property statement

The candidate confirms that the work submitted is his own, except where work which has formed part of jointly authored publications has been included. The contribution of the candidate and the other authors to this work has been explicitly indicated below. The candidate confirms that appropriate credit has been given within the thesis where reference has been made to the work of others.

The work in Chapter 4 of the thesis has appeared in publication as follows:

R. A. Khan, P. M. Shepley, A. Hrabec, A. W. J. Wells, B. Ocker, C. H. Marrows, and T. A. Moore, "Effect of annealing on the interfacial Dzyaloshinskii-Moriya interaction in Ta/CoFeB/MgO trilayers," Appl. Phys. Lett. **109**, 132404 (2016) (Editor's pick).

- Work attributed to the candidate: design and management of the project, experimental measurements, data analysis and interpretation, and preparation of the manuscript.

- Work attributed to other authors: P. M. Shepley: assistance with data analysis and manuscript editing. A. Hrabec: experimental assists and manuscript editing. A. W. J. Wells: experimental assists. B. Ocker: sample fabrication. C. H. Marrows: management of the project, interpretation, and manuscript reviewing and editing. T. A. Moore: design and management of the project, interpretation, and manuscript reviewing and editing.

The work in Chapters 5 and 6 of the thesis has appeared in publication as follows:

R. A. Khan, H. T. Nembach, M. Ali, J. M. Shaw, C. H. Marrows, and T. A. Moore, "Magnetic domain texture and the Dzyaloshinskii-Moriya interaction in Pt/Co/IrMn and Pt/Co/FeMn thin films with perpendicular exchange bias," Phys. Rev. B. **98**, 064413 (2018).

- Work attributed to the candidate: design and management of the project, sample fabrication and development, experimental measurements, data analysis and interpretation, and preparation of the manuscript.

- Work attributed to other authors: H. T. Nembach: experimental measurements, data analysis, and manuscript editing. M. Ali: experimental assists, data interpretation, and manuscript editing. J. M. Shaw: experimental assists. C. H. Marrows: management of the project, interpretation, and manuscript reviewing and editing. T. A. Moore: design and management of the project, interpretation, and manuscript reviewing and editing.

Acknowledgements

I am thankful to a number of individuals who provided invaluable support to me. A few paragraphs are not enough to express my gratefulness towards them.

I owe a debt of gratitude to my advisors, Dr. Tom Moore and Prof. Chris Marrows, whose original ideas form the bedrock of this work. I'm grateful to Tom for providing invaluable guidance and evaluation at every stage of the research, for being always available for a discussion, and for encouraging me to pursue my ideas. I'd like to thank Chris for introducing me to new concepts in physics, for many discussions, and for the all the advice. I'm thankful to them both for letting me express my ideas without trepidation.

I am deeply grateful to Dr. Oscar Cespedes and Dr. Gavin Burnell for providing assessments and guidance during the research; to Prof. Bryan Hickey for always encouraging me to perform.

Special thanks to Dr. Mannan Ali for single-handedly keeping the labs running, and for his training and guidance with experiments.

I am very grateful to John Turton and Brian Gibbs for their help with the cryogenic and vacuum systems; to Glenys Bowles for her endless help and support with the administrative affairs.

My appreciation goes to the investigators and fellow researchers of my grant network for their advice and support. I will always cherish the wonderful times we spent in different cities across the world.

In the Condensed Matter group, I'll be forever grateful to two fantastic groups of friends. Firstly, those who welcomed me to the group, helped and trained me, took me to the pub every week, and threw grand parties and get-together. Alphabetically, Aleš, Fatma, Joe, May, Nathan, Philippa, Priya, Rowan, Sophie, and Tim. Secondly, I've been privileged to have the support and friendship of Adam, Amy, Ben, Craig, George, Jamie, Katharina, Katy, Kowsar, Matt, and Shoug. These people have held me high when I was down, and held me higher when I was up.

Amy, Katharina, Kowsar, and Shoug fed me on a regular basis (due to my lack of interest in cooking). I am eternally grateful for this.

When I arrived in Leeds with £140 in my pocket and with no place to stay, Shams and Sonia opened their door to me without hesitation. My heartfelt thanks to them both for this rare act of generosity.

Lastly, I thank the European Commission for the Research Fellowship.

Abstract

The interfacial Dzyaloshinskii-Moriya interaction (DMI) is investigated in thin film heterostructures with perpendicular magnetic anisotropy. The DMI is influenced by the atomic arrangement at the interface. Also, the DMI is insensitive to the antiferromagnetic spin order.

Ta/CoFeB/MgO heterostructures were annealed at different temperatures ranging from 210-280 °C to bring about changes in the atomic arrangement at the interfaces. DMI fields were then measured using a field-driven creep regime domain expansion technique. The DMI peaks at $D = 0.057 \pm 0.003$ mJ/m^2 at an annealing temperature of 230 °C. The DMI field and the anisotropy field follow a similar trend as a function of annealing temperature. These experiments allow the conclusion that the underlying mechanisms for the behaviour of the DMI and the anisotropy are related to interfacial crystal ordering and B expulsion out of the CoFeB layer and consequent accumulation at the interfaces as the annealing temperature is increased.

The DMI was also explored in systems containing an antiferromagnet (AFM) layer. Trilayers of Pt/Co/IrMn and Pt/Co/FeMn were fabricated which exhibit large perpendicular exchange bias of 40 mT and 140 mT, respectively, in the as-grown state. Different phases of the antiferromagnetic IrMn and FeMn layers were accessed by varying the thickness. The magnetic domain morphology of the ferromagnetic Co layer is influenced by the spin order of the AFM layers. These variations in domain texture are related to the ferromagnet-antiferromagnet (FM-AFM) inter-layer exchange coupling and the anisotropy energy of the AFM layer. In contrast, the DMI remains unchanged, within experimental uncertainty, for different phases of the AFM layers. The DMI was measured by Brillouin light scattering spectroscopy. From these experiments, it is inferred that the DMI is insensitive to both AFM spin order and exchange bias, in agreement with theory. The DMI is different in the two systems: $D = -1.14 \pm 0.05$ mJ/m^2 for Pt/Co/IrMn and $D = -1.50 \pm 0.08$ mJ/m^2 for Pt/Co/FeMn; this is when IrMn and FeMn layers are paramagnetic. The difference in DMI is due to different Mn concentration at the FM/AFM interface of the two systems, and also due to Fe segregation from the FeMn layer.

List of abbreviations

AFM	Antiferromagnet
Ar	Argon
BLS	Brilloiun Light Scattering
Co	Cobalt
CoFeB	Cobalt-Iron-Boron
DMI	Dzyaloshinskii-Moriya Interaction
DW	Domain Wall
EB	Exchange Bias
FeMn	Iron-Manganese
FM	Ferromagnet
IP	In-plane
IrMn	Iridium-Manganese
MgO	Magnesium-Oxide
MOKE	Magneto-optical Kerr Effect
OOP	Out-of-plane
PEB	Perpendicular Exchange Bias
PM	Paramagnet
PMA	Perpendicular Magnetic Anisotropy
Pt	Platinum
SHE	Spin-Hall Effect
Si	Silicon
SIA	Structural Inversion Asymmetry
SOT	Spin-Orbit Torque
SQUID	Superconducting Quantum Interference Device
Ta	Tantalum
VSM	Vibrating Sample Magnetometer
XRD	X-Ray Diffraction
XRR	X-Ray Reflectivity

CONTENTS

Chapter 1

Introduction

1.1 Chiral magnetism

Symmetry breaking mechanisms are of fundamental importance in physics. For instance, due to spontaneous symmetry breaking, elementary particles in the universe acquire mass through the Higgs boson [1, 2]. A break in symmetry can also often lead to chiral structures in nature, such as proteins, sugars, or the DNA double helix, which always twists in the same direction. Life is chiral.

Chirality, a term introduced by Lord Kelvin [3], means handedness. Chiral phenomena are those that lack mirror reflection symmetry. Chirality can result from spontaneous symmetry breaking, as in macroscopic quantum systems [4], or can be stabilised by a chiral interaction, as in magnetism [5]. This thesis is aimed at improving our understanding of chiral magnetic behaviour, particularly in the nanoscale.

In magnetic materials lacking symmetry, chiral textures arise through the arrangement of atomic spins. This arrangement is governed by a magnetic interaction, known as the Dzyaloshinskii-Moriya interaction (DMI) [5, 6]. It is an antisymmetric form of the otherwise symmetric exchange interaction, which gives rise to ferromagnetic behaviour in materials.

The DMI can also exist [7, 8] in fabricated material systems, where inversion symmetry is broken at an interface. This work is focused on such multilayered systems, particularly on those which exhibit magnetisation in a direction perpendicular to the surface plane. Such heterostructures are undergoing intensive fundamental research with a view to be used in devices [9, 10, 11] in which electron spins are utilised, and as such, the research field is known as spintronics [12]. In these multilayered systems, the DMI gives rise to chiral spin textures, which can be manipulated to design novel devices with improved functionalities.

The next few sections of this introductory chapter will give the reader a review of research in topics relevant to this thesis, including spintronics and the Dzyaloshinskii-Moriya interaction. The chapter will then end with a brief overview of the work presented in this thesis.

1.2 Spintronics

Spintronics [12, 13, 14] is a promising technology under development which hopes to complement the semiconductor-based electronics technology, with a focus to improve the functionalities of current electronic devices. Conventional electronic devices function by controlling the charge of the electron, whereas spintronic devices work by controlling its spin. Manipulation of spins is both faster and consumes less energy, and thus allowing for efficient and low power memory, sensing, and logic devices.

The first application of spintronics was in 1997 in computer disk drives. This was through the giant magnetoresistance (GMR) effect [15, 16] discovered in 1988, which led to the awarding of the 2007 Nobel Prize to A. Fert and P. Grünberg. The GMR effect was observed in thin film multilayer systems where ferromagnetic and non-magnetic layers are alternately stacked [17]. When the FM layers are aligned parallel, the electrical resistance is low, whereas when they are aligned anti-parallel, the resistance is high. This is due to spin dependent scattering at the interfaces. The difference in resistance between the two magnetic states is very large, and hence extremely sensitive, and is used to read out information from magnetically recorded media. The extreme sensitivity means that data can be read out from very densely packed magnetic data bits efficiently and reliably. This has led to higher density, faster, and cheaper drives than were previously possible.

Researchers have since been utilising spintronics technology for other types of memory, such as magneto-resistive random access memory (MRAM) [18]. Commercial MRAMs as main computer memory are already available in the market, while MRAMs to replace the embedded cache memory in processors are being developed [19]. The goal, however, is to fundamentally redesign processor architecture using spintronics logic [10, 20]. Further into the future are spintronics-based applications in quantum computing, neuromorphic computing, energy harvesting, etc [21].

1.3 The Dzyaloshinskii-Moriya interaction

The quantum mechanical exchange interaction, discovered in 1926 by W. Heisenberg [22] and P. Dirac [23], is at the origin of magnetic behaviour in materials. It consists of a strong symmetric and a weak antisymmetric contribution. The symmetric component, also known as the Heisenberg interaction, prefers collinear orientation of neighbouring spins. The antisymmetric component, the Dzyaloshinskii-Moriya interaction (DMI), after the original proposal by I. Dzyaloshinskii [5] in 1958 and later by T. Moriya [6] in 1960, prefers canted orientation of adjacent spins. In order to exist, the DMI needs spin-orbit interaction [6] and a crystal environment lacking central symmetry. In materials possessing such properties, chiral spin structures, such as homochiral (single-handed) spin spirals [24, 25] and skyrmion (particle-like spin configuration) lattices [26, 27] have been observed as magnetic ground states.

Another type of magnetic system where DMI can exist is in thin film heterostructures lacking structural inversion symmetry. It was proposed by A. Fert and P. M. Levy [7] in 1980 that the symmetry is broken at the interface between a magnetic and a non-magnetic layer, and in such a scenario, a non-magnetic atom, if its spin-orbit coupling is sufficiently large, can mediate a Dzyaloshinskii-Moriya-type exchange interaction between two atoms of the magnetic layer. Indeed it was shown that the DMI can be generated by growing a few atom-thick magnetic layer on top of a layer with a large spin-orbit coupling [28, 29, 30]. In these systems, the thinness of the layers, together with spin-orbit coupling may also give rise to a perpendicular magnetic anisotropy (PMA) [31]. In fact, initially, these kind of systems were grown and studied for their perpendicular magnetisation due to its useful technological applications [13, 32]. The PMA in these systems can be strong and restricts the formation of spin spirals, and as such, in thin film systems, the DMI was overlooked for more than two decades. However, recent works on current- [33, 34] and field-induced [35, 36, 37] domain wall (separation between two magnetisation regions) dynamics in thin film multilayers, allowed the observation of chiral behaviour, as the strength of chiral interaction and anisotropy becomes comparable at a magnetic edge, like a domain wall (DW), or at a physical edge, like in a microstructure.

In these ultrathin film heterostructures, the DMI is that of the interfacial form and has been found to be present at the heavy-metal/ferromagnet (HM/FM) interface [33, 34], at the FM/oxide interface [38, 39], and more recently, at the FM/AFM interface [40]. In these cases, the DMI stabilises spin configurations, such as chiral Néel type (cycloidal) DWs [41, 30, 42, 43] and skyrmions [44, 45]. Such spin structures can be manipulated as information carriers [32, 46, 47] by electric currents via spin torques generated in adjacent HM [48] and/or AFM [49] layers.

1.3.1 Notable works and techniques

This section will briefly outline some of the prominent studies in this field. In an attempt to keep a coherent structure, the works will be grouped according to the measurement techniques.

Over the past decade there have been several studies exploring the presence of the DMI and its effects on different multilayer systems using a host of techniques. The earliest works employed spin-polarised scanning tunnelling microscopy to identify chiral magnetic order at metallic surfaces, specifically in 2006, for a monolayer of Mn on W(110) [28], and in 2008 on W(001) [50]. However, the question remained open on whether these spin spirals are Bloch-type (helical) or Néel type (cycloidal). Later in 2009, the spin spirals could also be identified as Néel type; in an Fe double layer on W(110) [29]. Soon afterwards, other methods to measure the DMI started to emerge, such as field- and current-driven domain expansion technique, Brillouin light scattering (BLS) spectroscopy, and Lorentz transmission electron microscopy (Lorentz TEM). In this thesis, the field-driven method and BLS were used to quantify the DMI and investigate the chirality of the magnetic order in ultrathin film heterostrucutres.

The field-driven creep regime domain expansion technique was first demonstrated in 2013 by Je *et al.* [35] in Pt/Co/Pt. The DMI induces a chirality in the DWs and modifies the energy, which results in an asymmetric out-of-plane (OOP) field-driven expansion of a bubble domain under an in-plane (IP) field. The DMI was modelled as an effective field [41] and extracted from creep regime DW motion. Immediately afterwards, in 2014, using this method Hrabec *et al.* [36] presented how the chirality of Néel DWs can be interchanged from being right-handed (right rotating) to left-handed (left rotating) by tuning the net DMI in the system by modifying the DMI at the top interface of Pt/Co/Pt through the insertion of an Ir layer. This showed that the Ir/Co and Pt/Co interfaces have opposite DMI. They also demonstrated that the DMI almost vanishes for an epitaxial Pt/Co/Pt stack when compared to its polycrystalline counterpart, and thus clearly pointing out the role of interfaces on the DMI. In 2015, Yang *et al.* [51] performed first principles calculations to elucidate the mechanism of the DMI at the Co/Pt interface. They showed that indeed the DMI is localised at the interface, and that it is driven by spin-orbit coupling, consistent with the Fert-Levy model [7, 44]. They also demonstrated a decrease in the DMI strength with increased intermixing at the interface. Also in 2015, using domain expansion patterns Kim *et al.* [52] proposed a method to determine DW types by considering contributions from the DMI and Zeeman energy that causes preferential elongation of bubble domains, from which the DW type could be determined.

There have been reports on this bubble expansion creep technique, by Lavrijsen *et al.* [53] in Pt/Co/Pt and Vañatka *et al.* [54] in Pt/Co/GdO$_x$, depicting a deviation of experiments from the creep theory. In response to this, Jué *et al.* proposed the contribution of an intrinsic chiral damping in Pt/Co/Pt multilayers [55], which may cause this divergent DW motion from creep. A phenomenological explanation was later reported by Akosa *et al.* [56]. Also, the formation of creep bubble domains with non-elliptical tear drop shapes at high IP fields were shown by Lau *et al.* [57]. They explained this behaviour by considering global energy variations of the entire domain shape rather than the energy of the DW at a finite point in space, which is the usual approach. This was followed by another paper [58] from the same research group, where it was depicted that elastic deformation of DW can occur due to stiffness, which may explain the deviation from creep.

BLS is used to measure the non-reciprocal spin wave dispersion, which manifests due to the presence of the DMI. The energy contribution of the DMI to propagating spin waves was actually a theoretical work by Moon *et* *al.* [59] in 2013. This led to the first experimental demonstration of measuring the DMI by BLS in 2015 by Di *et al.* [60] on Pt/Co/Ni multilayers. Later in the same year, a number of experimental publications emerged. Cho *et al.* [61] used the technique on Pt/Co/AlO$_x$ (also Belmeguenai *et al.* [62]) and Pt/CoFeB/AlO$_x$ heterostructures. They performed thickness dependent studies and confirmed that the DMI indeed manifests as an interfacial effect. Nembach *et al.* [63] reported a linear relation between Heisenberg exchange and DMI in Py/Pt bilayers, thus demonstrating that the two interactions share the same underlying mechanism. Soucaille *et al.* [64] compared the techniques of BLS and DW creep measurements for CoFeB/MgO bilayers on various underlayers. They concluded that the DMI values from the two methods only agreed qualitatively and suggested to treat the underlying models with caution. More on this can be found in Section 6.3.3.

The DMI results in canted orientation of spins at the physical edges of a microstructure. One of the early works to demonstrate this was in 2014 by Pizzini *et al.* [37], where they utilised this chiral interaction to preferentially nucleate domains at one edge of a microstrucutre of perpendicularly magnetised Pt/Co/AlO$_x$ by biasing the system with an external in-plane field. This asymmetric nucleation is, of course, chiral and depends on the magnitude and direction of the applied in-plane field, and thus from this the authors were able to determine the strength of the DMI. Using the same principle, later in 2016, Han *et al.* [65] demonstrated a method of obtaining the DMI from shifted hysteresis loops of asymmetric microstructures. Here, it is pertinent to mention a theoretical proposal of measuring the DMI from shifted magnetic hysteresis loops, but where these are instead due to exchange bias in an AFM/FM bilayer, which was reported by Yanes *et al.* [66].

The technique of Lorentz TEM was used to indirectly identify the presence of the DMI in Pt/Co/AlO$_x$ films [43]. In this work, Benitez *et al.* directly observed Néel DWs in this system, which consequently indicated the presence of the DMI. They measured the magnitude of the DMI by domain annihilation. This method was originally proposed by Hiramatsu *et al.* [67] in 2014 in a theoretical study. The presence of homochiral Néel walls requires large fields to merge two expanding domains. This is because of the high energy barrier that exists when two Néel walls meet, as they have the same chirality. A DMI value thus can be extracted from the annihilation fields.

The above works indicate that intensive research on the DMI is on going along with the development of new measurement techniques. Open questions remain on the validity of these techniques and on the reliability of the magnitude of the DMI obtained in different multilayers using these techniques.

1.3.2 Effect on current-driven domain wall dynamics

Current-driven DW motion in magnetic materials holds promise for low power and high performance memory and logic devices [32, 10, 68]. Conventionally, such devices used a torque due to the transfer of spin angular momentum (spin transfer torque) between a fixed and a free ferromagnetic layer separated by a non-magnetic layer [69, 70]. This mechanism was facilitated by a spin-polarised current flowing between the two layers. The torque on a magnetic DW as predicted by Berger [71] is based on the same principle.

In the latest generation of these devices, which uses even less power, DWs are driven by torques (spin-orbit torques) originating from an adjacent non-magnetic layer [72, 73, 74]. These torques are generated by spin-orbit effects, such as Rashba [75], spin Hall [76], and Dresselhaus [77] effect. Particularly in multilayers with perpendicular anisotropy and inversion asymmetry, the combination of the spin Hall effect (SHE) and the DMI from a heavy-metal underlayer, has generated very high speed DW motion [33, 34]. This is because the current-induced dynamics of a DW under the spin Hall torque depends on the DW spin structure, which is set by the DMI.

The action of the DMI on DWs was first studied on Fe double layer on W(110) by Heide *et al.* [78] in 2008, following the experimental work by Bode *et al.* [28]. Through first principles calculations they reported that a sufficiently strong DMI can fix both the type (Néel) and chirality of a DW. However, it was Thiaville *et al.* [41] in 2012 who first studied, numerically and analytically, the current-driven dynamics of DWs in perpendicularly magnetised multilayers with DMI and SHE. By modelling the DMI as a chiral in-plane field localised on a DW, they demonstrated how the DMI converts Bloch walls to Néel walls of a fixed chirality. They termed these Dzyaloshinskii DWs. A year later in 2013, Emori *et al.* [33] and Ryu *et al.* [34] demonstrated experimentally that the presence of DMI-stabilised Néel walls means that the spin Hall torque can act efficiently, as a Néel wall lies transversely to the associated field from the torque. This results in high speed DW motion. The DMI field can be evaluated by applying an offset IP field of varying magnitude. Furthermore, since the DMI also selects the chirality of these Néel walls, they move unidirectionally in response to an applied current of a fixed polarity. These results have a crucial impact on the development of DW based spintronic devices.

1.4 Antiferromagnetic spintronics

In terms of both fundamental curiosity and practical application, ferromagnets have been a topic of interest to human beings for thousands of years. As such, all spintronic technologies, whether in commercial or in research phase, use ferromagnets. On the other hand, the use of antiferromagnets (AFMs) as an active element in microelectronic devices has remained elusive, although they are abundant and discovered in the 1930s by L. Néel [79]. This is mainly due to their lack of a net magnetisation, as moments alternate between individual atomic sites, which makes them insensitive to magnetic probes. Very recently, research on antiferromagnetic spintronics [80, 81, 82] has started to emerge, following breakthroughs in our abilities to manipulate charge-spin coupling effects, such as the spin Hall effects [83]. AFMs possess properties which can be very useful in device applications, such as very high frequency dynamics [84], zero stray fields, efficient generation of spin current and spin torques [85], etc. Indeed, there are strong suggestions that AFMs could contribute to future spintronic technologies [86].

Use of antiferromagnetic materials in spintronics has generally been done in three ways: through intrinsic manipulation (for instance, with a current) of individual moments, through interfacial coupling [87, 88] in a FM/AFM bilayer, and through the use of synthetic AFMs. For the case of intrinsic switching, Wadley *et al.* [89] in 2015 demonstrated the reversal of an AFM layer of CuMnAs using current-induced spin torques. The authors also showed that the magnetic state in such a device is indeed immune to external fields. Later in 2017, Olenik *et al.* [90] successfully fabricated a memory cell out of the same material and compatible with current microelectronic circuitry. They demonstrated that the memory element can record pulses with time-scales of hundreds of picoseconds. Optical switching of AFMs were also shown by Manz *et al.* [91] in 2016.

There were reports of current-induced field-free magnetisation switching of a FM layer in out-of-plane AFM/FM exchange coupled systems. In 2015 Fukami *et al.* [92] showed this in PtMn/[Co/Ni] multilayers by generating spin-orbit torques by passing a current through the in-plane magnetised AFM underlayer of PtMn. Normally, an external field is needed for the switching in order to break the symmetry. However, here the authors utilised the exchange bias for this. A similar work came out in 2016 [93], but for the system of OOP IrMn/CoFeB/MgO. Also in 2016, van den Brink *et al.* [94] utilised the same principle of exchange biasing in Pt/Co/Pt/IrMn multilyers (the top Pt layer was very thin) to achieve field-free current-induced switching. The difference here is that the current was through the heavy-metal Pt layer and not through the AFM layer. Another notable magnetisation switching study was performed in in-plane exchange coupled system of IrMn/Py by Tshitoyan *et al.* [49] in 2015. In this work, the authors report a large spin Hall angle of IrMn (0.22 ± 0.04) which exceeds most heavy-metals, such as, Pt (0.056 ± 0.005 [95]), Ta (0.12 ± 0.04 [48]), etc. They also correlate a large current-induced torque with the presence of the exchange bias by decoupling the bilayer with a spacer layer.

In racetracks made of a synthetic AFM, a record current-driven DW velocity of 750 m/s was achieved by Yang *et al.* [96]. In this case, two oppositely magnetised ferromagnetic systems of Pt/Co/Pt with PMA was separated by a non-magnetic Ru layer. The authors attributed the high velocity to a novel exchange coupling torque. Further to this, they also reported a high packing density of DWs due to the lack of magnetostatic fields.

Research on AFM spintronics is in its infancy and requires continued efforts to realise novel practical devices. There have been reports, as summarised above, on current-driven magnetisation switching and DW motion in systems comprising AFM layers. However, how these operations are affected by fundamental mechanisms, such as the DMI and exchange coupling, are still to be explored. This project thus aims to contribute to this research by investigating such elementary processes in multilayers containing AFMs.

1.5 Thesis overview

The interfacial DMI has become experimentally relevant over the last few years. As a result, there is considerable need to understand the elementary mechanisms of this interaction. As such, the focus of this thesis was to investigate some of the fundamental aspects of the interfacial DMI. The thesis is comprised of two projects, which are different in many aspects, but are tied together by the common phenomenon of chiral magnetism, brought about by the DMI. The work is covered in Chapters 4-6.

Chapter 4 investigates how the interfacial DMI in perpendicularly magnetised Ta/CoFeB/MgO thin film system is influenced by the atomic order at the interfaces. The DMI is measured by a field-driven creep regime domain expansion technique, which is elaborated in this chapter. Changes in atomic order are brought about by annealing the system close to its crystallisation temperature. The results are interpreted in the context of anisotropy field measurements.

Chapter 5 is concerned with the fabrication of perpendicularly magnetised exchange coupled systems of Pt/Co/IrMn and Pt/Co/FeMn. The spin order of the antiferromagnet layers is controlled by varying the thickness. Subsequent structural and magnetic characterisation is performed and the link between these properties is established. The two systems are also optimised to obtain a strong perpendicular anisotropy and a large exchange bias.

Chapter 6 builds on the work in Chapter 5 by exploring interfacial mechanisms in the exchange coupled systems. Particularly, it investigates the effect of the antiferromagnetic Néel order on both the domain morphology and the DMI. The domain texture is imaged magneto-optically, while the DMI is probed by Brillouin light scattering spectroscopy.

Preceding the results, Chapter 2 will discuss some of the necessary background theory, while Chapter 3 will outline the experimental techniques in detail.

Chapter 2

Fundamental concepts

2.1 Introduction

This chapter will present the essential elementary concepts required in understanding the work in this thesis. Particularly, the notions of magnetism, magnetic anisotropy, domain wall dynamics, and exchange bias will be discussed. These concepts are central to the results presented later in the thesis. The descriptions given in this chapter are not exhaustive. For a more detailed discussion the reader is directed to references [97, 98].

2.2 Exchange interaction

Ferromagnetic behaviour in materials is due to the spontaneous alignment of atomic moments with nearest neighbours so that the interaction energy between them is minimised. This results in an ordered magnetic state. This magnetic order collapses at a certain critical temperature, called the Curie temperature T_C, which is material specific. Above T_C a ferromagnetic material becomes paramagnetic, where the spins are randomly oriented due to thermal energy.

The origin of this spontaneous alignment is the exchange interaction [22, 23], which is quantum mechanical in nature and is directly related to the Pauli exclusion principle [99]. When the orbitals of the outer valence electrons of two adjacent atoms overlap, the electrostatic energy from Coulomb interaction is less when the spins are aligned parallel, compared to when they are aligned antiparallel. This is because when they are parallel, the Pauli principle enforces that they cannot share a common orbit, and thus stay further apart. Hence, the Coulomb energy is reduced by stabilising the parallel spin configuration. As a result, the spins of these electrons tend to line up. This difference in energy between the two spin configurations is the exchange energy.

For simplicity, consider two electrons a and b with space coordinates $\mathbf{r}_1$ and $\mathbf{r}_2$, and with wavefunctions $\psi_\mathrm{a}(\mathbf{r}_1)$ and $\psi_\mathrm{b}(\mathbf{r}_2)$, respectively. The total wavefunction of the two electrons is then given by

$$\Psi_{1,2} = \psi_{\mathrm{a}}(\mathbf{r}_1)\psi_{\mathrm{b}}(\mathbf{r}_2). \tag{2.1}$$

Since electrons are fermions and indistinguishable, the total wavefunction must be antisymmetric upon exchange, according to the Pauli exclusion principle, which forbids two fermions to occupy the same quantum state. Thus,

$$\Psi_{1,2} = -\Psi_{2,1}. \tag{2.2}$$

The total wavefunction of the electrons can be described as a product of functions of space and spin coordinates such that

$$\Psi(\mathbf{r}) = \varphi(\mathbf{r})\chi(\mathbf{s}). \tag{2.3}$$

Thus, Equation 2.2 can be preserved by having either antisymmetric space, or antisymmetric spin functions. For the case where the spatial function is symmetric, the spin function must be the antisymmetric singlet state χ_{S}. This results in the singlet total wavefunction

$$\Psi_{\mathrm{S}} = \frac{1}{\sqrt{2}}\left[\varphi_{\mathrm{a}}(\mathbf{r}_1)\varphi_{\mathrm{b}}(\mathbf{r}_2) + \varphi_{\mathrm{b}}(\mathbf{r}_1)\varphi_{\mathrm{a}}(\mathbf{r}_2)\right]\chi_{\mathrm{S}}(\mathbf{s}). \tag{2.4}$$

When the spatial function is antisymmetric, the spin function must be the symmetric triplet state χ_{T}, which results in the triplet total wavefunction

$$\Psi_{\mathrm{T}} = \frac{1}{\sqrt{2}}\left[\varphi_{\mathrm{a}}(\mathbf{r}_1)\varphi_{\mathrm{b}}(\mathbf{r}_2) - \varphi_{\mathrm{b}}(\mathbf{r}_1)\varphi_{\mathrm{a}}(\mathbf{r}_2)\right]\chi_{\mathrm{T}}(\mathbf{s}). \tag{2.5}$$

The difference in the energies of these two states is given by

$$E_{\mathrm{S}} - E_{\mathrm{T}} = \int \varphi_{\mathrm{a}}^*(\mathbf{r}_1)\varphi_{\mathrm{b}}^*(\mathbf{r}_2)\mathcal{H}\varphi_{\mathrm{b}}(\mathbf{r}_1)\varphi_{\mathrm{a}}(\mathbf{r}_2)\mathrm{d}\mathbf{r}_1\mathrm{d}\mathbf{r}_2, \tag{2.6}$$

where $\mathcal{H}$ is the Hamiltonian that concerns the interaction between the two electrons. This difference signifies the energy produced by the exchange of two electrons. A spin-dependent Hamiltonian, the Heisenberg Hamiltonian, can be constructed as

$$\mathcal{H}_{\text{ex}} = -2J\mathbf{S}_1 \cdot \mathbf{S}_2, \tag{2.7}$$

where $\mathbf{S}_{1,2}$ are nearest neighbour spins, and J represents the integral in Equation 2.6, and is know as the exchange integral. When $J > 0$, $E_{\text{T}} < E_{\text{S}}$ and a triplet state is favoured, giving rise to ferromagnetic spin configuration, where the spins are aligned parallel. If $J < 0$, $E_{\text{S}} < E_{\text{T}}$ and the singlet state is favoured and the spin order is antiferromagnetic, where the spins are aligned antiparallel. Thus, in antiferromagnetic materials there is no net magnetisation. The critical temperature for antiferromagnetic materials is called the Néel temperature T_{N}, after L. Néel [79]. That is, above T_{N}, the antiparallel order of the magnetic moments disappear.

2.2.1 Itinerant ferromagnetism

The $3d$ transition metals Fe, Co, and Ni exhibit spontaneous magnetisation. In metals, electrons are delocalised and are described by the free-electron formalism. For the case of transition metals, the $3d$ band intersects the Fermi energy, as illustrated in Figure 2.1. In this band picture, spontaneous magnetisation is due to the split of the spin up and spin down electron bands. E. C. Stoner showed [100] that this spontaneous magnetisation happens if the gain in the exchange energy is greater than the loss in kinetic energy due to the split in the bands. Mathematically, the Stoner criterion for spontaneous magnetisation is

$$JN(E_{\text{F}}) > 1. \tag{2.8}$$

If the product of the exchange integral J and the density of states at the Fermi energy $N(E_{\text{F}})$ is greater than 1, then the material would exhibit spontaneous magnetisation. Fe, Co, and Ni have a large density of states at the Fermi energy E_{F} and satisfy the Stoner criterion at room temperature, and are thus ferromagnetic.

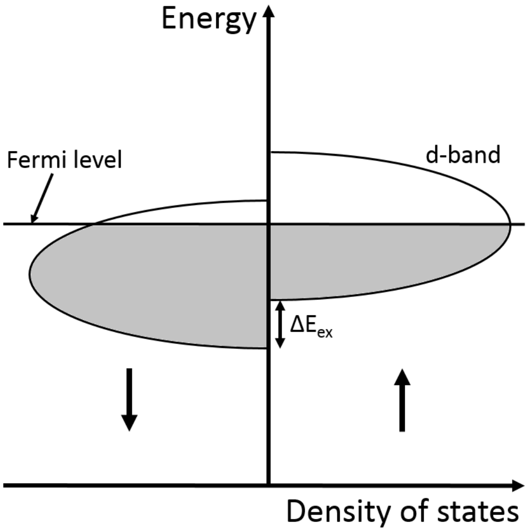

Figure 2.1: Schematics of the density of states at the Fermi level showing spontaneous magnetisation in transition metals. The two bands are mutually shifted by the exchange splitting energy.

2.2.2 Dzyaloshinskii-Moriya interaction

The Dzyaloshinskii-Moriya interaction (DMI) [5, 6] is a weak antisymmetric component of the exchange interaction. It exists in materials with a low symmetry and requires spin-orbit coupling. The interaction can be expressed by the Hamiltonian:

$$\mathcal{H}_{\mathrm{DMI}} = -\,\mathbf{D}\cdot(\mathbf{S}_1 \times \mathbf{S}_2), \tag{2.9}$$

where $\mathbf{S}_{1,2}$ are adjacent spins, and $\mathbf{D}$ is a vector which lies along a high-symmetry axis and couples the spins perpendicularly. This is in opposition to the symmetric Heisenberg interaction (Equation 2.7), which promotes a collinear orientation of neighbouring spins.

In thin film heterostructures, which are of concern in this thesis, an interfacial DMI can exist [7, 8] as the inversion symmetry is broken at the interface. Under such a condition, a heavy atom with a strong spin-orbit coupling, can facilitate a Dzyaloshinskii-Moriya-type exchange interaction between two atoms of the magnetic layer, as illustrated in Figure 2.2.

In magnetic systems where the Heisenberg interaction and the DMI are both

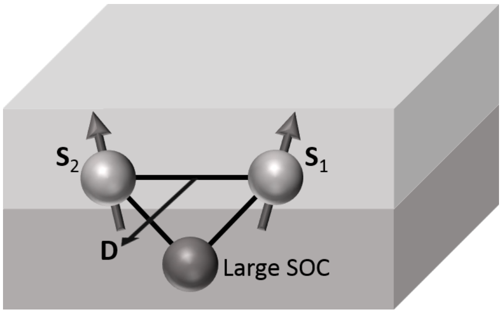

Figure 2.2: Mechanism of the Dzyaloshinskii-Moriya interaction at the interface of a magnetic (top) and non-magnetic (bottom) layer. A non-magnetic heavy atom with a large spin-orbit coupling couples adjacent spins ($\mathbf{S}_{1,2}$) of the magnetic layer such that $\mathbf{S}_1$ tilts relative to $\mathbf{S}_2$ by a rotation around the Dzyaloshinskii-Moriya vector **D**.

present, the total Hamiltonian contains both energy terms.

2.3 Magnetic anisotropy

When the magnetisation of a material points to a specific direction, the so called easy axis, then the material is said to have a magnetic anisotropy. Energy is needed to rotate the magnetisation away from the easy axis. This is known as the anisotropy energy. There are several origins of magnetic anisotropy [97], which will be discussed below.

2.3.1 Magnetocrystalline anisotropy

Energy is minimised when the magnetisation lies along a certain crystallographic direction, owing to the shape of the atomic orbitals and coupling between spin and orbital angular momenta. This means that it is easy to magnetise the crystal along this easy axis. Crystal anisotropies are of two types depending on the shape of the lattice structure:

1. Uniaxial anisotropy, where the energy depends on the orientation of the magnetisation with respect to the easy axis. It occurs in hexagonal

crystals such as cobalt. The energy is given by

$$E = KV \sin^2 \theta + \text{higher order terms}, \tag{2.10}$$

where K is called the anisotropy constant, V is the volume of the sample and θ is the angle between the magnetisation and the easy axis. The higher order terms are usually small and thus are not considered. Since the anisotropy is uniaxial, these type of systems have one easy axis and thus two energy minima, separated by energy maxima. This results in magnetic hysteresis.

2. Cubic anisotropy occurs in crystals having a cubic lattice system, such as iron and nickel. The anisotropy takes on a cubic symmetry with more than one easy axis. In this case the energy is given by

   $$E = KV(\alpha_1^2\alpha_2^2 + \alpha_2^2\alpha_3^2 + \alpha_1^2\alpha_3^2), \tag{2.11}$$

   where α is the cosine of the angle between the crystal axis and the magnetisation.

2.3.2 Shape anisotropy

For the case of a uniformly magnetised sample, magnetic free poles are generated at the surface. Magnetostatic interaction from this results in a field inside the sample having an orientation which is opposite to the applied magnetic field. Thus, this field is termed as the demagnetising field H_d, whose magnitude depends on the shape and magnetisation of the sample:

$$H_\mathrm{d} = N_\mathrm{d} M, \tag{2.12}$$

where N_d is the demagnetising factor, which depends on the shape of the sample, and M is the magnetisation. The shape anisotropy is given by

$$K_\mathrm{d} = \frac{1}{2} N_\mathrm{d} \mu_0 M^2. \tag{2.13}$$

The formation of domains in a sample is due to the competition between the exchange and the various anisotropy energies. A uniformly magnetised sample breaks into domains with magnetisation in different directions in order to reduce the demagnetising field and magnetostatic anisotropy energy.

2.3.3 Perpendicular anisotropy in thin film systems

In thin films, the total anisotropy energy is given by

$$E = K_{\text{eff}} V \sin^2 \theta, \tag{2.14}$$

where

$$K_{\text{eff}} = K_{\text{V}} + \frac{2K_{\text{S}}}{t}. \tag{2.15}$$

Here, the total anisotropy K_{eff} is split into volume anisotropy K_{V} and surface anisotropy K_{S} terms, with t as the thickness of the film. The volume anisotropy K_{V} contains contributions from magnetocrystalline anisotropy and shape anisotropy. The surface anisotropy K_{S}, can have an orientation perpendicular to the plane of the film, depending on the structure of the atomic orbitals at the interface and spin-orbit coupling. For example, in Pt/Co [31] and Ta/CoFeB [101] interfaces, hybridisation of atomic orbitals along with spin-orbit coupling gives rise to a perpendicular component of the anisotropy at the interface. The competition between the surface and volume anisotropy determines the strength and direction of the effective anisotropy K_{eff} of the system. A strong perpendicular interface anisotropy combined with a considerably small thickness of the films can result in the system having an overall perpendicular magnetic anisotropy (PMA).

Materials with PMA have significant relevance in terms of technological applications. Perpendicular anisotropy tends to be strong, and thus offers good magnetic stability in devices, for instance in data storage, due to the large energy between magnetisation states. In devices utilising magnetic domains and domain walls, a large anisotropy is very useful as it results in narrow domain walls, and thus allows for higher storage density, such as in hard disk drives.

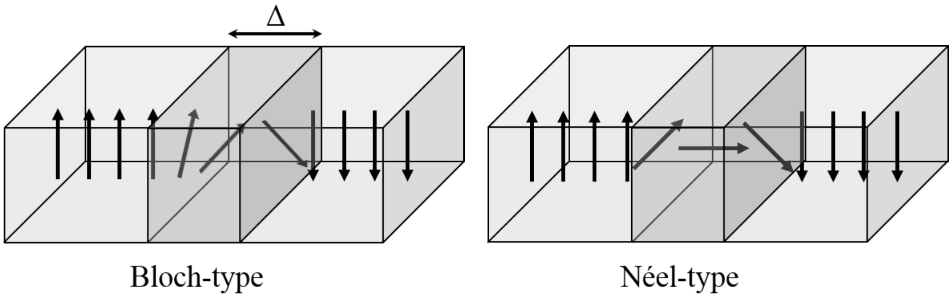

Figure 2.3: Structure of 180° domain walls which are present in systems with perpendicular magnetic anisotropy. Δ is the width of the domain wall. In a Bloch wall the spins rotate perpendicularly to the plane of domain magnetisation, while in a Néel wall the spins rotate along the plane.

2.4 Magnetic domain wall

A magnetic domain is a region with uniform magnetisation with all the moments pointing in the same direction. A uniformly magnetised magnetic system usually breaks into domains in order to minimise energy. The interface between two magnetic domains where the magnetisation gradually changes from one orientation to a different one is called a domain wall (DW), as illustrated in Figure 2.3 for a system with perpendicular anisotropy. The length across which the rotation takes place is the domain wall width Δ. This depends on the anisotropy and the strength of coupling between the spins. In magnetic systems with perpendicular anisotropy, the spins turn 180° between up and down magnetisation directions.

In systems with PMA, there are two types of domain walls. Bloch-type, after F. Bloch [102] who was first to analytically describe domain walls, are those where magnetisation rotation takes place in the direction perpendicular to the domain magnetisation plane. The spin spiral formed is thus helical. On the other hand, Néel-type DWs, after L. Néel, are those where the magnetisation rotates along the plane of domain magnetisation, and thus represents a cycloidal spin spiral.

Néel walls have a demagnetisation energy associated with them. Thus, Bloch walls are magnetostatically favoured. However, as mentioned previously, the Dzyaloshinskii-Moriya interaction can stabilise Néel walls and

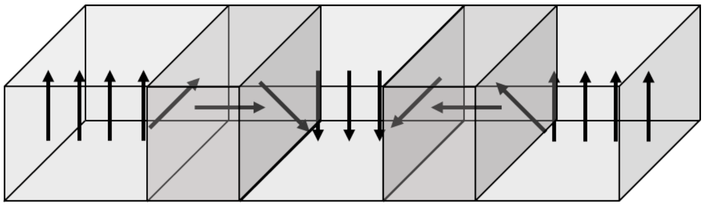

Right-handed (clockwise) Néel

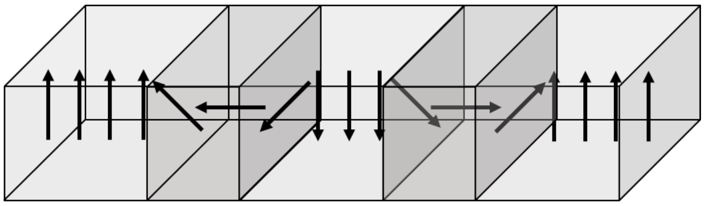

Left-handed (anticlockwise) Néel

Figure 2.4: Illustration of up-down and down-up Néel-type domain walls with a fixed chirality, present in the same system. The magnetisation rotates either clockwise or anti-clockwise.

also fix their sense of rotation, or chirality. More on this can be found in Chapter 4. Figure 2.4 shows examples of homochiral Néel walls in a system, where the sense of rotation of the magnetisation is always the same, and is determined by the DMI.

2.4.1 Dynamic regimes of an elastic system

The dynamics of an elastic physical system, driven by a force through a medium with weak disorder, is universal and can be divided into several regimes, as shown in Figure 2.5a. Creep [103, 104] and thermally assisted flux flow (TAFF) [105] motion occurs at low driving forces and requires thermal energy. At higher applied forces in the depinning regime [105], thermal excitation becomes less influential. Lastly, in the flow regime, the motion exhibits a linear dependence on the driving force [104, 105].

In the presence of weak random disorder, and at zero temperature, an elastic interface is pinned at disorder sites (local regions with a high energy barrier) and shows no motion in response to all driving forces below a critical force known as the depinning force f_{dep}, above which point a depinning trans-

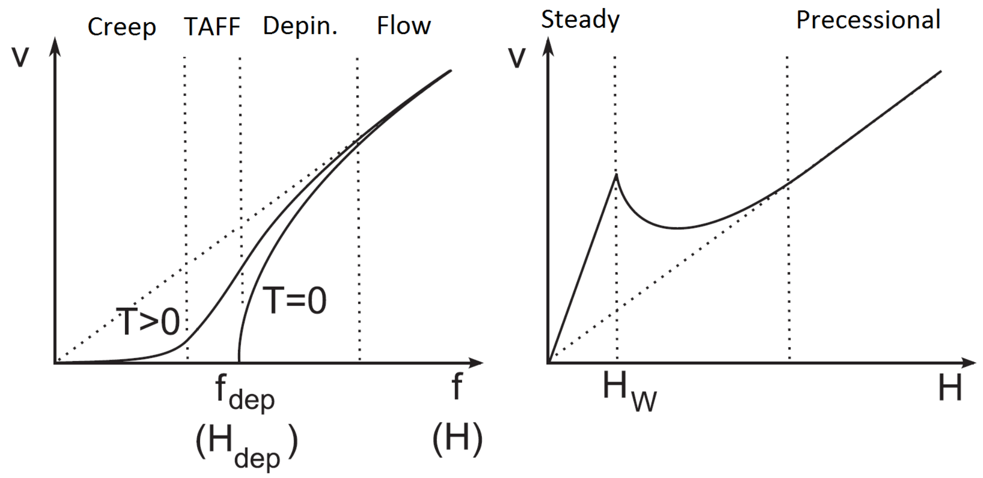

(a) (b)

Figure 2.5: (a) Theoretical regimes of the dynamics of an elastic physical system moving through weak disorder. (b) Walker breakdown of the domain wall velocity. The Walker field H_W marks the end of the steady-state motion of the domain wall. Figure adapted from ref. [104].

ition occurs. This situation changes when the temperature is non-zero and the depinning transition becomes smeared due to thermal excitation [103]. In such conditions, the interface is able to overcome the pinning energy barrier due to thermal energy. Consequently, a non-zero velocity is obtained for all finite forces. This thermally activated motion regime below f_{dep} is known as creep. Considering the DW as a 1D elastic interface driven by a field in a weakly disordered 2D surface, the creep regime velocity is mathematically described by [103, 104]

$$v_{\text{creep}} = v^0_{\text{creep}} \exp\left[-\left(\frac{T_{\text{dep}}}{T}\right)\left(\frac{H_{\text{dep}}}{H}\right)^{\mu}\right], \tag{2.16}$$

where v^0_{creep} is a numerical prefactor representing the characteristic velocity with which the DW jumps over the barrier, T_{dep} is the depinning temperature given by $T_{\text{dep}} = U/k_{\text{B}}$, where U is the pinning energy and k_{B} is the Boltzmann constant; H_{dep} is the depinning field, T is the temperature, H is the applied field, and the exponent μ has an experimentally obtained value of 1/4 [103, 104, 106]. Thus, in this region $\ln v$ varies linearly with $H^{-1/4}$.

Past the creep regime, the system enters the TAFF regime where $\ln v$ has a linear response with H. Like the creep regime, the TAFF regime is also thermally assisted, but the motion is more fluid due to an increased driving force. The DW velocity in this region is expressed as [103]

$$v_{\mathrm{TAFF}} = v^0_{\mathrm{TAFF}} \exp\left[-\left(\frac{T_{\mathrm{dep}}}{T}\right)\left(1 - \frac{H}{H_{\mathrm{dep}}}\right)\right]. \tag{2.17}$$

Beyond the TAFF regime, the DW velocity follows a power-law relationship with the applied field, $v = (H - H_{\mathrm{dep}})^{\beta}$ [107], where β is a critical exponent known as the depinning exponent. Finally, well beyond the depinning field, disorder becomes irrelevant and the system reaches the flow regime where the DW exhibits a viscous flow motion with the velocity and varies linearly with the applied field, $v = mH$ [104, 107], where m is DW mobility.

In magnetic systems, two separate regimes of linear flow with different mobility are observed, which are separated by a critical field called the Walker field H_{W} [108]. The difference in mobility is due to a change in wall dynamics. Below H_{W}, the DW magnetisation is stable and its motion is in the so-called steady state, where the velocity is proportional to the applied field. Above H_{W}, the DW becomes unstable as the magnetisation starts to precess, and the velocity drops. The mobility of the DW is higher in the steady-state regime than the precessional regime, as depicted in Figure 2.5b.

2.5 Exchange bias

When an AFM/FM bilayer (with $T_{\mathrm{C}} > T_{\mathrm{N}}$) is field-cooled through the T_{N} of the AFM layer from a temperature $T_{\mathrm{C}} > T > T_{\mathrm{N}}$, an additional anisotropy is introduced in the system. This results in a shift in the hysteresis loop of the FM, along with an increase in coercivity, as though an intrinsic field is present in the system. The FM is said to be biased by the AFM. This phenomenon of exchange bias EB, also known as exchange anisotropy, was discovered by W. Meiklejohn and C. Bean [87].

Qualitatively, this effect can be explained as a result of the exchange coupling at the AFM/FM interface, which aligns the AFM spins with the FM

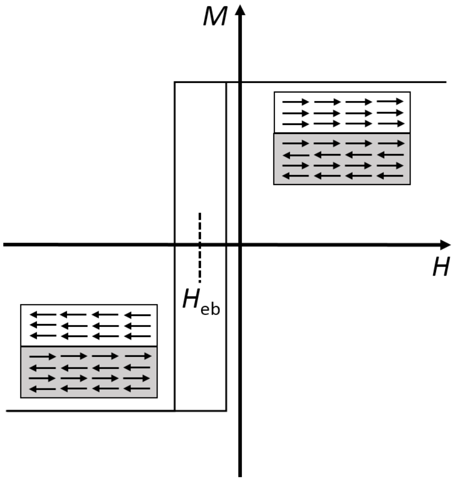

Figure 2.6: Simple schematic of the spin configuration of an exchange biased ferromagnet/antiferromagnet bilayer which results in a shifted magnetic hysteresis loop. The shift is the exchange bias field H_{eb}.

spins. This is illustrated in Figure 2.6. When the system is cooled through T_N under an applied magnetic field, the AFM spins adjacent to the FM spins align ferromagnetically due to exchange coupling. The other spin-planes in the AFM layer align antiferromagnetically and produce no net magnetisation. (If the AFM layer is deposited on top of the FM layer, then the AFM spins at the interface will follow the spin order of the FM layer, and a field cooling procedure may not be required if the anisotropy of the FM layer is sufficiently strong.)

Now, when a reverse field is applied to switch the FM layer, its spins feel a torque from the coupled AFM spins. Thus, this requires the application of an extra field (additional energy) than normal, in order to reverse the FM spins. However, if the applied field is reversed back to its initial direction, the FM spins will switch at a smaller field, since now the torque from the AFM spins is in favour of the field direction. Thus, this is an unidirectional anisotropy and the overall result is a shift in the FM hysteresis loop in one direction. The energy contribution to the system in presence of the applied field is given by:

$$E = \mu_0 M(H + H_{eb}), \tag{2.18}$$

where M is the magnetisation, H is external field, and H_{eb} is the exchange bias field.

The mechanism of exchange bias given above is very simplistic and considers an atomically smooth interface. In reality, it is the uncompensated spins at defect sites, such as step edges, dislocations, etc, that contribute to the exchange bias. Furthermore, many other factors, such as anisotropy, thickness, roughness, spin configuration and magnetic domains, of both the FM and the AFM layers, are involved in exchange bias. This makes the phenomenon quite complex, and in fact, a clear understanding of exchange bias at the microscopic level is still lacking.

Chapter 3

Methodology

3.1 Introduction

This chapter is a review of the various experimental techniques used in this project. Sample fabrication method will be discussed, along with the techniques used to characterise the structural and magnetic properties of the samples. Magnetic imaging technique will also be outlined.

3.2 Sputter deposition of thin films

Thin film structures are commonly deposited using a technique known as sputtering. In this process, atoms are ejected out of a target material by bombarding it with Argon ions due to momentum transfer. The ejected atoms settle on a surface (substrate) within the vicinity of the target. The deposition of thin films using sputtering is done within a high vacuum chamber inside which targets of desired materials are mounted on a number of sputtering sources.

The high vacuum inside the sputtering chamber used in this project is achieved by using two types of pumps. Firstly, a mechanical roughing pump is used in order to bring down the chamber dynamics from viscous fluid flow to molecular flow which is in the mTorr pressure regime. Then, a cryopump is used, which utilises a stage at a low temperature and with a large surface area, in order to adsorb the gas molecules inside the chamber. At this point, majority of the gas molecules inside the chamber are pumped out. What remains is hydrogen and water vapour. A liquid nitrogen-cooled Meissner trap is used prior to deposition in order to reduce the partial pressure of water. Thus, a base pressure of up to 10^{-8} Torr may be achieved.

Ar is then introduced into the chamber to provide the ions to collide with the target. This is done by applying a large negative voltage (around 500V) to the target. The application of the voltage causes the formation of a plasma and the resulting Ar+ ions are accelerated by the Coulomb force and collide with the target. Ar is used as it is inert and does not form compounds and thus allows for clean growth. Also, the mass of Ar atoms is ideal to transfer sufficient momentum and at the same time eject only surface atoms of the

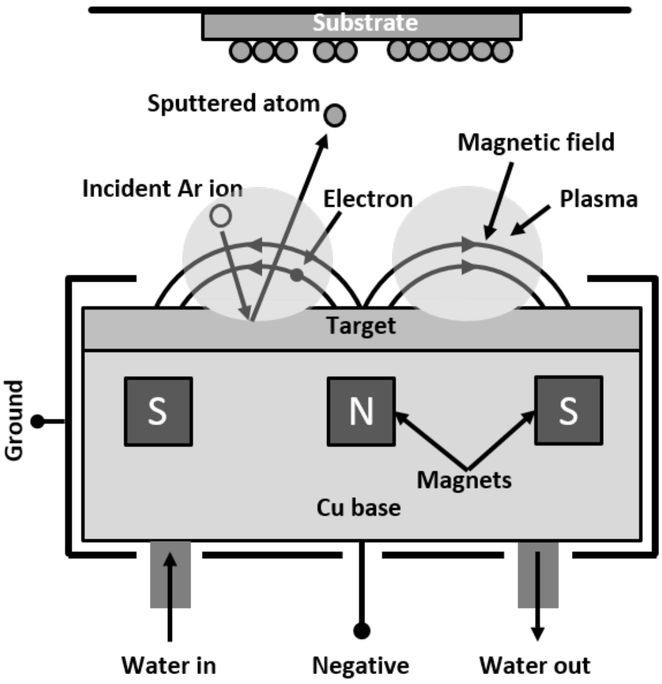

Figure 3.1: Schematic diagram showing the various elements of a magnetron sputtering machine. Ar ions sputter atoms from the target which nucleate into islands on a nearby substrate and then grow into a film.

target.

To increase the rate of emission, the technique of magnetron sputtering is utilised. Figure 3.1 shows the cross-section of a magnetron sputtering gun. The target is placed on a water-cooled Cu base for good thermal contact. Permanent magnets are used in such a way so as to generate a magnetic field directed in a radial arc from the centre and thus forming a torus through the target. The charged particles are confined in this toroidal magnetic field. Hence, the plasma is in close proximity to the surface of the target. For magnetic targets, a stronger field is used in order to compensate for the intrinsic magnetic flux of the target. Sputtering is a fast and reliable method of producing high quality thin films. Material growth rates and quality can be tuned by adjusting different parameters, such as the chamber base pressure, Ar pressure, gun power, target to substrate distance, etc [109].

3.3 Characterisation techniques

3.3.1 Vibrating sample magnetometer (VSM)

A vibrating sample magnetometer (VSM) [110] is used to measure the magnetic moment of a sample as a function of applied magnetic field. Thus, magnetic hysteresis loops can be obtained from which properties such as saturation magnetisation and coercivity can be extracted. The VSM system used in this project is an Oxford Instruments MagLab VSM capable of measurements between 1.5-300 K, and in magnetic fields up to 8 T. A schematic of the system is shown in Figure 3.2. A sample is mounted on a polyether etherketone (PEEK) holder, which is non-magnetic, resistant to both high and low temperatures, and has high thermal conductivity. The holder is then lowered, using a carbon-fibre rod, into the variable temperature insert (VTI) of a gas flow cryostat. A vertical magnetic field is generated by superconducting magnets placed at the base of the cryostat. The temperature is controlled by drawing helium gas into the VTI through a needle valve, and a resistive heater at the base of the VTI. The VTI is kept at low vacuum by a rotary pump. This removes air particles, such as, water vapour, nitrogen, oxygen, etc, which would otherwise freeze in low temperatures and could block the various components.

The top of the sample rod is attached to an actuator which vibrates the sample at a known frequency (55 Hz). The sample sits between two pick-up coils that have a voltage induced in them as the sample vibrates, due to Faraday's law of electromagnetic induction. When the magnetic sample is vibrated, it results in a change in the magnetic flux through the coils and induces an electromotive force which is detected as a voltage. The magnitude of the voltage generated in the pick-up coils is proportional to the magnetic moment of the sample. This voltage is detected by a lock-in technique where a reference signal with the same frequency as the sample vibration frequency is used in order to detect the in-phase signal from the coils. Thus, noise signals at other frequencies are ignored, ensuring high sensitivity. A calibration sample is used to convert the measured voltage into a value for the magnetic moment.

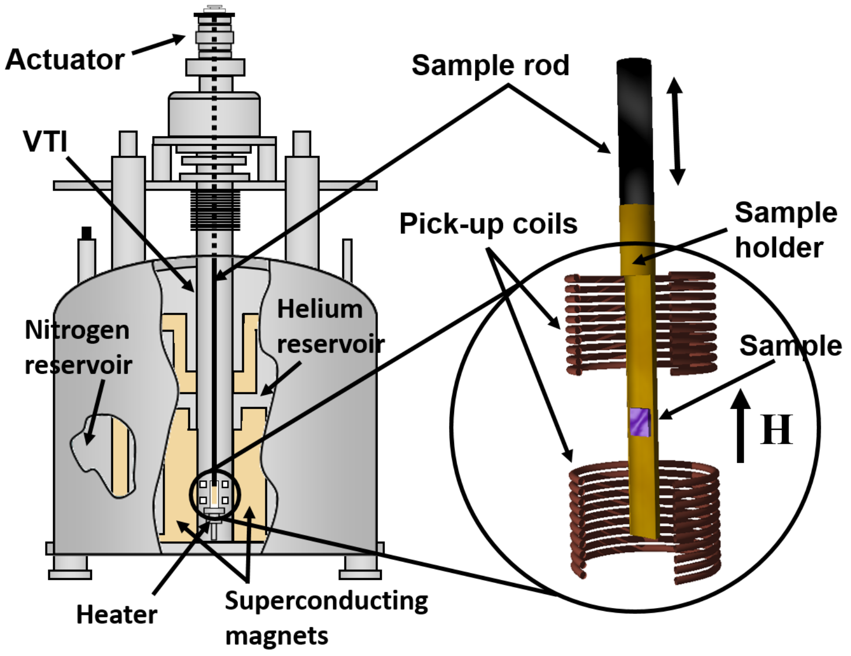

Figure 3.2: Schematic showing the various elements of a vibrating sample magnetometer. Figure adapted from ref. [111].

3.3.2 SQUID-VSM

In order to detect magnetic signal from samples with very small magnetic moment, for instance, multilayered systems with PMA where the FM layer is very thin, a superconducting quantum interference device (SQUID) [112] is utilised for magnetic sensing which provide sensitivity of about three orders of magnitude higher compared to a standard VSM. A SQUID-VSM has the same basic setup as a traditional VSM, except, for signal detection it uses a SQUID, which is inductively coupled to the VSM detection circuit (Figure 3.3). A SQUID consists of two Josephson junctions in a loop of superconducting material. Without the presence of any external magnetic field, an input bias current splits into the two branches. However, a magnetic field, for instance from a sample, induces a screening current in the superconducting loop generating a magnetic field that cancels the external flux. Since the screening current is flowing within a loop, it increases the current in one junction and decreases it in the other producing a detectable voltage across the junction. However, the flux enclosed within a superconducting loop is

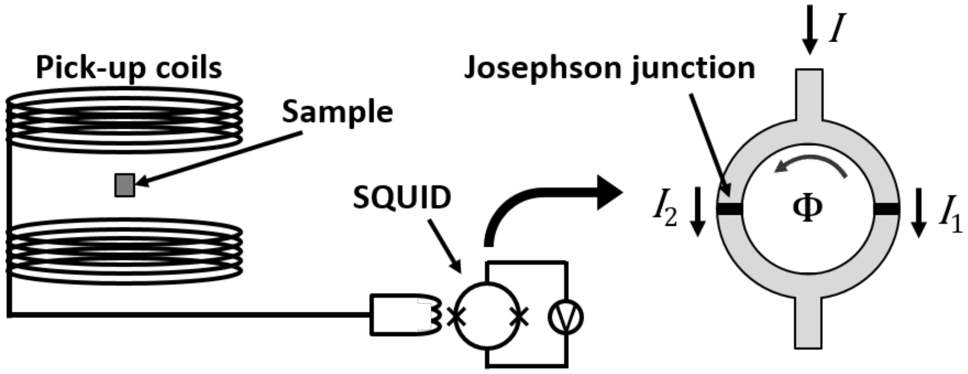

Figure 3.3: Illustration of the detection principle of a SQUID-VSM. The sample is vibrated in the detection coils which are inductively coupled to the SQUID. On the right is a diagram of a SQUID. The bias current I enters and splits into I_1 and I_2. The bent arrow represents the screening current. Φ represents the magnetic flux within the loop.

quantised and hence must be an integer number of flux quanta. Thus, every time the flux increases by a half of an integer, the screening current changes direction. The period of the current reversal is used to measure the magnetic signal of the vibrating sample. A Quantum Design SQUID-VSM system is used in this thesis capable of measuring samples from 1.6-1000 K, and with magnetic fields up to 6T.

3.3.3 X-ray characterisation

X-ray diffractometry is a technique used to characterise the physical structure of materials. The technique was discovered at the University of Leeds in 1912 [113] by W. H. Bragg, who, along with his son W. L. Bragg, was awarded the Nobel Prize in 1915 for their seminal work on X-ray crystallography. It is a non-destructive technique which is well suited to probe the microstructural properties of films and multilayers. In this project, X-ray reflectivity (XRR) is used to measure the thickness of sputtered films to calibrate deposition rates, and also to estimate the thickness of individual layers in multilayered systems. X-ray diffraction (XRD) is used to extract crystallographic information of the grown films.

X-rays follow the Bragg condition, illustrated in Figure 3.4, where reflections

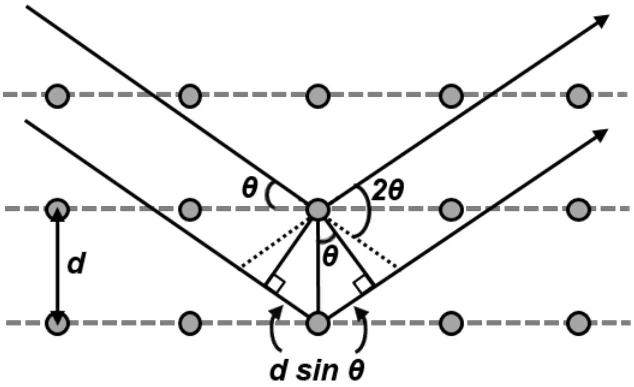

Figure 3.4: Bragg diffraction. Two parallel X-ray beams with the same wavelength and phase are incident at an angle θ on a crystalline solid and are scattered off two atoms from two different planes with a separation of d. The lower beam traverses an extra length of $2d\sin\theta$. Constructive interference occurs if and only if this length is equal to an integer multiple of the wavelength of the radiation.

from two parallel surfaces interfere constructively when the path difference between the two beams is an integer number of wavelengths, and destructively when the path difference is half of an integer. Thus, the Bragg's law for a structure of period d is given by

$$n\lambda = 2d\sin\theta, \tag{3.1}$$

where θ is the angle of reflection, λ is the wavelength of the X-ray, and n is the order of the reflection.

In an X-ray diffractometer, X-rays generated from an X-ray tube are directed at an angle θ on the surface of a sample and a detector collects the reflected beam at an angle 2θ. A diagram is shown in Figure 3.5. The sample and detector arm are rotated at constant angular velocities, where the detector is rotated at twice the velocity of the sample in order to maintain a θ-2θ mode of operation, which is commonly used.

In an X-ray tube, electrons are accelerated towards a copper target using a high voltage. When the accelerating voltage is sufficiently high, the accelerated electrons have sufficient energy to eject Cu electrons from the K shell creating a vacancy. When electrons from the L and M shell fill this vacancy,

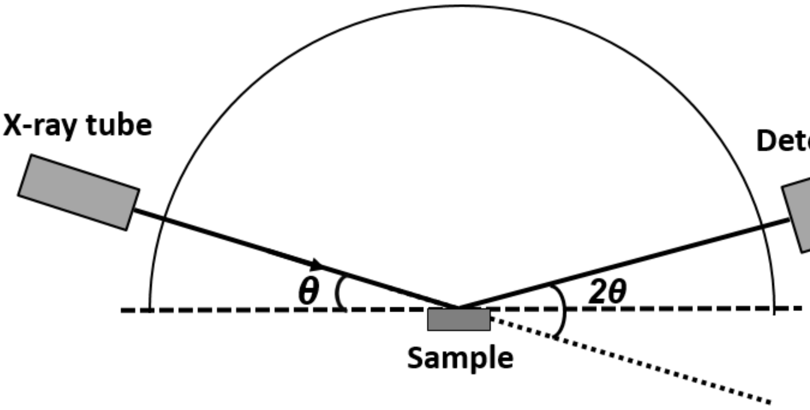

Figure 3.5: Illustration of X-ray diffractometry. The X-ray incidence angle is rotated during scanning and a detector tracks the reflected beam at twice that angle. The measured intensity is then plotted as a function of 2θ.

X-ray photons are produced. These are the characteristic Cu K radiation. Cu K_{α_1} radiation is produced when electrons relax from the L_3 to the K shell, while Cu K_{α_2} is from the L_2 to the K shell. Cu K_β is due to M shell electrons. A monochromator is used to remove all radiation except K_{α_1}, which has a wavelength of 1.54 Å.

X-ray reflectivity

X-ray reflectivity (XRR) scans are performed at low angles of reflection; at $2\theta < 15°$. At such low angles, interference occurs from surfaces and interfaces. For incident angles below a critical angle θ_c, total external reflection occurs, while above θ_c internal reflections from different interfaces result in interference fringes, which are known as Kiessig fringes after H. Kiessig, who observed this phenomenon in 1931 [114]. An example of this is shown in Figure 3.6. The period of the interference fringes is inversely proportional to the thickness of the layer, the depth of the fringes shows how parallel the reflecting surfaces are, while the rate of fall of the intensity is proportional to the roughness. Different electron densities in the different layers affect the reflection. This is analogous to different refractive indices in classical optics. Thus, the position of the point of internal reflection allows the estimation of the electron densities.

In this project, XRR scans are performed mainly to extract the thickness of

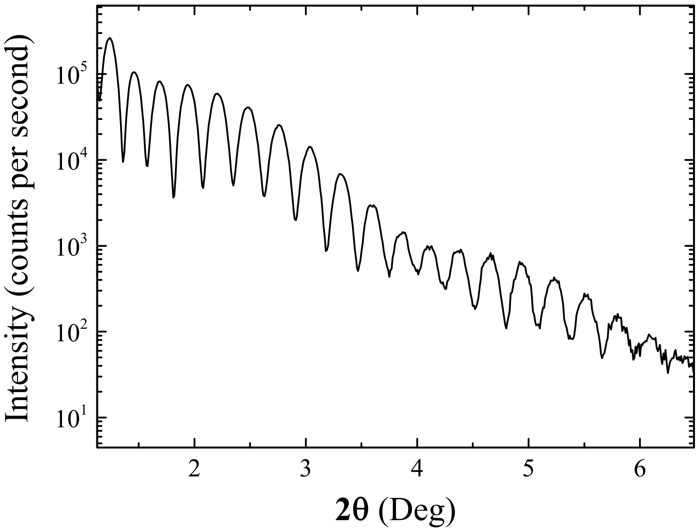

Figure 3.6: Kiessig fringes on an XRR scan of a 30 nm film of FeMn grown on a SiO_2 substrate. A modulation of the fringes can be observed which is due to the formation of a very thin oxide layer on top.

a single grown layer in order to calculate deposition rates by normalising the thickness by the deposition time. At an intensity maximum of a Kiessig fringe, the path difference between the reflected waves should be an integral multiple of the incident wavelength

$$n\lambda = 2t\sqrt{\sin^2\theta_n - \sin^2\theta_c}, \tag{3.2}$$

where θ_n is the angle when the maximum occurs, and t is the film thickness replacing d in Equation 3.1. At a small angle of incidence this can be simplified to

$$\theta_n^2 = \theta_c^2 + \left(\frac{n\lambda}{2t}\right)^2. \tag{3.3}$$

From the slope of a plot of the squares of the Kiessig fringe order against the squares of the angles of the intensity maxima, the thickness of the film can be obtained from

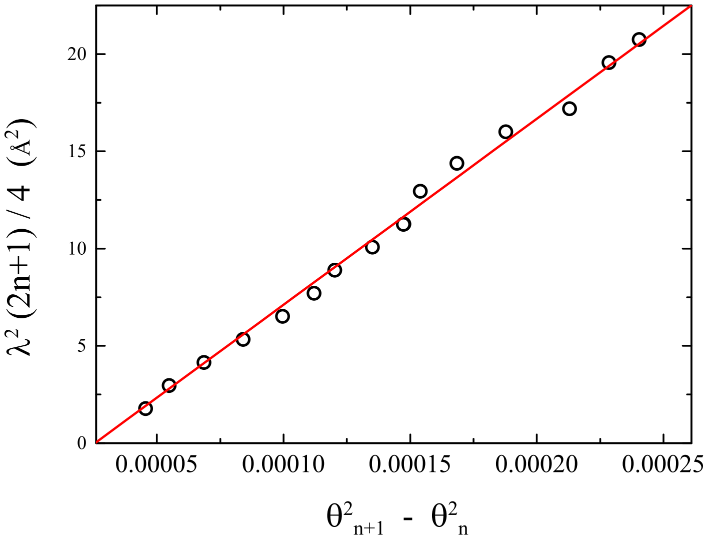

Figure 3.7: Plot of the square of Kiessig fringe order vs the squares of the angles of the intensity maxima; from the XRR scan of Figure 3.6. The square root of the slope of the linear fit (red) reveals the thickness of the layer.

$$t^2 = \frac{\lambda^2(2n+1)}{4(\theta^2_{n+1} - \theta^2_n)}. \tag{3.4}$$

This is shown in Figure 3.7 for the XRR scan of Figure 3.6.

Additionally, XRR scans are performed to assess layer thickness in multilayered structures where reflections at each interface results in a complex superposition of fringes. By modelling the fringes from the experimental data the thickness of the individual layers are determined. More on how XRR scans from multilayers are analysed can be found in Section 5.2.

X-ray diffraction

X-ray diffraction (XRD) scans are performed at high angles; at $2\theta > 20°$. Such scans provide information about the crystal structure of the sample. At high angles, the wavelength is comparable to the distance between atomic planes. This results in X-ray intensity peaks as a function of angle, as shown in Figure 5.1. From the position of the peaks it is possible to calculate the distance between atomic planes. With the lattice spacing known, this can then be used to extract the crystallographic directions of the measured material.

3.4 Magneto-optical techniques

Magneto-optical effects can be utilised to characterise materials in terms of their magnetic properties. In this work, the magneto-optical Kerr effect (MOKE) has been used to obtain magnetic information from samples. A laser MOKE magnetometer was used to obtain magnetic hysteresis loops, while a wide-field Kerr microscope was utilised for imaging magnetic domains.

3.4.1 Magneto-optical Kerr effect (MOKE)

When linearly polarised light is reflected from the surface of a magnetic material, it exhibits a rotation (Kerr rotation) of the polarisation. This is depicted in Figure 3.8. The phenomenon is known as the Kerr effect, after J. Kerr in 1877 [115]. Magneto-optical effects were first observed by M. Faraday (Faraday effect) in 1845, but in transmission, rather than reflection. Since the rotation is proportional to the magnetisation, the relative change in magnetisation of a material can be obtained by measuring the Kerr rotation. The Kerr effect is caused by the different absorption coefficients of left and right circularly polarised light, which are the two components of linearly polarised light. For an anisotropic medium, where the symmetry is broken by a spontaneous magnetisation, the dielectric displacement vector can be expressed as

$$\mathbf{D} = \tilde{\epsilon}\mathbf{E} = \epsilon\mathbf{E} + i\epsilon Q\mathbf{m} \times \mathbf{E} \text{ with} \tag{3.5}$$

$$\tilde{\epsilon} = \begin{bmatrix} \epsilon & \epsilon_{12} & \epsilon_{13} \\ -\epsilon_{12} & \epsilon & \epsilon_{23} \\ -\epsilon_{13} & -\epsilon_{23} & \epsilon \end{bmatrix}, \tag{3.6}$$

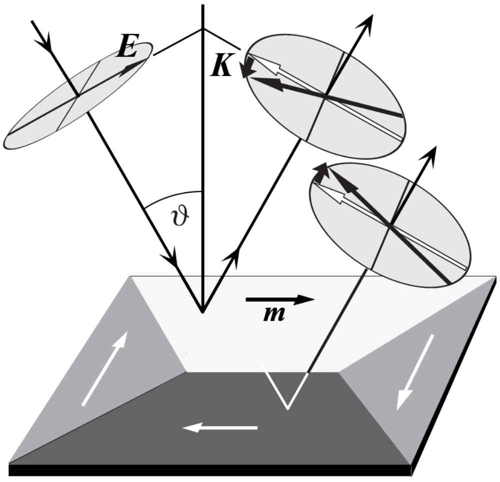

Figure 3.8: Illustration of the Kerr effect. When linearly polarised light with electric field vector ***E*** is illuminated on a magnetic surface with magnetisation vector ***m***, the reflected light is rotated to obtain a new vector ***K***. If the same is done for an oppositely magnetised surface, the rotation is reversed. Adapted from Ref. [117].

where $\tilde{\epsilon}$ is the dielectric tensor [116] for the magnetic medium with the off-diagonal elements being proportional to the magnetisation, ϵ is the dielectric constant for an isotropic medium and relates the displacement vector $\mathbf{D}$ with the electric field $\mathbf{E}$, Q is the Voigt constant which is proportional to the magnetisation, and $\mathbf{m}$ is the unit vector specifying the direction of magnetisation. In the second term of Equation 3.5, the cross product represents the action of a Lorentz force, which allows for a semi-classical explanation of the Kerr effect, that the incident polarised light causes the surface electrons to oscillate, and due to the Lorentz force resulting from the magnetisation of the surface, the polarisation of the reflected light is rotated.

Quantum mechanically, the Kerr effect is related to the spin-orbit interaction [118]. The magnetisation of the sample causes the two circularly polarised light to have different refractive indices in the sample. This is because opposite polarisations lead to equal but opposite energy contributions originating from spin-orbit coupling. Thus, they propagate at different velocities through the material. When they reflect out they carry a phase difference, which means that the polarisation axis of the reflected light is now rotated.

Depending on the measurement orientation, three forms (shown in Figure

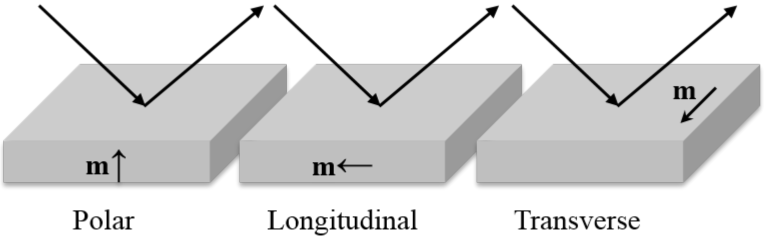

Figure 3.9: The three geometries of the magneto-optical Kerr effect. The short arrows represent the magnetisation direction of the sample. The long arrows represent the incident and reflected radiation.

3.9) of the Kerr effect exist: (i) The polar Kerr effect occurs when the magnetisation of the sample is perpendicular to the surface. It is independent of the polarisation of the incident light. (ii) The longitudinal Kerr effect occurs when the magnetisation is in-plane but parallel to the plane of incidence. (iii) The transverse Kerr effect takes place for the case when the magnetisation is parallel (in-plane) to the surface of the sample and perpendicular to the plane of incidence. Thus, no rotation takes place for the components of the light which are perpendicular to the plane of incidence.

3.4.2 Laser MOKE magnetometry

A laser MOKE magnetometer was used to measure the change in magnetisation of the samples as a function of applied magnetic field which results in hysteresis loops. Measurements were carried out in a dark room using a HeNe laser of wavelength 632.8 nm, and with water-cooled electromagnets with up to 550 mT field capability. Figure 3.10 shows the schematics of the experimental setup. Light from the laser is plane-polarised using a polariser and is allowed to shine on a sample placed in between two electromagnets. The reflected laser beam is then passed through another polariser (named here as analyser), which is set one to two degrees away from extinction depending on the intensity of the signal due to the Kerr rotation of the polarisation [119]. The final beam is fed into a photo detector which converts the photo-current into a voltage through an amplifier. This voltage is proportional to the magnetisation and is recorded as a function of the applied field using a computer to produce the desired hysteresis loop.

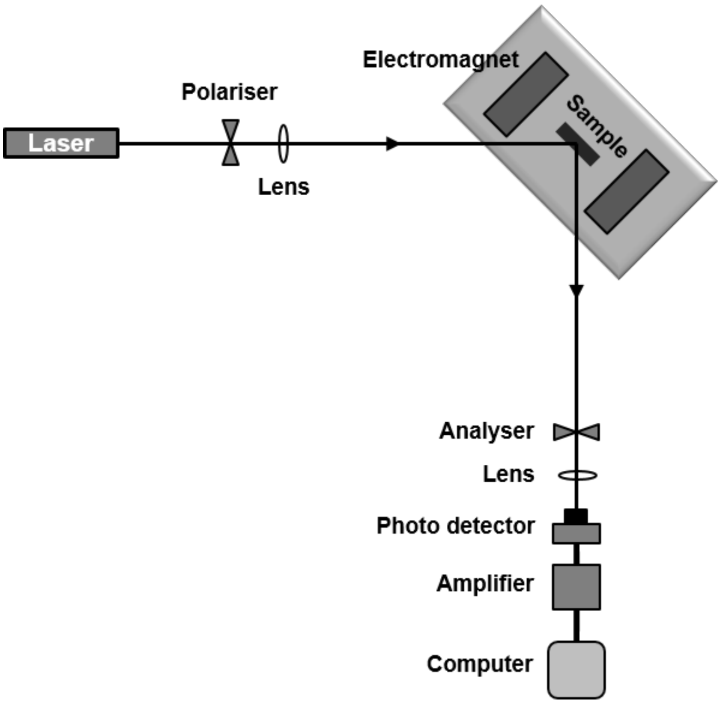

Figure 3.10: Schematics of the optical and electronic setup of the laser MOKE magnetometer.

3.4.3 Wide-field Kerr microscopy

A Kerr microscope is used to image magnetic domains in materials. It utilises the same magneto-optical principle and measurement mechanism. In general, a Kerr microscope is a standard optical microscope with added components to obtain magneto-optical sensitivity. Thus, a Kerr microscope is able to produce images with resolutions of micrometres or less, depending on the type and magnification of the objective lens used. There are two types of Kerr microscopes: wide-field [117] and laser-scanning [120]. The former type provides an image of a certain sample area at a time immediately, while laser-scanning microscopes use a laser spot to scan a certain sample area and sequentially build up the image. Wide-field Kerr microscopes are most commonly used as it is very versatile.

In this project, a commercial wide-field Kerr microscope from evico magnetics was employed. In this setup, a white light emitting diode light source is used. The reflected light from the sample is detected using a camera with a charge coupled device sensor and recorded on a computer. The produced images are in greyscale (Figure 3.11), where the intensity is proportional to the magnetisation of the magnetic domains of the sample. Hysteresis loops can also be obtained from the change of intensity of the images. A special aperture is used to tune the sensitivity to the different Kerr geometries. In addition to the optical components of the set-up, electromagnets for both in-plane and out-of-plane magnetic fields are installed. The strength of the field can be varied via the strength of the current through the coils of the electromagnets.

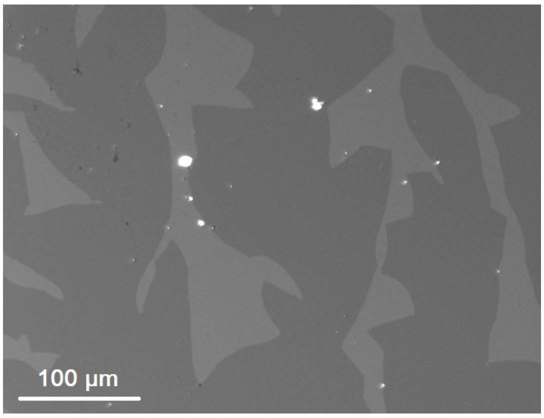

Figure 3.11: A wide-field Kerr micrograph showing the magnetic domains in a sample of Ta/CoFeb/MgO with perpendicular magnetisation. In this particular case, the bright regions are magnetised into the plane of the sample, while the dark regions are magnetised out of the plane.

Chapter 4

Interfacial atomic order influences the Dzyaloshinskii-Moriya interaction

4.1 Introduction

Ta/CoFeB/MgO is an interesting and useful system in which to study magnetic domain wall (DW) motion [121, 122]. It is technologically relevant as DWs can be driven with a low current density owing to its small coercivity due to a low density of DW pinning defects [123]. It is also widely used as an electrode in devices utilising magnetic tunnel junctions [124]. Thus, a combination of the techniques of efficient current-induced DW motion, and readout via tunnel magnetoresistance makes the material system a promising candidate for low power magnetic memory and sensors, especially DW and tunnel junction devices. Due to the presence of structural inversion asymmetry (SIA), Ta/CoFeB/MgO has been reported [125, 122] to possess the DMI, which is important to quantify as it influences the spin structure of a DW, and thus, its current-driven dynamics.

The DMI is sensitive to the atomic arrangements at the interface [36, 53]. An ordered atomic arrangement has been shown to enhance the DMI theoretically [51]. This work demonstrated this experimentally for Ta/CoFeB/ MgO. A systematic increase in the atomic order at the interfaces was brought about by annealing the films at different temperatures. Annealing causes the CoFeB layer, which is amorphous in the as-grown state, to crystallise [126, 101]. The DMI field was measured post-annealing and was found to respond to the changes in the interfacial atomic order. The DMI field is measured using a magnetic field-driven DW creep method. Annealing plays an important role in sample preparation and fabrication. It is generally required to produce a strong PMA in this system. Furthermore, sample heating is often a required step in nanofabrication procedures. Thus, it is important to find out how the DMI is affected by sample heating in Ta/CoFeB/MgO. An optimum annealing temperature was found for a maximum DMI in this material system. This chapter will describe in detail the results obtained, including an elaborate explanation of the experimental procedure used to measure the DMI. The chapter will also discuss the possible underlying mechanisms for the observed trend in the DMI by linking to anisotropy field measurements, which was also found to follow a similar trend as a function of the annealing temperature.

4.2 Multilayer system

The multilayer system investigated is that of a Ta(50 Å)/$Co_{20}Fe_{60}B_{20}$(8 Å)/MgO(20 Å), which is deposited on a thermally oxidised Si substrate. The system was sputter deposited by Singulus Technologies, Germany using a TIMARIS/ROTARIS tool. To prevent degradation of the MgO layer in ambient conditions and during annealing, a 50 Å Ta capping layer was deposited on top. The fabricated samples were then annealed (in the University of Leeds) in a furnace for 2 hrs in vacuum at a pressure of 8×10^{-6} Torr at the desired temperature and using a ramp rate of 5 °C/min. The as-deposited and the annealed samples possess a perpendicular magnetic anisotropy (PMA) as shown by the square magnetic hysteresis loops (Figure 4.1(a)) which are measured using a magneto-optical Kerr effect (MOKE) magnetometer in the polar configuration and thus making it sensitive to out-of-plane (OOP) magnetisation.

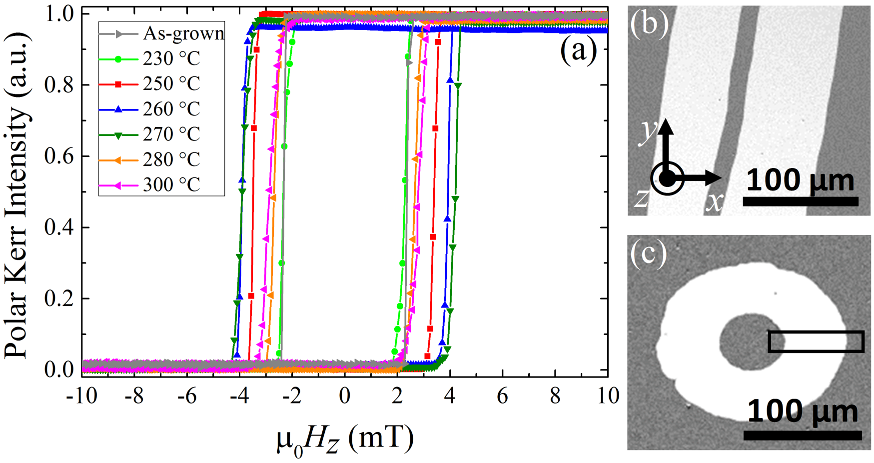

Figure 4.1: (a) Polar Kerr hysteresis loops of Ta/CoFeB/MgO system annealed at different temperatures. Kerr microscope difference images exhibiting 'line' domains (b) and 'bubble' domains (c) after a field pulse. The bright regions represent the areas swept by the DWs during the application of the field pulse. The black rectangle in (c) marks a section inside which DW displacements are measured in each pixel row and averaged.

In order to observe magnetic domains, magneto-optical imaging was done using a wide-field Kerr microscope in the polar configuration. The microscope is equipped with an electromagnet to generate an in-plane (IP) magnetic field and a custom home-built coil [127] to generate an OOP field. A difference image is generated using software, where images captured before and after a field pulse were subtracted.

The as-deposited film shows "line" domains (Figure 4.1(b)), whereas, the same film when annealed at a minimum temperature of 200 °C exhibits "bubble" domains (Figure 4.1(c)). In an as-grown film, due to the low density of defects, nucleation of domains occur at the sample edges, where there are more defect sites available. When two expanding domains, for instance, from opposite edges meet, they do not merge easily. This is because the DWs have the same chirality and thus, a topological energy barrier [43] exists between them, such that a much larger field is required, compared to the DW propagation field, in order to completely annihilate the DWs. As a result, when an as-grown film is incompletely saturated then such line domains occur, as reversal starts from two closely spaced DWs. However, in an annealed film, owing to crystallisation, defect sites are readily available within the film, from which domains can be nucleated. In this work, the technique used to measure the DMI (discussed later in Section 4.3), utilises bubble domains and thus, only annealed films where bubble domains can be nucleated were measured.

4.2.1 DW motion regime investigation

This section looks at the field-driven DW motion regimes of Ta/CoFeB/MgO. The experimental method used to quantify the DMI, and the theoretical model to describe the experiment takes place in the creep regime. It is thus important to confirm that the DW driving field used in the experiments is within the creep regime. In order to investigate the motion regimes, DW velocity was calculated for magnetic field pulses applied perpendicular to the sample plane (H_z). DW displacements at different pulse lengths were obtained from Kerr microscope difference images. DW velocities were then calculated by normalising the displacements by the field pulse times. Average DW velocities as a function of H_z is shown in Figure 4.3(a), for a 300 °C annealed sample. When $\ln v$ is plotted against $H_z^{-1/4}$ (Figure 4.2(b)) a linear behaviour is obtained till ≈2.3 mT, which validates that creep occurred within this region, where $\ln v \propto H^{-1/4}$ (refer to Section 2.4.1 for more details). The maximum driving OOP field used in the DMI measurement method is 1.8 mT, which is well within the creep field range.

The higher velocity regions were also identified from the acquired data. Figure 4.3(c) shows the plot of $\ln v$ vs H_z. The linear region in this plot identifies the TAFF regime, where $\ln v \propto H$. The beginning of the linear part marks the end of the creep regime, marked as $H_{\mathrm{C-T}}$, while the end of it represents the start of the depinning region at the depinning field H_{dep}. The critical field values associated with all the regimes identified here agree well with a report [123] for the same system and for the same composition of the FM layer ($\mathrm{Co_{20}Fe_{60}B_{20}}$).

4.3 Field-driven domain expansion technique

The DMI field is measured using a field-driven creep regime asymmetric expansion of magnetic domains, by lifting the energy degeneracy of DWs through the application of an in-plane field [35, 36]. To initialise a domain configuration for this method, the film is first saturated in a given direction. Then, a reverse field is applied to prepare a domain, either from one of the pre-reversed lines as mentioned in Section 4.2, or from a bubble at a defect. The DMI is measured using bubble domains, which can be nucleated only in annealed films. When a nucleated circular bubble domain is expanded under the application of an OOP field H_z, the expansion is isotropic, as depicted in Figure 4.3(a). This is because the DMI acts locally on a DW, and as a result, the DMI field H_{DMI} maintains radial symmetry with respect to the axis of expansion, which is parallel to the OOP field direction. When the same OOP expansion is performed but in presence of an applied IP field H_x, the symmetry is broken (Figure 4.3(b)). This is because the applied IP field either adds on to the DMI field, or acts against it. Thus, the effective IP field acting on the DW is strengthened ($H_x + H_{\mathrm{DMI}}$) on one side (right side in this case), causing the DW to travel with a higher velocity, compared to the DW on the other side, where the effective field is weakened ($H_x - H_{\mathrm{DMI}}$).

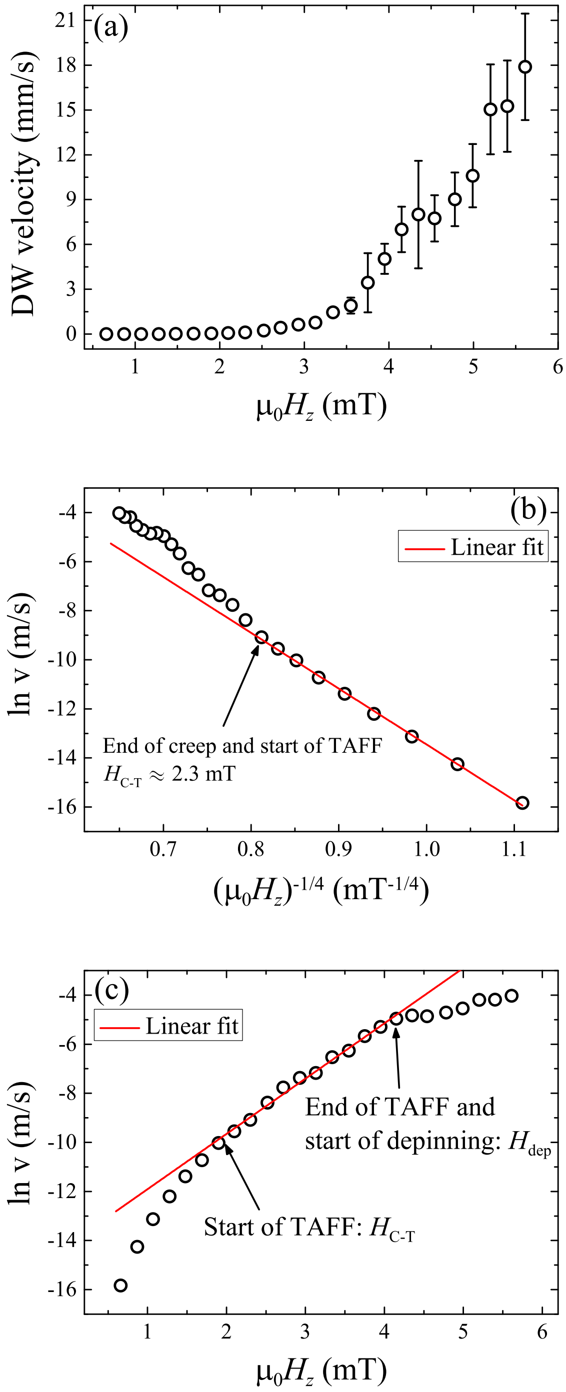

Figure 4.2: Field-driven DW motion regime investigation: (a) Plot of DW velocity v as a function of applied perpendicular field $\mu_0 H_z$. (b) Plot of $\ln v$ vs $\mu_0 H_z^{-1/4}$. Linear behaviour (red solid line) confirms DW creep motion till $\mu_0 H_z \approx 2.3$ mT. (c) Plot of $\ln v$ vs $\mu_0 H_z$. Linear part marks the TAFF region. The plots are for Ta/CoFeB/MgO annealed at 300 °C.

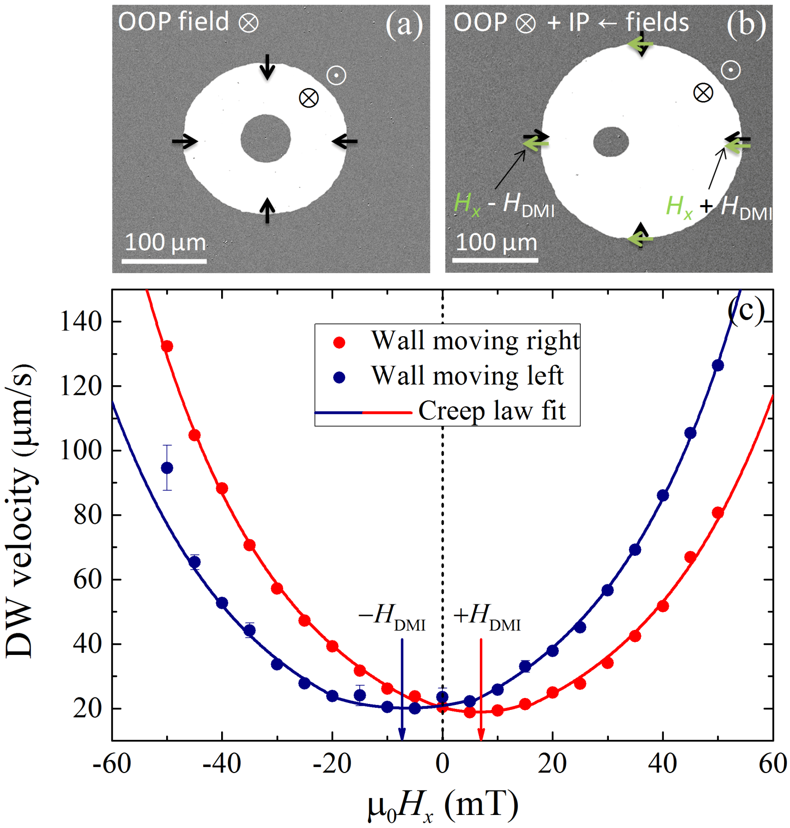

Figure 4.3: Kerr difference images showing: (a) isotropic expansion of a nucleated bubble domain by an OOP field pulse H_z. The bright region represents the area swept by an up-down DW during the field pulse. The black arrows represent the orientation of spins in the centre of an ideal Néel type DW due to the DMI field H_{DMI}; (b) asymmetric expansion when the same bubble is expanded but in presence of a static IP field H_x. The green arrows represent the action of the IP field on the DW spins. (c) DW velocity as a function of IP field H_x where the DW was driven with an OOP field pulse H_z of 1.4 mT. The error bars are from standard deviations of the average values. The solid lines are fits of the creep law. The minimum points of the plots mark the DMI fields H_{DMI} indicated by the red and blue arrows.

It is necessary that the IP field H_x is aligned in-plane as precisely as possible. A misalignment would generate an OOP component, which would affect the measurement technique itself, especially in systems with low coercivity like Ta/CoFeB/MgO. To align H_x, several steps are taken. First, the IP electromagnet is roughly aligned by using a bubble gauge. Next, the alignment is fine tuned by making sure DW motion does not occur at large $+H_x$ and $-H_x$. This step is particularly useful in magnetically soft systems, where the OOP component generated from a slight misalignment is enough to drive DWs. Finally, the distance propagated by a DW horizontally in an OOP field-expanded bubble domain under a particular $+H_x$ is compared against the distance in a bubble domain expanded under $-H_x$. The alignment is adjusted until the DW displacements are equal.

DW velocity is calculated from difference images as mentioned previously. To reduce errors, velocities are calculated for each row of pixels of a section (black rectangle in Figure 4.1(c)) and averaged using a Python script. This procedure is then repeated with different H_z pulse times and further averaged. The DMI field can be extracted by plotting the DW velocity as a function of IP field H_x, for a fixed OOP field which drives the DW. Such a plot, for a sample which has been annealed at 280 °C, is shown in Figure 4.3(c). The red and blue velocity plots represent DWs moving right and left, respectively. The effect of the DMI field can be observed by noticing that the axis of symmetry of the two plots shifts away from $H_x = 0$ in opposite directions. This offset of the minimum of each of the plot from $H_x = 0$ is a measure of H_{DMI}, since we assume that it is at this point the effective IP field acting on the DW is 0, as H_x cancels out H_{DMI}, resulting in the lowest DW velocity. This velocity is non-zero since the OOP field is still driving the DW. The minimum velocity, and thus H_{DMI} can be easily identified from the plot without the need of any further analysis. This makes the method very simple and robust. However, in order to accurately identify H_{DMI}, the experiment is modelled with the creep theory of DW dynamics, which is modified [35] to take into account the action of the DMI field and the applied IP field on the DW energy. The creep scaling law assumes that the DW is a 1D elastic interface moving in a 2D weakly disordered medium, and that at a low driving force, that is the applied field in this case, the DW velocity has an exponential dependence on it [103, 128]. The creep law is expressed as

$$v = v_0 \exp[-\zeta(\mu_0 H_z)^{-\mu}], \tag{4.1}$$

where $\mu_0 H_z$ is the applied OOP field, μ is the creep exponent which takes the value of $1/4$ for field-driven DW motion [103, 129, 104], the prefactor v_0 is the characteristic speed, and ζ is a scaling coefficient which is expressed as

$$\zeta = \zeta_0 \left[\sigma(H_x)/\sigma(0)\right]^{1/4}, \tag{4.2}$$

where ζ_0 is a scaling constant, and σ is the DW energy density per unit of surface. σ is modelled analytically using a 1D framework [41], where it is considered that the magnetisation does not vary significantly along the y- and z-directions. This is valid in the z-direction due to the strong perpendicular anisotropy of the system, but not in the y-direction. Thus, the model can be used only for the case of DWs moving on the x-direction. The DW energy density, as a function of the applied IP field H_x takes the general form of [41]

$$\sigma = \sigma_0 + 2\Delta K_\mathrm{D} \cos^2\phi - D\pi\cos\phi - \mu_0 M_\mathrm{s} \pi \Delta H_x \cos\phi, \tag{4.3}$$

where $\sigma_0 = 4\sqrt{AK_0}$ is the energy density of a Bloch wall, with A as the exchange stiffness and $K_0 = \mu_0 H_\mathrm{K} M_\mathrm{s}/2$ is the effective anisotropy, where $\mu_0 H_\mathrm{K}$ is the measured anisotropy field (discussed in Section 4.4) and M_s is the saturation magnetisation measured by a SQUID-VSM to be $M_\mathrm{s} = (6.50 \pm 0.04) \times 10^5$ A/m (Figure 4.5). The second term in Equation 4.3 represents the shape anisotropy energy density of the DW, where $\Delta = \sqrt{A/K_0}$ is the DW width and $K_\mathrm{D} = N_x \mu_0 M_\mathrm{s}^2/2$ (N_x is the DW demagnetisation factor) is the DW anisotropy favouring a Bloch wall, and ϕ is the azimuthal angle from the x-direction representing the magnetisation of the DW (Figure 4.4). The third term is the DMI energy density with $D = \mu_0 H_\mathrm{DMI} M_\mathrm{s} \Delta$ as the effective micromagnetic DMI constant [41]. The fourth term is the energy density of the applied longitudinal field.

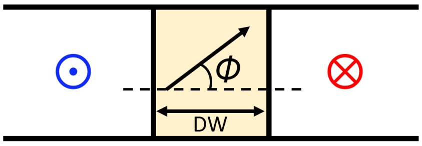

Figure 4.4: A domain wall (DW) is the region in yellow between the magnetised domains pointing up (blue) and down (red). The angle ϕ represents the magnetisation of the DW.

By minimising the DW energy density (Equation 4.3) with respect to ϕ, the equilibrium state of the DW under the applied IP field can be obtained

$$\frac{\mathrm{d}\sigma}{\mathrm{d}\phi} = \sin\phi(\mu_0 M_\mathrm{s}\pi\Delta(H_x + H_\mathrm{DMI}) - 4\Delta K_\mathrm{D}\cos\phi) = 0, \tag{4.4}$$

which results in two solutions

$$\phi = \begin{cases} 0 \text{ or } \pi, & \text{when } |H_x + H_\mathrm{DMI}| > 4K_\mathrm{D}/\mu_0 M_\mathrm{s}\pi \\ \arccos(\frac{\mu_0 M_\mathrm{s}\pi(H_x+H_\mathrm{DMI})}{4K_\mathrm{D}}), & \text{when } |H_x + H_\mathrm{DMI}| < 4K_\mathrm{D}/\mu_0 M_\mathrm{s}\pi \end{cases}. \tag{4.5}$$

Inserting $\phi = 0$ or π in Equation 4.3, the expression for the Néel wall energy density can be obtained

$$\sigma_\mathrm{N} = \sigma_0 + 2K_\mathrm{D}\Delta - \mu_0 M_\mathrm{s}\pi\Delta|H_x + H_\mathrm{DMI}|, \tag{4.6}$$

while the other solution gives the energy density for the Bloch wall

$$\sigma_\mathrm{B} = \sigma_0 - \frac{\mu_0^2 M_\mathrm{s}^2 \pi^2 \Delta}{8K_\mathrm{D}}(H_x + H_\mathrm{DMI})^2. \tag{4.7}$$

This means that for the condition

$$|H_x + H_\mathrm{DMI}| < \frac{4K_\mathrm{D}}{\mu_0 M_\mathrm{s}\pi} \tag{4.8}$$

the total effective IP field acting on the DW $(H_x + H_\mathrm{DMI})$ is not sufficient to transform a Bloch wall into a Néel wall. This is at relatively low applied IP fields. The spin structure of the DW in such a case is in a Bloch-Néel mixed state and the DW energy is expressed by Equation 4.7. Otherwise,

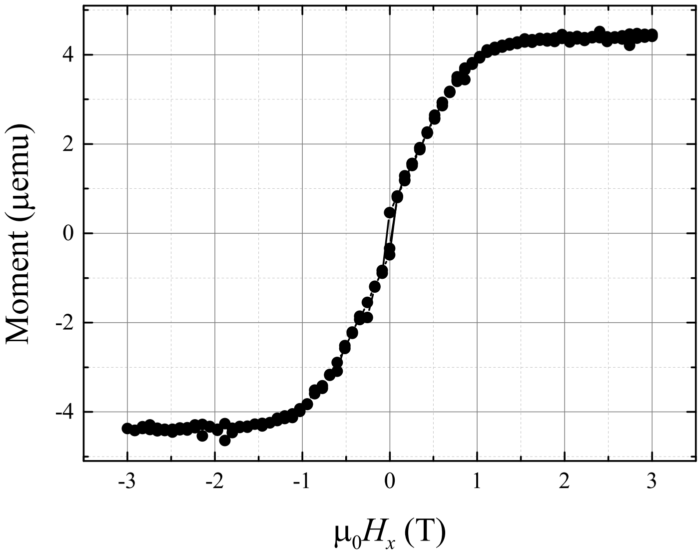

(a)

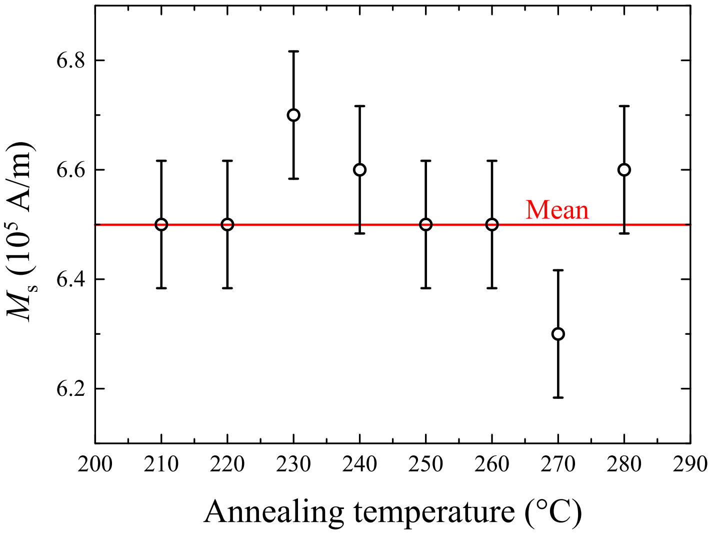

(b)

Figure 4.5: (a) SQUID-VSM moment vs IP field hysteresis loop of an OOP magnetised Ta/CoFeb/MgO sample annealed at 280 °C from which the saturation magnetisation M_s is obtained. (b) M_s of samples annealed at different temperatures from which a mean value (red line) of $M_\mathrm{s} = (6.50 \pm 0.04) \times 10^5$ A/m is calculated. The error bars are from the standard deviation of the distribution of data, while the uncertainty in the average value is from the standard error.

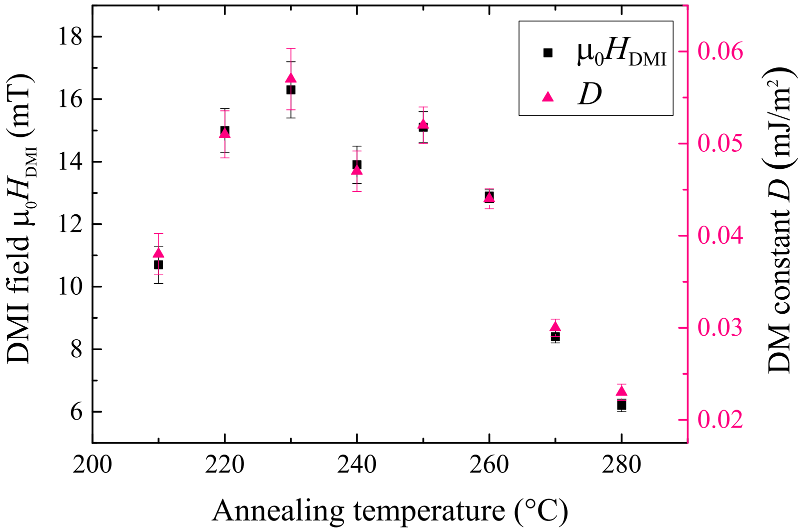

Figure 4.6: DMI field $\mu_0 H_{\text{DMI}}$ (black squares) and the DM constant D (pink triangles) as a function of annealing temperature. The uncertainties in the DMI fields are from standard erros.

when $(H_x + H_{\text{DMI}})$ is sufficient to stabilise a Néel wall, the DW energy is expressed by Equation 4.6.

The experimental data fits well with the DW creep model as shown in Figure 4.3(c) (solid lines) where v_0, ζ_0, and H_{DMI} are the three fitting parameters used. The DMI field H_{DMI} was subsequently extracted from the fits. These are marked on the respective plots by red and blue arrows. The effective DM constant D was consequently calculated by using the expression $D = \mu_0 H_{\text{DMI}} M_s \Delta$ [41].

Figure 4.6 shows the variation of the DMI field H_{DMI} (black), and the DMI constant D (pink) with regard to the annealing temperature. As the temperature in increased the DMI gradually rises from $D = 0.038 \pm 0.002$ mJ/m^2 at a temperature of 210 °C, reaches a peak value of $D = 0.057 \pm 0.003$ mJ/m^2 at 230 °C, and then decreases back with further increase in temperature. The DWs in this system are determined to have a right-handed chirality and thus the sign of D is positive, as per convention. The chirality of the DW can be deduced from the applied OOP and IP field directions. The magnitude and sign of the DMI agrees well with previous reports [122, 125] in

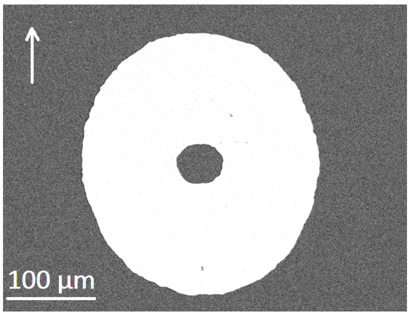

Figure 4.7: Elliptical, rather than circular, domain expansion showing the presence of an IP uniaxial anisotropy. The image is that of a Ta/CoFeB/MgO film annealed at 300 °C, where a nucleated circular domain is expanded using only an OOP field. The white arrow shows the easy axis of anisotropy.

the same system.

4.3.1 In-plane uniaxial anisotropy

It is worthwhile to mention that some of the measured samples exhibit a small IP uniaxial anisotropy, which is evident in an OOP-field expansion of a bubble domain, as it causes a slightly elliptical, rather than a circular expansion. This is depicted in Figure 4.7. The anisotropy is acquired due to the substrate being moved horizontally during deposition which was a necessary step. It is thus necessary to investigate if the anisotropy brings about a change in the DMI measurements, especially in the obtained DMI field values. To do this, the in-plane easy axis of the film was rotated with respect to the applied horizontal IP field, and for each rotation the DW v vs H_x measurements were performed using the same value of OOP field and the same range of IP fields. The data for the 300 °C annealed film is shown in Figure 4.8 (top row). From the data it can be concluded that the minimum of the plot, that is, the DMI field remains the same irrespective of the position of the IP easy axis with respect to the applied IP field. This behaviour, however, is expected since the longitudinal DMI field acts locally on the DW position and thus, is radially symmetric for a DW curvature.

The data also shows an expected shift in the velocity plots as the easy axis is rotated. The shifts are due to the DWs moving a bit faster along the IP

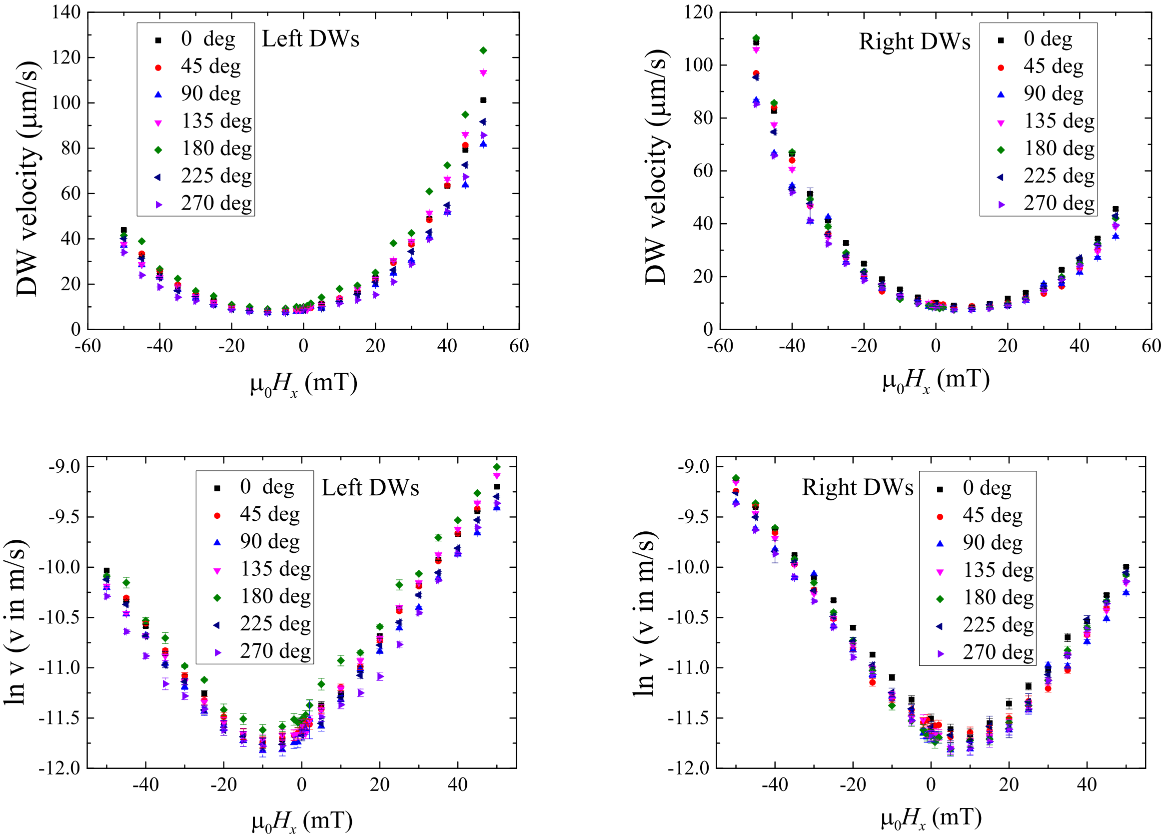

Figure 4.8: Plots of DW v vs H_x (top row) and ln$v$ vs H_x (bottom) for DWs moving left and right. Each colour refers to the angle of the IP easy axis with respect to the IP field. A shift in the plots is observed which is due to the presence of the acquired IP uniaxial anisotropy. However, the minimum velocity, at which the IP field cancels the DMI field, remains the same.

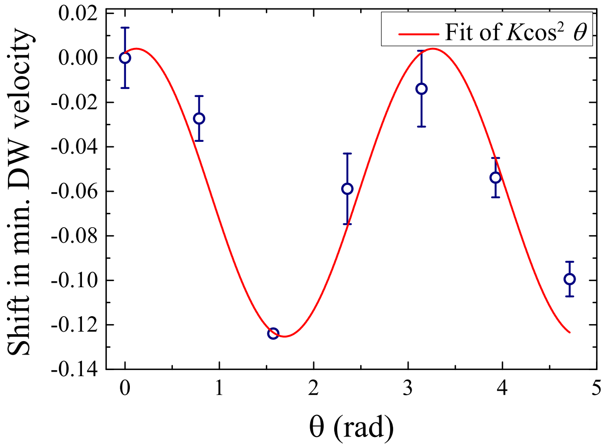

Figure 4.9: Shift in the minimum velocity points from Figure 4.8 (bottom row) plotted against their respective angle. The data follows a cosine squared relation representing a uniaxial anisotropy.

easy axis relative to the IP hard axis. The shifts are more evident in plots of ln v vs H_x, shown in Figure 4.8 (bottom row). From these plots, the average shift from a left and a right moving DW is then plotted against the respective angle of rotation which shows the typical cosine squared relation of uniaxial anisotropy. The plot is shown in Figure 4.9.

4.4 Magnetic anisotropy measurement technique

To investigate the obtained trend in the DMI, the anisotropy field of the samples annealed at different temperatures was measured. An increase in the magnetic anisotropy indicates an increase in atomic order at the interface in this material system [130, 126]. The anisotropy field was measured magneto-optically utilising coherent rotation of magnetisation at a low field range. The section will elaborate on the method.

The field required to coherently rotate the magnetisation from the easy axis to the hard axis is the magnetic anisotropy field $\mu_0 H_K$. The anisotropy constant is calculated from $\mu_0 H_K M_s/2$. This is the effective anisotropy which incorporates contributions from surface, volume, and shape anisotropy. The anisotropy field was measured magneto-optically using the Kerr microscope for a low field range over which the magnetisation rotates coherently. In this method, the Kerr microscope is set up in the polar configuration so that the OOP component of the magnetisation m_z is measured. In this configuration, m_z is continuously measured while an IP field H_x sweep is performed in order to rotate the magnetisation from the easy (OOP) to the hard axis (IP). Before the application of the IP field, the magnetisation of the sample is saturated along the OOP easy axis using an OOP field H_z. This results in the maximum value of m_z, while the value of the IP component of the magnetisation m_x is zero. Now, as H_x is increased, the sample magnetisation starts to rotate IP and consequently m_z gets smaller in magnitude until nucleation of domains would start to occur causing a sharp drop in m_z. At this point H_x is sufficiently strong to rotate the magnetisation of the entire system IP.

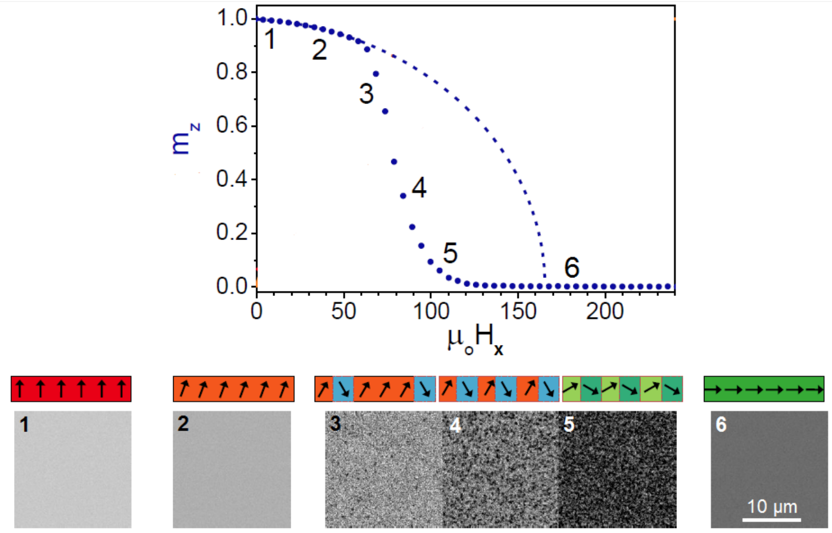

Figure 4.10: The plot shows the normalised polar Kerr signal probing the OOP component of magnetisation m_z. The blue dots are data points showing the decrease in the signal caused by the rotation of magnetisation from OOP to IP due to the application of an IP field. The dashed blue line is a simulation of coherent rotation of magnetisation from OOP to IP derived by assuming that the total magnetisation is $\mathbf{m}^2 = m_z^2 + m_x^2 = 1$. Thus, the x-intercept represents the anisotropy field. The set of figures at the bottom shows Kerr images and the respective illustrations of the magnetisation rotation process. The magnetisation initially rotates coherently before breaking into domains which is characterised by the sharp drop of the Kerr signal in the plot. Figure adapted from ref. [131].

This is shown as an example in Figure 4.10, where successive Kerr difference images are shown for a pre-OOP-saturated sample. At $H_x = 0$ (image 1) the image is bright and uniform, indicating OOP saturation of magnetisation (m_z = maximum). With the increase of H_x the image becomes darker due to a decrease in the Kerr intensity as m_z gets smaller. However, the image stays uniform depicting that the magnetisation is rotating coherently. This uniformity disappears when H_x is increased further. The image exhibits bright and dark specs due to the formation of small up and down canted domains in order to lower the energy of the system. At this point, the Kerr signal drops rapidly as more of these canted domains form until the magnetisation of the entire system switches, at which point the image becomes uniform again. Thus, the low field data is extrapolated (blue dashed line), assuming that the magnetisation rotates coherently in this regime, i.e. $\mathbf{m}^2 = m_z^2 + m_x^2 = 1$, and the anisotropy field $\mu_0 H_\mathrm{K}$ is obtained from the x-intercept.

4.5 Effect of anisotropy on the DMI

The anisotropy field follows a similar trend as the DMI, as a function of the annealing temperature, as shown in Figure 4.11 (top) with an example measurement (bottom). It shows a peak in magnitude at about the same temperature range as the peak in the DMI. Such a trend of the anisotropy field was also reported by Avci *et al.* [130], but for a smaller temperature range.

The initial rise in the anisotropy field is due to an enhancement of the crystal ordering of the CoFeB and MgO layers brought about by annealing [126, 101]. Such a behaviour was previously reported [130, 126] in this system. Crystallisation of the CoFeB layer is also brought about by B diffusion from the CoFeB layer into the adjacent layers, especially into Ta as it is a B sink [132]. Segregation of B into the adjacent layers, in Ta/CoFeB/MgO, was observed by chemical depth profiling by LoConte *et al.* [122]. An improved atomic order in these two layers causes a rise in the anisotropies at the MgO/CoFeB and CoFeB/Ta interfaces. These two interfaces both contrib-

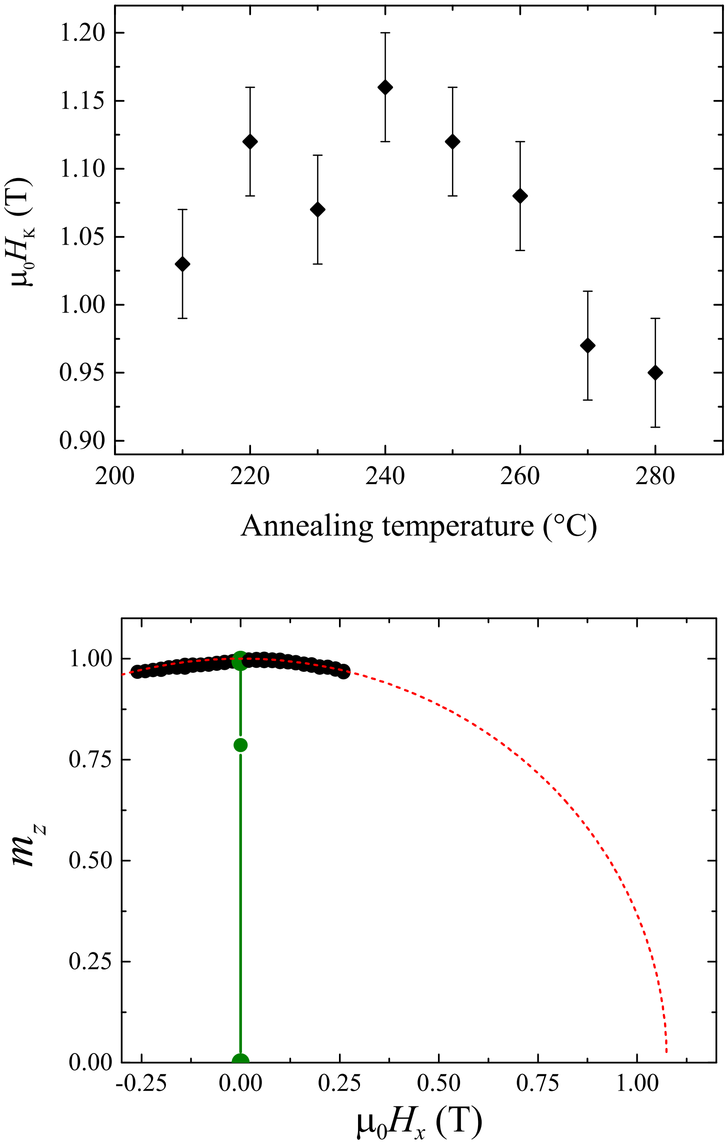

Figure 4.11: Top: Effective anisotropy field $\mu_0 H_K$ vs annealing temperature. The variation is similar to H_{DMI} vs annealing temperature. The error is obtained from the quality of the fit and by performing repeated measurements. Bottom: Plot of (normalised) OOP magnetisation m_z vs IP field $\mu_0 H_x$. The OOP magnetisation was probed using a Kerr microscope in the polar settings. Before applying the IP field, the magnetisation was saturated along the easy z-axis using an OOP field $\mu_0 H_z$ (green data points). This ensured a maximum value of m_z, while $m_x = 0$. The red dashed line is the extrapolation of the plot assuming that the magnetisation rotates coherently as the IP field is increased. Hence, the x-intercept represents the anisotropy field.

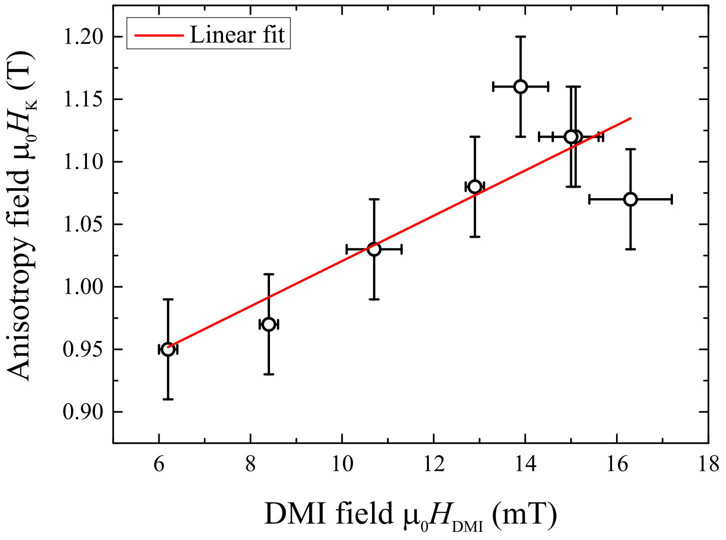

Figure 4.12: Plot of the anisotropy field $\mu_0 H_K$ vs the DMI field $\mu_0 H_{DMI}$. The two quantities follow a linear relationship with respect to the annealing temperature.

ute to the perpendicular magnetic anisotropy of the system [101, 133] and hence, we observe an increase in the overall anisotropy with increasing annealing temperature. However, annealing the samples at even higher temperatures causes a decrease in the magnetic anisotropy. This to due to a combined effect of B deposition [122] and intermixing [101] at both the MgO/CoFeB and CoFeB/Ta interfaces as the films are annealed at relatively high temperatures.

The DMI field and the anisotropy field are strongly correlated with each other, as a function of temperature. This is depicted in Figure 4.12. From the inter-relationship of the DMI field and the anisotropy field, we deduce that the observed variation in these two quantities have common underlying mechanisms. The DMI is sensitive to interfacial atomic order [36, 53] and thus, an enhancement in the atomic arrangements at the Ta/CoFeB interface, due to annealing, results in the initial improvement of the DMI. It is accepted that the DMI is present at the HM/FM interface [33, 34], however, very recent studies report [38, 39] that a FM/Oxide interface can also generate a sizeable DMI. Thus, for Ta/CoFeB/MgO, a more ordered CoFeB/MgO top interface also contribute to the initial enhancement of the DMI as a result of annealing. Here it is appropriate to mention that in symmetric Pt/Co/Pt systems, Hrabec *et al.* [36] found the DMI to vanish for epitaxially grown ordered interfaces, when compared to disordered polycrystalline interfaces. However, since the system was symmetric, the polycrystalline stack exhibited the DMI due to an asymmetry in disorder between the top and the bottom interfaces. For the ordered epitaxial stack, the DMI was probably enhanced at the two interfaces individually, but cancelled each other as they are symmetric, resulting in a zero net DMI.

The DMI field decreases as the films are annealed at even higher temperatures; similar to the anisotropy field. The accumulation of B at both the Ta/CoFeB and CoFeB/MgO interfaces becomes significant since the B accumulation acts as a barrier to the interaction between the atoms lying at the interfaces of the involved layers. Furthermore, higher temperature annealing results in intermixing [130] at the interface, which has been reported [51] to be detrimental for the DMI. Thus, these are the two factors which together contribute to the weakening of the DMI at relatively high annealing temperatures.

4.6 Conclusion

This chapter demonstrates how the interfacial DMI in perpendicularly magnetised Ta/CoFeB/MgO multilayer is affected by the atomic arrangement at the interface between two layers. Changes in atomic order was brought about by annealing the films systematically at different temperatures ranging from 210-280 °C. Then, DMI fields were measured using a field-driven method in the creep regime by breaking the energy symmetry of an expanding bubble domain by using an applied IP field. The different regimes of DW dynamics was thoroughly investigated for the system in order to ensure that DW motion occurred within creep during DMI field experimentation.

From the measurements it was found that a maximum DMI was achieved at a temperature of around 230 °C. It is inferred that the initial rise of the DMI as a function of temperature is related to an improved crystal order at the interfaces, while the DMI decreases at higher temperatures due to the segregation of boron out of the CoFeB layer and consequent accumulation at the adjacent interfaces of Ta/CoFeB and CoFeB/MgO. The boron accumulation acts as a disruption between the layers responsible for the generation of the DMI. This mechanism is supported by anisotropy field measurements which was found to follow a similar trend and peaking in magnitude at around the same temperature range as the DMI field. This work gives us concrete experimental evidence of how the DMI is sensitive to the interfacial atomic order.

The presence of an acquired IP anisotropy was also investigated and was found not to influence the DMI measurement technique.

Chapter 5

Development of systems with perpendicular exchange bias

5.1 Introduction

The use of an antiferromagnet (AFM) as an active element in functional devices is an emerging branch of spintronics [134, 135]. AFMs possess certain physical properties, which we can take advantage of and venture into new directions in spintronic device applications. AFMs allow the generation of large spin currents through which magnetisation in an adjacent ferromagnet (FM) layer can be efficiently switched [49, 136, 92]. Furthermore, there are no stray fields associated with AFM materials since the net magnetisation is zero due to the compensation of magnetic moments at the atomic level. In a FM, such interfering fields may cause device malfunctions brought about by, for example, crosstalk between neighbouring devices, susceptibility to external magnetic fields, etc. Thus, eliminating stray fields through the use of AFMs could prove to be vital in integrated devices with low dimensions. Also, the typical frequency of magnetisation dynamics in AFMs is in the terahertz range, suitable for ultrafast information processing [84].

This project aims to exploit some of these properties by incorporating AFM materials in multilayer film systems. One way to do this is by manipulating the magnetisation of a FM by an AFM through interfacial coupling [87] between the two layers. For this, polycrystalline systems of Pt/Co/IrMn and Pt/Co/FeMn are fabricated and investigated which exhibit perpendicular magnetic anisotropy (PMA) and perpendicular exchange bias (PEB) [137, 138, 81, 139]. In these multilayers, the efficiency of current-driven DW motion might be increased by combining the phenomenon of enhanced spin-orbit torques (through the use of AFM materials), and the existence of homochiral Néel walls (through the presence of the DMI). Furthermore, the coincidence of the DMI with a vertical exchange field could replace the need for an externally applied field to stabilise skyrmion bubbles [45]. In order to achieve enhanced spin torques, a combination of a Pt heavy-metal layer and a Mn-based AFM (IrMn and FeMn) layer was used which has been shown to generate large spin currents [140, 49, 136, 141]. These AFMs also exhibit a large exchange bias (EB) when coupled to a FM [142, 139, 143]. Further to this, the Pt layer was used in order to realise a perpendicular anisotropy in the system [31], and also to obtain a sizeable DMI [37, 36].

In this foundational study, the dependence of PMA, PEB and DMI on layer thickness was examined in the chosen trilayers. The work done in this project is divided into two chapters. In this chapter, the growth, layer thickness optimisation, and structural and magnetic characterisation of these systems will be discussed in detail. The link between the structural and the magnetic properties will then be explored. This should serve as important information in order explain the interfacial mechanisms, such as EB and DMI, which will be discussed in the next chapter. Structural characterisation is realised using X-ray reflectivity and diffraction while magnetic properties are characterised by laser MOKE magnetometry, vibrating sample magnetometry, and magneto-optical imaging. The individual layer thicknesses were adjusted to obtain a strong PMA and a large PEB in these stacks in the as-grown state. Different phases of the AFM layer are characterised by identifying the Néel temperatures (T_{N}) and the blocking temperatures (T_{B}) of the layers at different layer thicknesses.

5.2 Fabrication of Pt/Co/IrMn

The trilayer polycrystalline system of Pt/Co/$\mathrm{Ir_{20}Mn_{80}}$ was deposited by magnetron sputtering on a thermally oxidised Si substrate, at a base pressure of 2×10^{-8} Torr, and at an Ar working pressure of 2.5×10^{-3} Torr. The layers were grown on a 50 Å Ta seed layer in order to facilitate a (111) texture for the Pt and Co layers, and consequently for the IrMn layer. Such a crystalline texture of IrMn [144] (and also FeMn [145]) offers the largest areal density of spins at the interface, and thus provides for an enhanced exchange coupling with the Co layer resulting in a large exchange bias. Also, a (111) orientation of Pt is required to facilitate PMA [146] in Pt/Co bilayers. Figure 5.1 is a high angle X-ray scan of a sample showing the Pt(111) and IrMn(111) peaks. Lastly, a capping layer of at least 30 Å of Pt or Ta was also deposited on top of the stacks in order to prevent oxidation. A change in capping layer does not influence the magnetic properties which are measured here.

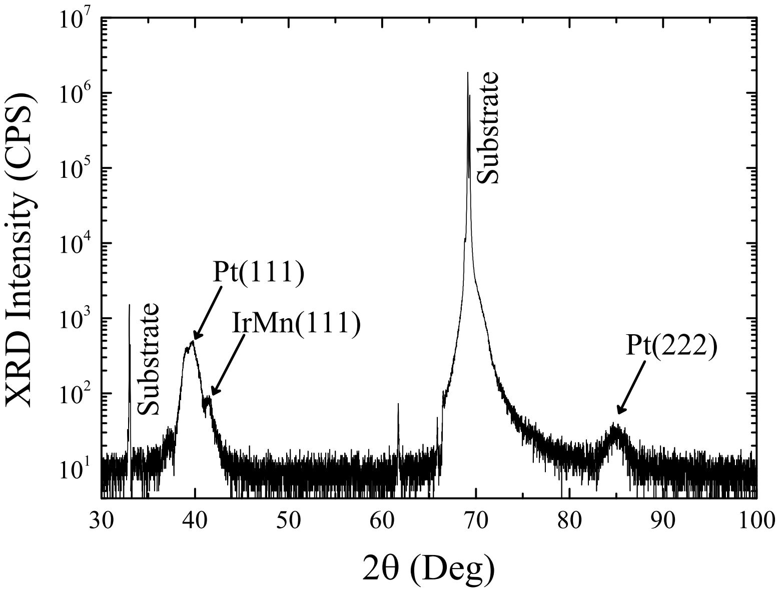

Figure 5.1: X-ray diffraction of polycrystalline Ta(50 Å)/Pt(50 Å)/Co(10 Å)/IrMn(50 Å)/Pt(50 Å) from which the (111) texture of the IrMn layer may be confirmed.

The thickness of individual layers of the grown samples was assessed by low angle X-ray reflectivity (XRR) measurements. Figure 5.2 shows representative XRR scans for two samples of Ta(50 Å)/Pt(50 Å)/Co(10 Å)/IrMn(t_{IrMn})/Pt(50 Å), where t_{IrMn} = 60 Å (top) and 10 Å (bottom). Interference of reflected X-rays from each interface results in a convolution of Kiessig fringes, as discussed in Section 3.3.3. By fitting the data with a model of the multilayer system [147], the thickness of the individual layers can be evaluated. The extracted layer thicknesses from the fits for the two samples, along with other parameters, are shown in Table 5.1. The extracted thicknesses agree well with the nominal thicknesses.

Care should be taken when evaluating layer thickness in such a way since the model used may not be accurate as additional layers resulting, for example, from oxidation, alloying, etc., are not taken into account. On the other hand, inclusion of such additional layers increases the number of fitting parameters, which in turn, decreases reliability. The ideal approach to achieve accuracy in layer thickness is to carefully calibrate the sputter rates of the materials. Thus, sputter rates for each individual layer were calibrated before each growth run.

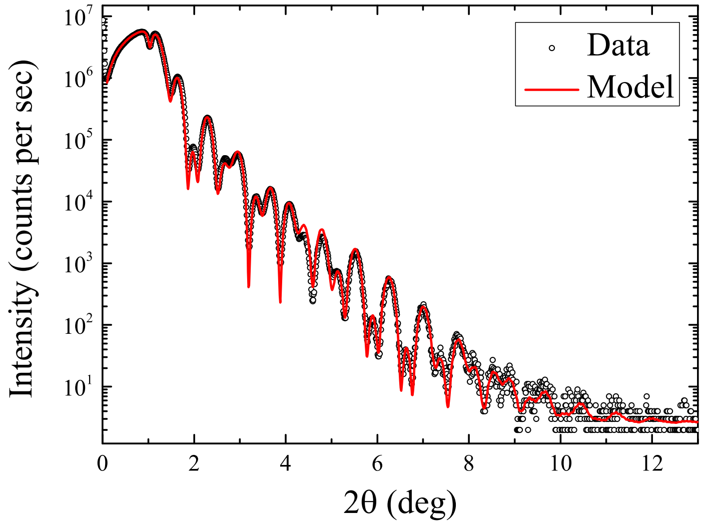

(a)

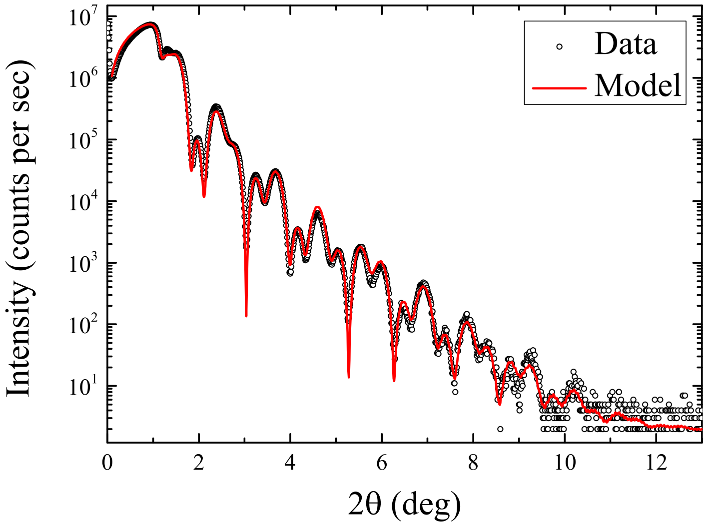

(b)

Figure 5.2: X-ray reflection scans and fits of (a) Ta(50 Å)/Pt(50 Å)/Co(10 Å)/IrMn(60 Å)/Pt(50 Å), and (b) Ta(50 Å)/Pt(50 Å)/Co(10 Å)/IrMn(10 Å)/Pt(50 Å).

Table 5.1: Extracted parameters from the fits of the XRR data of Figures 5.2(a) and (b), respectively. The value of roughness in the PtO_2 layer is larger than the thickness. This indicates a discontinuous layer of PtO_2.

(a)

Material	Thickness (Å)	Density (%)	Roughness (Å)
Si	∞	98.5	0.0
SiO_2	938.3	89.3	2.6
Ta	51.1	80.8	8.1
Pt	56.0	98.5	3.4
Co	10.6	96.8	2.6
IrMn	61.4	99.6	6.9
Pt	54.6	100	3.5
PtO_2	1.6	97.7	3.9

(b)

Material	Thickness (Å)	Density (%)	Roughness (Å)
Si	∞	97.6	0.0
SiO_2	984.4	87.9	3.6
Ta	51.7	81.1	7.5
Pt	57.4	96.7	3.5
Co	10.0	99.8	4.0
IrMn	10.3	97.2	6.8
Pt	56.6	99.9	4.6
PtO_2	1.2	98.2	2.5

5.2.1 Optimisation of perpendicular magnetic anisotropy

In a system with Pt/Co, the perpendicular magnetic anisotropy is due to the Pt 5d-Co 3d hybridisation, which is localised at the Pt/Co interface [31]. The hybridisation enhances orbital magnetisation of Co, leading to PMA. The enhancement of orbital magnetisation decreases with increasing Co layer thickness, causing the loss of perpendicular anisotropy when it is too thick [31]. Thus, in order to obtain a strong perpendicular anisotropy in this system, an optimum thickness of Co layer was chosen. For this, the Co layer thickness (t_{Co}) was systematically varied, while the thicknesses of the other layers were kept constant. The IrMn layer was 50 Å thick, at which the system exhibit an exchange bias (EB) field at room temperature. The result for Ta(50 Å)/Pt(20 Å)/Co(t_{Co})/IrMn(50 Å)/Pt(50 Å) is shown in Figure 5.3 (b), where coercive fields (H_c) are plotted against Co layer thickness. The coercive fields are obtained from easy axis polar MOKE magnetic hysteresis loops, depicted in Figure 5.3 (a). It is half the difference between the two switching fields. Films with Co thickness ranging from 8-14 Å exhibit perpendicular magnetisation characterised by square, easy axis loops. Outside this range the system loses out-of-plane anisotropy, which is characterised by hard axis loops. From this investigation, the working Co thickness was chosen to be t_{Co} = 10 Å, at which the coercivity is at its peak value, and thus the system provides a stable perpendicular magnetisation.

The perpendicular orientation of the spins in the Co layer sets the orientation of the IrMn spins in contact with the Co layer normal to the plane, which results in a perpendicular exchange bias (PEB). The PEB is present in the samples in the as-grown state and does not require any post-growth processing, such as field cooling. The EB decreases when the Co layer thickness increases, in the range where the PMA is dominant, as shown in Figure 5.3 (c).

5.2.2 Antiferromagnetic layer thickness dependence

The thickness of the AFM layer is related to its spin order. When the layer is thin enough, the Néel temperature T_N moves below room temperature, which results in paramagnetic behaviour at room temperature. The spin order of the AFM layer, in turn, influences the interactions at the FM/AFM interface, and thus the magnetic properties. To investigate this, the IrMn layer thickness (t_{IrMn}) was varied from 10-100 Å, while the thickness of all other layers were kept fixed, for Ta(50 Å)/Pt(20 Å)/Co(10 Å)/IrMn(t_{IrMn})/Pt(50 Å). Coercive fields (H_c) and EB fields (H_{ex}), extracted from polar MOKE hysteresis loops, are presented in Figure 5.4(b), as a function of IrMn layer thickness. H_{ex} is the shift of a hysteresis loop from H = 0.

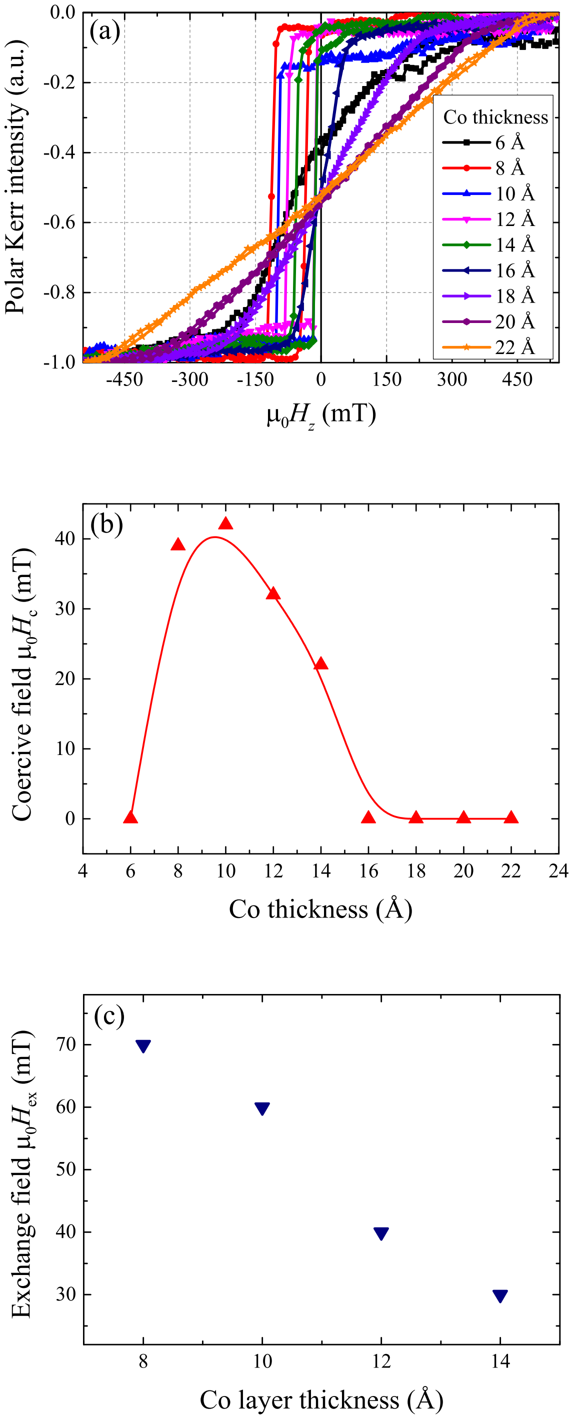

Figure 5.3: (a) Polar MOKE hysteresis loops for Ta(50 Å)/Pt(20 Å)/Co(t_{Co})/IrMn(50 Å)/Pt(50 Å). Films with Co thickness from 8-14 Å exhibit PMA. (b) Coercive fields as a function of Co layer thickness. The solid line is a guide to the eye. (c) EB field as a function of Co layer thickness, for the samples with PMA. The uncertainties are smaller than the size of the data points.

In order to accurately identify the different phases of this exchanged biased system, a second run of sample fabrication was performed, where the IrMn layer thickness was changed in smaller increments than the previous run. A second growth run was necessary due to the limitation of the sputtering machine. The data for the second run is shown in Figure 5.5.

The combined data for the two growth runs is presented in Figure 5.6. From the data it can be observed that at ≈23 Å of IrMn, EB starts to develop in the system. From this thickness onwards, H_{ex} rises steadily and stabilises at 35 Å, with a value of $\mu_0 H_{\mathrm{ex}} = 50$ mT. There is an initial sharp enhancement in coercivity, which peaks at the same 23 Å of IrMn, at which the onset of the EB occurs. After peaking, H_{c} drops rapidly to a saturation value of $\mu_0 H_{\mathrm{c}} = 40$ mT at the thickness of 35 Å, at which thickness the EB field also stabilises.

The initial rise in coercivity is due to the onset of the AFM phase of IrMn and coupling with the Co layer. At 10 Å layer thickness the IrMn is in its paramagnet (PM) phase with no spin order. With the increase in thickness, AFM spin order sets in, resulting in an exchange interaction at the Co/IrMn interface. This PM to AFM phase transition is marked by the enhancement in coercivity, which starts at ≈17 Å of IrMn. At this point, as the Co layer is switched, it also drags the coupled spins of the IrMn layer along with it, causing the enhancement in coercivity. This is possible for the Co layer since the volume anisotropy energy of the AFM layer (K_{AFM}) is smaller compared to the exchange energy at the interface between the FM and the AFM ($J_{\mathrm{FM/AFM}}$). Increasing the IrMn thickness further, causes K_{AFM} to become larger, resulting in further rise in coercivity. This trend continues until a critical thickness of ≈23 Å is reached, when K_{AFM} becomes so large that it is no longer energetically favourable for the Co layer to drag the IrMn spins. From this critical thickness onward, K_{AFM} is sufficiently large to resist the torque from the FM Co layer ($K_{\mathrm{AFM}} > J_{\mathrm{FM/AFM}}$). Thus, a decrease in coercivity is observed in the system, along with the introduction of the EB field. The trends obtained closely match with reports [142] for similar systems with in-plane magnetisation.

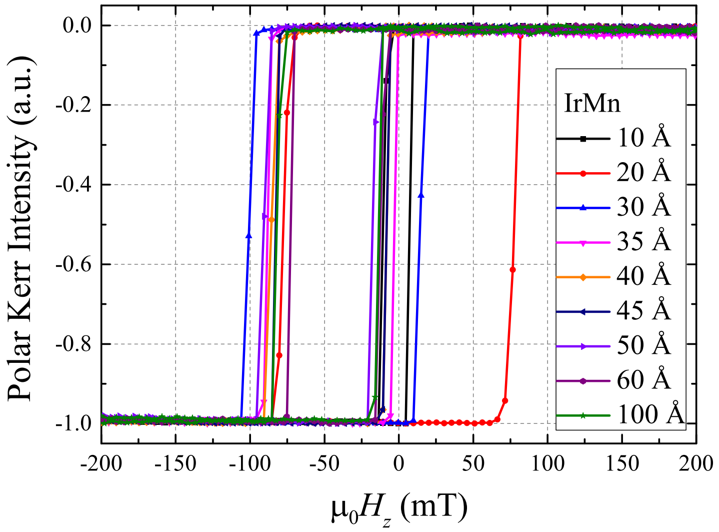

(a)

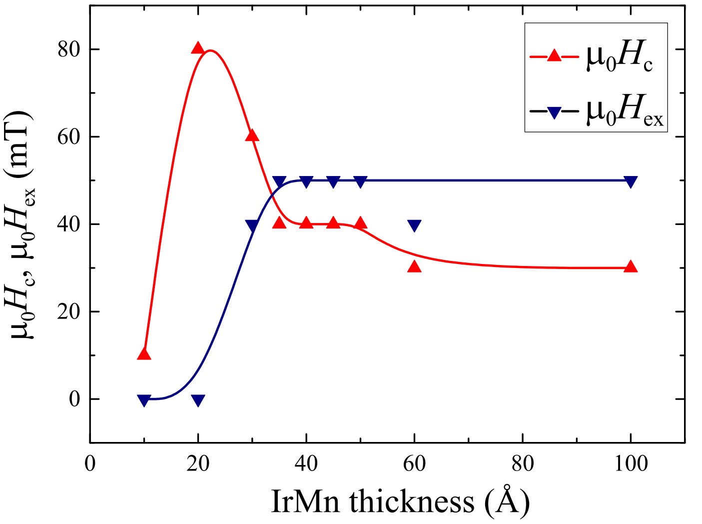

(b)

Figure 5.4: (a) Polar MOKE hysteresis loops for Ta(50 Å)/Pt(20 Å)/Co(10 Å)/IrMn(t_{IrMn})/Pt(50 Å); growth run 1. (b) Coercive field $\mu_0 H_c$ (red up triangles) and exchange bias field $\mu_0 H_{ex}$ (blue down triangles) as a function of IrMn layer thickness. The uncertainties are smaller than the size of the data points. The solid lines are guides to the eye.

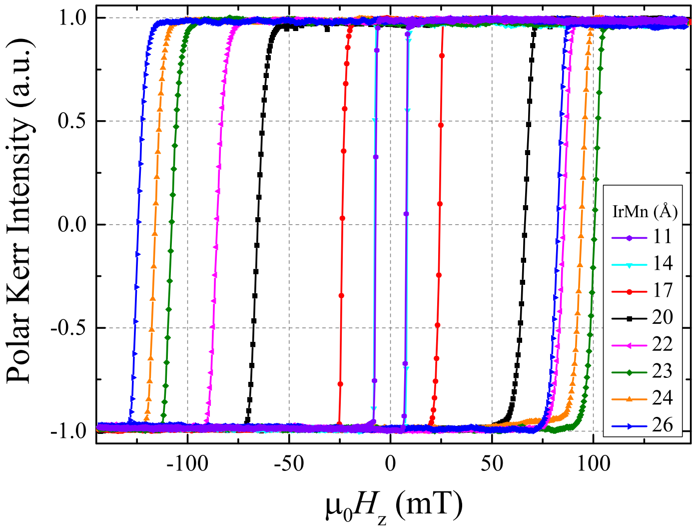

(a)

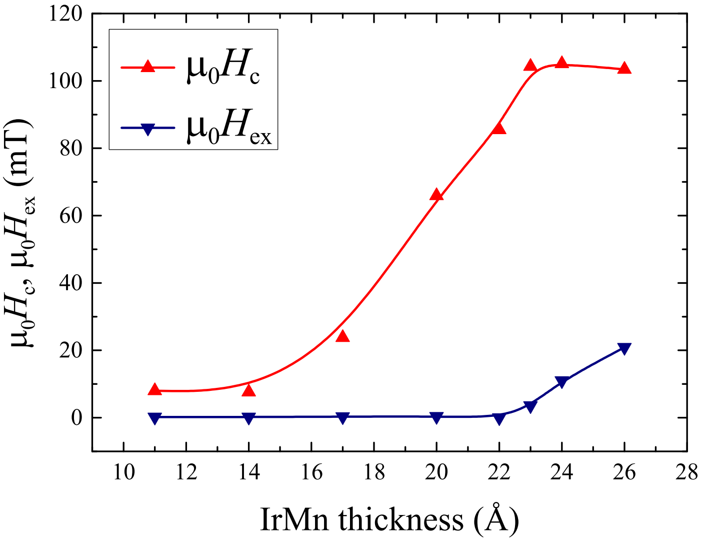

(b)

Figure 5.5: (a) Polar MOKE hysteresis loops for Ta(50 Å)/Pt(20 Å)/Co(10 Å)/IrMn(t_{IrMn})/Pt(50 Å); growth run 2. (b) Coercive field $\mu_0 H_c$ (red up triangles) and exchange bias field $\mu_0 H_{ex}$ (blue down triangles) as a function of IrMn layer thickness. The uncertainties are smaller than the size of the data points. The solid lines are guides to the eye.

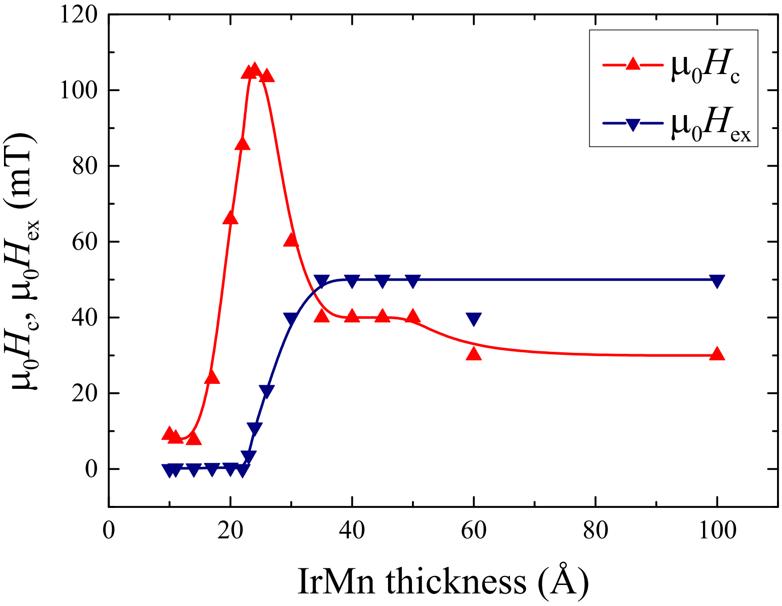

Figure 5.6: Coercive field $\mu_0 H_c$ (red up triangles) and exchange bias field $\mu_0 H_{ex}$ (blue down triangles) as a function of IrMn layer thickness, for Ta(50 Å)/Pt(20 Å)/Co(10 Å)/IrMn(t_{IrMn})/Pt(50 Å); growth run 1 and 2 combined. The solid lines are guides to the eye. The PM-AFM phase transition occurs at ≈17 Å, marked by the enhancement in coercivity. The exchange bias field develops at ≈23 Å, at which a peak in coercivity is also observed.

5.2.3 Additional assessments

Growth of control samples

Perpendicularly magnetised Pt/Co/Pt was grown as a control system in the same vacuum cycle and growth run. Pt/Co/Pt was chosen as it closely matches the system of Pt/Co/IrMn/Pt. Polar MOKE hysteresis loops and the magnetic properties of Pt/Co/Pt with varying Co thickness are summarised in Figure 5.7. The stacks exhibit PMA in the range of Co layer thicknesses which agree with literature [127, 36], including coercivity values. This indicates that the changes in the magnetic properties between Pt/Co/Pt and Pt/Co/IrMn/Pt are due to the IrMn layer and its coupling with the Co layer.

Comparison of capping layers

A capping layer of Pt was used for the stacks presented so far. In order to perform experiments using currents (not presented in this thesis), a capping layer with a higher resistivity than Pt was required to prevent shunting through the capping layer. For this, Ta was chosen due to its high resistivity of ≈180 $\mu\Omega$cm [122], compared to ≈30 $\mu\Omega$cm of Pt [148]. To investigate whether changing the cap to Ta effects the magnetic properties, similar stacks were grown and compared. The data for Pt/Co/IrMn with a Ta cap layer, presented in Figure 5.8 , shows that H_c, H_eb, and the required Co layer thickness for PMA, all remains the same for Pt and Ta capping layers.

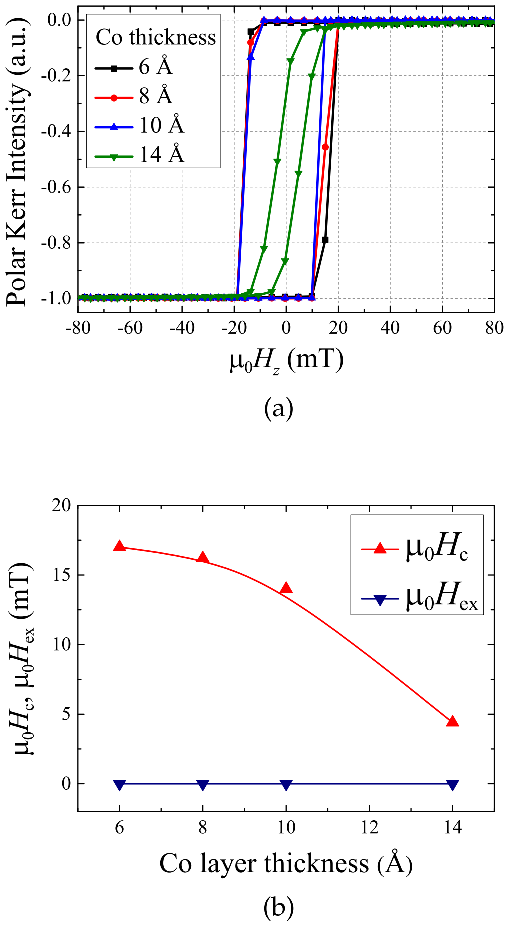

(a)

(b)

Figure 5.7: Control system of Pt/Co/Pt. (a) Polar MOKE loops. (b) Coercivity (red) and EB (blue) as a function of Co layer thickness.

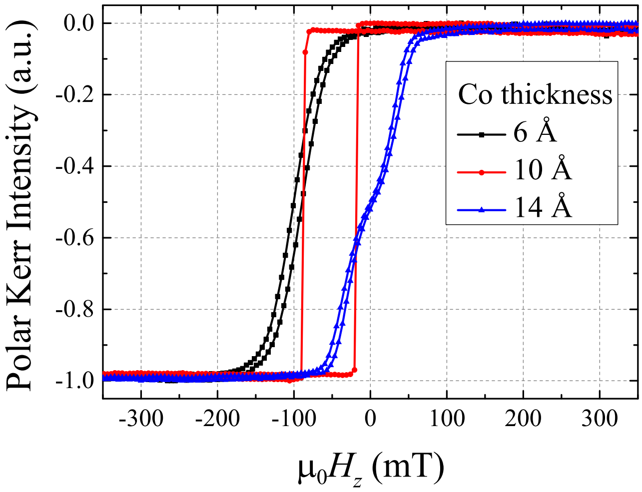

Figure 5.8: Polar MOKE hysteresis loops for Pt/Co/IrMn with a 50 Å Ta cap layer. PMA is achieved at 10 Å of Co, at which thickness, coercivity and EB are unchanged, when compared to the same stack but with a Pt cap layer.

Effect of annealing on magnetic properties

Annealing samples is often a required step in nanofabrication processes. Hence, experiments were performed to find out how post-growth high temperature annealing affects the magnetic properties of the samples. For this, a sample with EB was annealed at 200 °C for 2 hours in vacuum with a pressure of 2×10^{-4} Torr. Such a temperature is usually used during lithography processes. Polar MOKE loops before and after annealing are shown in Figure 5.9. Slight enhancement in both H_c and H_eb is observed, which is expected since more pinning sites are available because of crystallisation occurring due to annealing. However, a change in domain texture was not observed. More on domain structure will be discussed in the next chapter.

5.2.4 Investigation of paramagnetic behaviour

There are two critical temperatures associated with an AFM material: the Néel temperature T_N and the blocking temperature T_B. T_N is the temperature below which there exist AFM spin order. Above T_N there is no spin order, and the material is paramagnetic. T_B of an AFM material becomes

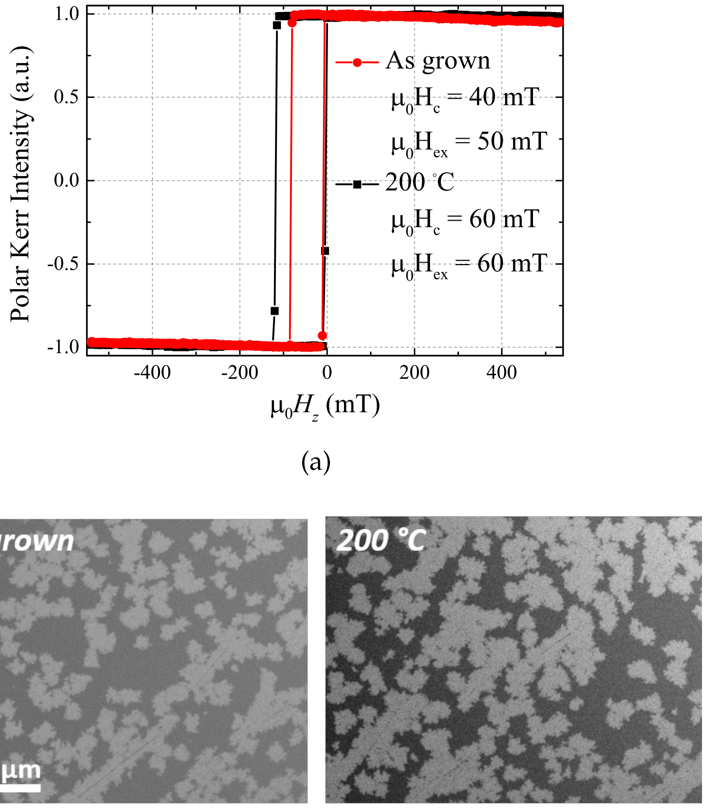

(a)

(b)

Figure 5.9: (a) Polar MOKE hysteresis loops for an exchange biased Pt/Co/IrMn sample before (red) and after (black) annealing. The sample was annealed at 200 °C for 2 hours in vacuum. (b) Kerr microscope difference images showing the magnetic domain morphology before (left) and after (right) annealing.

relevant when it is coupled to a FM material. T_B is the point below which the FM-AFM bilayer exhibits EB. As explained previously, this is when the spins of the AFM material at the interface are no longer reversible by the FM spins, and the uncompensated spins result in the EB. T_N (and consequently T_B) is related to the thickness of the AFM material [149, 150, 151]. The layer thickness influences properties, such as crystal structure and magnetic anisotropy energy of the material, and thus dictates the ordering temperature up to a given thickness after which the material attains bulk-like properties.

In order to verify the paramagnetic phase of the IrMn layer at low thicknesses, T_N and T_B of the IrMn layer were identified. This was done by measuring magnetic properties at low temperatures. The magnetic characterisation was performed in a 2-300 K VSM. The sample was initially cooled from room temperature to 5 K under a constant perpendicular field of 200 mT, which is large enough to saturate the Co layer magnetisation. After this procedure, a series of hysteresis loops were measured at increasing temperatures from which H_c and H_{ex} were extracted. At each point of temperature, repeated cycles of field sweep were performed in order to train the sample, and from the final loop the magnetic properties were extracted. The training effect [152, 153, 142] is the reduction in coercive and exchange fields with repeated field sweeps after the initial field-cooled state. This is due to the reorientation of the AFM domains with each field reversal, until a ground state is reached when the coercivity and EB stabilises. For our material system, four cycles of field sweep were sufficient to reach stable values of coercivity and EB.

The temperature dependence of H_c (red up triangles) and H_{ex} (blue down triangles) is depicted in Fig. 5.10 for three of the smaller thicknesses of IrMn (20, 14, and 11 Å) for the stack of Pt(20 Å)/Co(10 Å)/IrMn(t_{IrMn})/Pt(30 Å). H_{ex} of all the samples is observed to drop with temperature and vanish at T_B. At temperatures below this point, the AFM domains are stable and non-reversible. H_c also falls with temperature until T_N, at which point transition to the PM phase takes place and the value of H_c is that of the Co layer, as there is now no exchange coupling at the Co/IrMn interface. For the sample with 20 Å of IrMn, $T_B = 200$ K (marked with a dashed line in Fig. 5.10(a)), while T_N is just above room temperature. Thinning the IrMn layer, causes both T_B and T_N to move down the temperature axis, as shown in Fig. 5.10(b) and Fig. 5.10(c), for 14 and 11 Å of IrMn, respectively. At room temperature, these two samples are above T_N and thus, the IrMn layer is paramagnetic. This experiment demonstrates that at low thicknesses, the IrMn layer is in the paramagnetic phase and the transition to the AFM phase can be done by simply cooling under a field. These results also demonstrate that by controlling the IrMn thickness, T_B and T_N in this system can be modified.

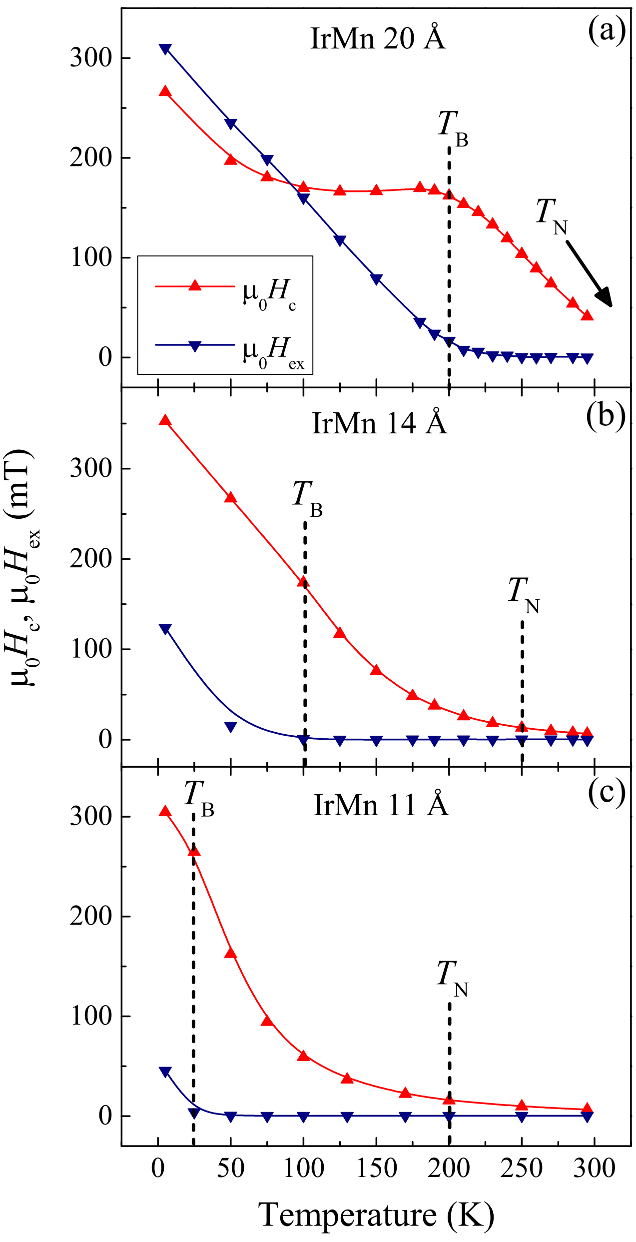

Figure 5.10: Plots of coercivity H_c (red up triangles) and exchange bias H_{ex} (blue down triangles) as a function of temperature, for selected IrMn thicknesses. The blocking (T_B) and Néel temperatures (T_N) are indicated by vertical dashed lines. At 20 Å IrMn (a) $T_B = 200$ K, while T_N lies just above room temperature. Both T_B and T_N move to lower temperatures as the IrMn layer thickness is decreased to 14 Å (b), and then to 11 Å (c).

5.3 Fabrication of Pt/Co/FeMn

Growth of the system of Pt/Co/$Fe_{50}Mn_{50}$ was performed under the same sputtering conditions as Pt/Co/IrMn, and on a Ta seed layer and with a Pt or Ta cap layer. As before, magnetic characterisation was performed using laser MOKE, and structural characterisation was performed using X-rays.

5.3.1 Optimisation of perpendicular magnetic anisotropy

For the initial growth run for the system of Pt(20 Å)/Co(10 Å)/FeMn(t_{IrMn}), the FM Co layer thickness (10 Å) was that used for the Pt/Co/IrMn system. However, this resulted in split hysteresis loops when the system is exchange biased. This is depicted in Figure 5.11 for 45 Å and 50 Å of FeMn layer thickness. The split occurs possibly because the spins of the Co layer align 50% up and 50% down. The FeMn layer grown on top of Co then follows this orientation.

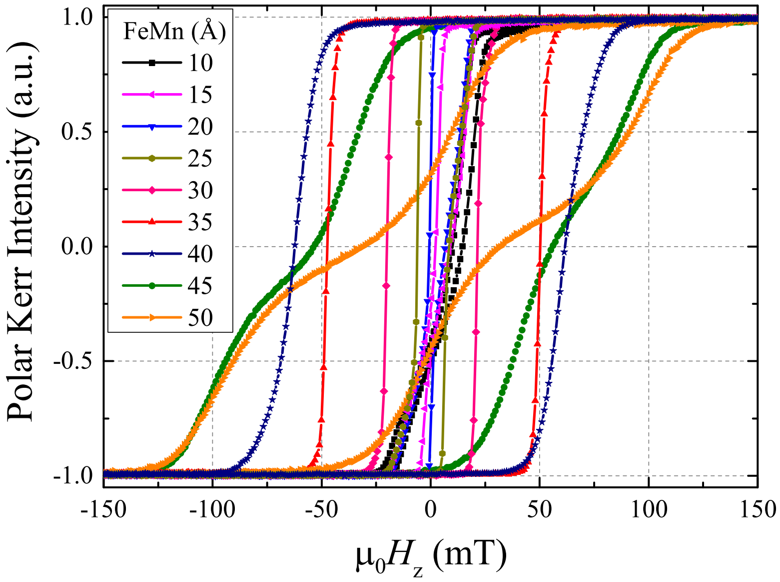

Figure 5.11: Split exchange biased polar MOKE hysteresis loops at 45 and 50 Å of FeMn. The data is for the system of Ta(50 Å)/Pt(20 Å)/Co(10 Å)/FeMn(t_{IrMn})/Pt(30 Å).

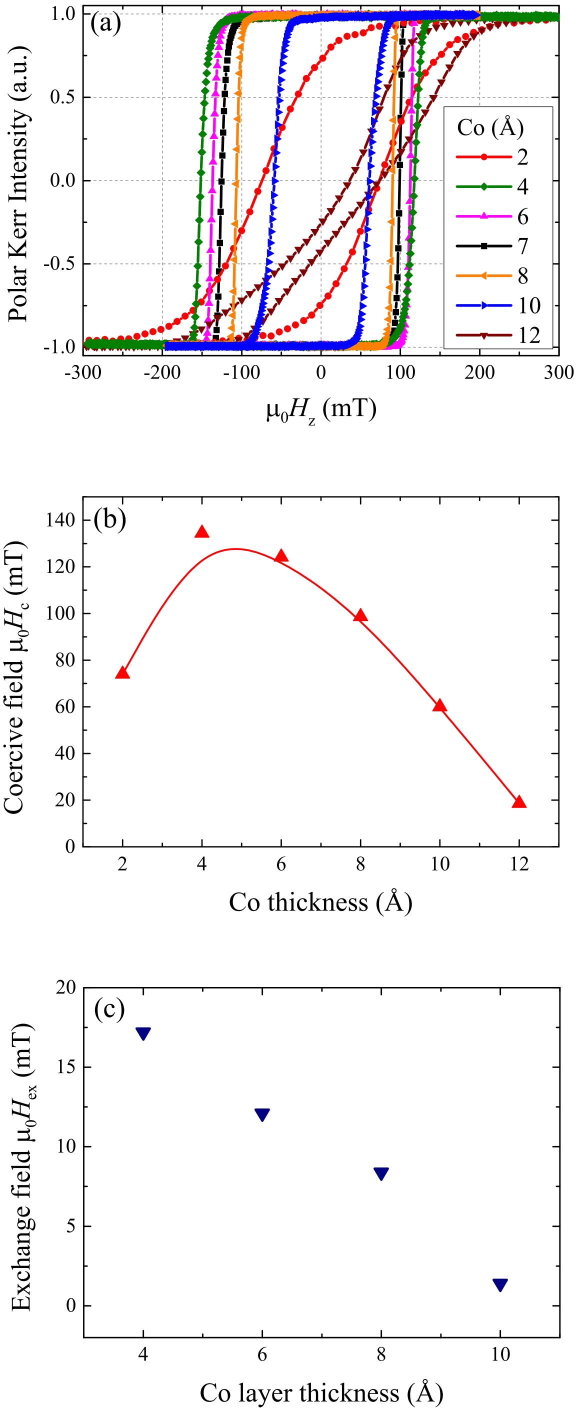

Figure 5.12: (a) Polar MOKE hysteresis loops for Ta(50 Å)/Pt(20 Å)/Co(t_{Co})/FeMn(40 Å)/Pt(30 Å). Films with Co thickness ranging from 4-10 Å exhibit PMA. (b) Coercive fields as a function of Co layer thickness. The solid line is a guide to the eye. (c) EB field as a function of Co layer thickness, for the samples with PMA.

Aligning the spins through a post-growth field cooling procedure should remove the splitting. However, to avoid a post-growth processing, and also, more importantly, to obtain a strong perpendicular anisotropy, the Co thickness was optimised also for this system. It was found that the necessary thickness of the Co layer for an optimum PMA for Pt/Co/FeMn was slightly thinner compared to the system of Pt/Co/IrMn. The growth and results for this experiment is shown in Figure 5.12, where the Co thickness was varied, while the other layers were at fixed thicknesses. The stack grown for this is Ta(50 Å)/Pt(20 Å)/Co(t_{Co})/FeMn(40 Å)/Pt(30 Å). Samples with Co thickness ranging from 4-10 Å exhibit perpendicular magnetisation characterised by square, easy axis loops. Thus, from this experiment, the ideal thickness for the growth of Pt/Co/FeMn was chosen to be t_{Co} = 6 Å. The EB decreases with increasing Co layer thickness, as shown in Figure 5.12 (c).

5.3.2 Antiferromagnetic layer thickness dependence

The optimised Co layer thickness of t_{Co} = 6 Å resulted in single loop hysteresis loops at different AFM FeMn layer thickness. In order to investigate in detail the dependence of coercivity and exchange bias on the FeMn layer thickness, three growth runs were performed, the data of which are shown in Figure 5.13, Figure 5.14, and Figure 5.15, respectively. The combined summary of the three growth runs is presented in Figure 5.16.

From the data in Figure 5.16 it is observed that in the system of Pt/Co/FeMn the onset of exhange bias occurs at ≈40 Å of FeMn, at which thickness a peak in coercivity is also observed. When the thickness of the FeMn layer is very small, it is paramagnetic, and the coercivity of the system is low. At ≈25 Å of thickness, PM to AFM phase transition occurs in the FeMn layer which initiates coupling with the Co layer causing an enhancement in coercivity. Both H_{ex} and H_{c} starts to stabilise at ≈80 Å of FeMn.

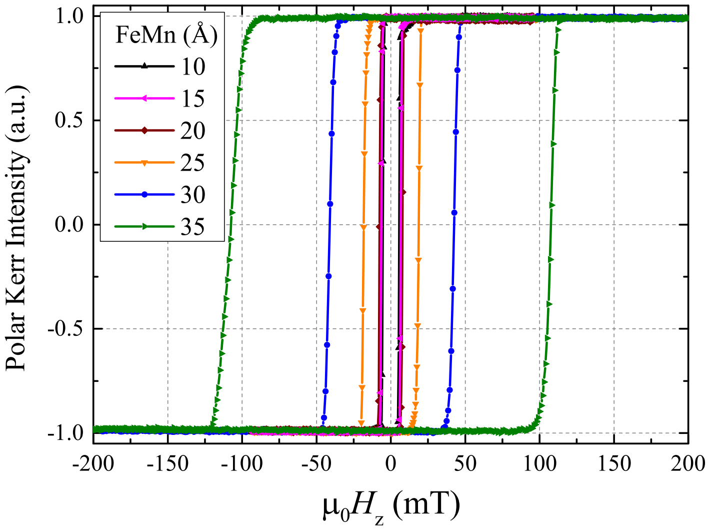

(a)

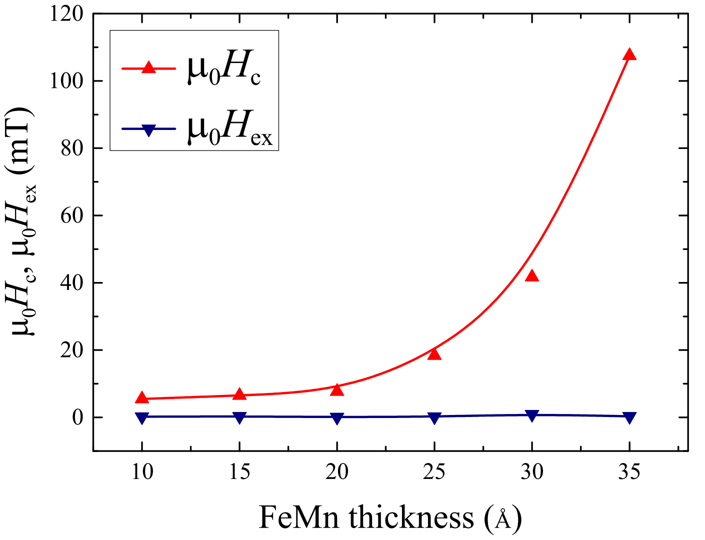

(b)

Figure 5.13: (a) Polar MOKE hysteresis loops for Ta(50 Å)/Pt(20 Å)/Co(6 Å)/FeMn(t_{FeMn})/Pt(30 Å); growth run 1. (b) Coercive field $\mu_0 H_c$ (red up triangles) and exchange bias field $\mu_0 H_{\mathrm{ex}}$ (blue down triangles) as a function of FeMn layer thickness. The solid lines are guides to the eye.

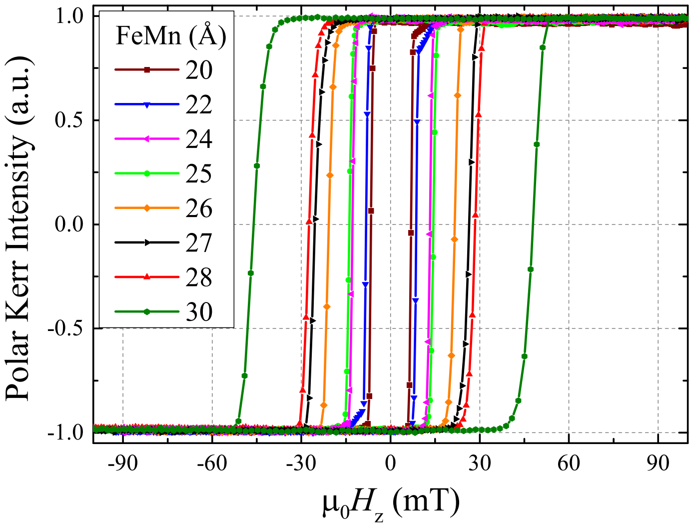

(a)

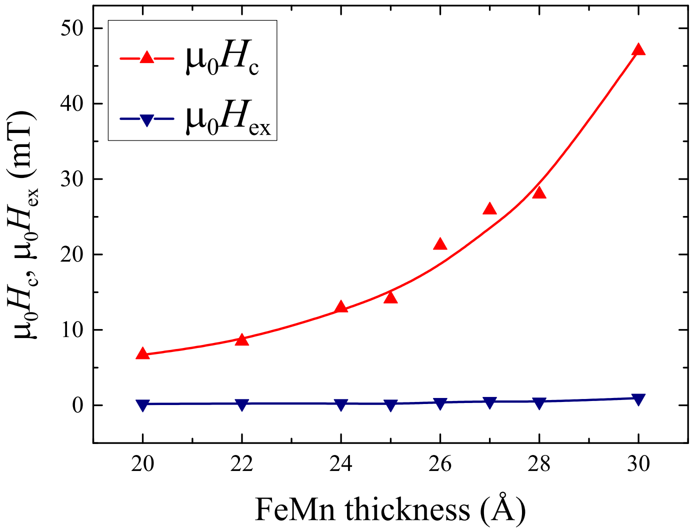

(b)

Figure 5.14: (a) Polar MOKE hysteresis loops for Ta(50 Å)/Pt(20 Å)/Co(6 Å)/FeMn(t_{FeMn})/Pt(30 Å); growth run 2. (b) Coercive field $\mu_0 H_c$ (red up triangles) and exchange bias field $\mu_0 H_{ex}$ (blue down triangles) as a function of FeMn layer thickness. The solid lines are guides to the eye.

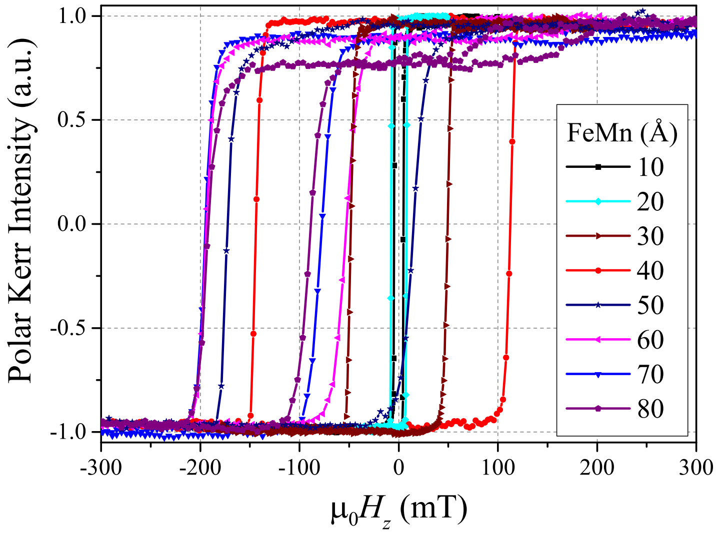

(a)

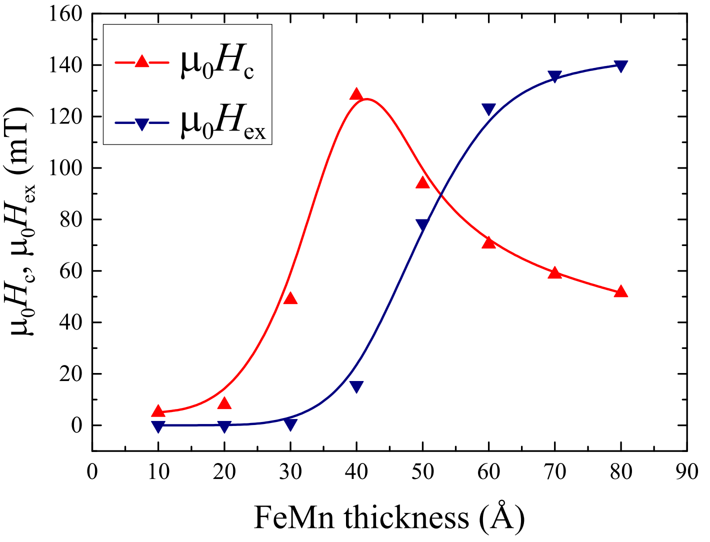

(b)

Figure 5.15: (a) Polar MOKE hysteresis loops for Ta(50 Å)/Pt(20 Å)/Co(6 Å)/FeMn(t_{FeMn})/Pt(30 Å); growth run 3. (b) Coercive field $\mu_0 H_\mathrm{c}$ (red up triangles) and exchange bias field $\mu_0 H_\mathrm{ex}$ (blue down triangles) as a function of FeMn layer thickness. The solid lines are guides to the eye.

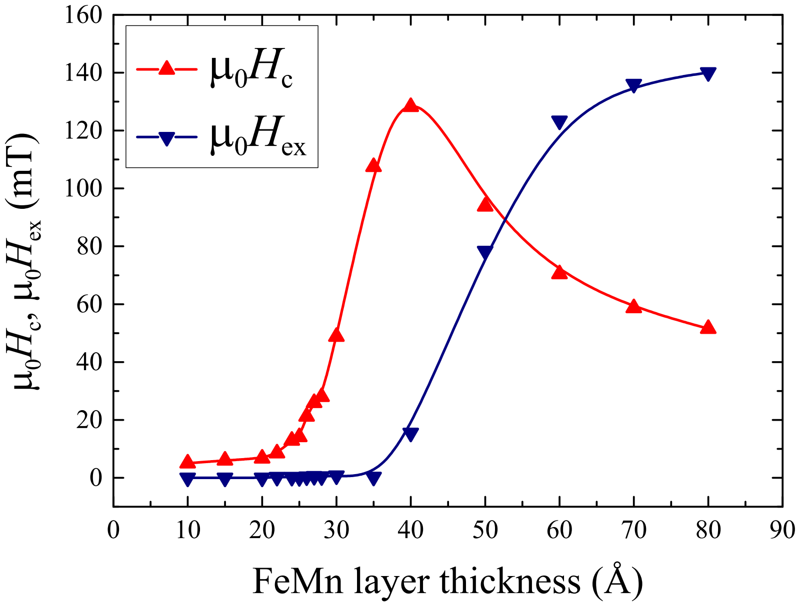

Figure 5.16: Coercive field $\mu_0 H_\mathrm{c}$ (red up triangles) and exchange bias field $\mu_0 H_\mathrm{ex}$ (blue down triangles) as a function of FeMn layer thickness, for Ta(50 Å)/Pt(20 Å)/Co(6 Å)/FeMn(t_FeMn)/Pt(30 Å); growth run 1, 2 and 3 combined. The solid lines are guides to the eye. The exchange bias field develops at ≈40 Å, at which a peak in coercivity is also observed.

5.4 Comparison between the two systems

The general trend of the magnetic properties in the two systems of Pt/Co/IrMn and Pt/Co/FeMn as a function of AFM layer thickness is very similar. However, there are notable differences as well. The AFM phase transition, which we relate to the enhancement of coercivity, occurs at a smaller thickness for the IrMn layer (≈17 Å), compared to the FeMn layer (≈25 Å). Consequently, the onset of EB, along with the peak in coercivity, occurs for a thinner IrMn layer (≈23 Å), compared to FeMn (≈40 Å). Furthermore, the peak coercivity of the IrMn system is smaller (≈110 mT) compared to the FeMn system (≈130 mT). The maximum EB field for the IrMn stack is almost a factor of 3 smaller (≈50 mT) compared to the FeMn stack (≈140 mT). Although, a thinner Co layer in the FeMn system may have contributed to this behaviour in both coercivity and EB. Lastly, the effective anisotropy field is larger for the IrMn system (anisotropy field measurements are shown in Chapter 6).

5.5 Summary

In this chapter, the fabrication methods and subsequent characterisation of polycrystalline systems of Pt/Co/IrMn and Pt/Co/FeMn were outlined. The two systems investigated exhibit perpendicular magnetic anisotropy and perpendicular exchange bias. The systems were grown by magnetron sputtering. Structural characterisation were done using X-ray reflectivity and diffraction, while magnetic properties were characterised by MOKE magnetometry, vibrating sample magnetometry, and magneto-optical imaging. The relation between the structural and the magnetic properties was established, especially, the dependence of coercivity and EB on the AFM layer thickness (IrMn and FeMn layers). Optimisation of the FM Co layer was also performed to obtain an optimum PMA.

Through this investigation, different phases of the AFM layers were classified depending on their thicknesses. Particularly, the points of PM to AFM phase transition, and the onset of EB were distinguished. Furthermore, the Néel temperatures and the blocking temperatures at different IrMn layer thicknesses were identified by temperature dependent magnetometry.

Lastly, the two systems were compared in terms of their magnetic and structural properties. Overall, the information extracted from this investigation will be used to explain the interfacial mechanisms in these systems, which is the focus of the next chapter.

Chapter 6

Antiferromagnetic spin order and the Dzyaloshinskii-Moriya interaction

6.1 Introduction

Antiferromagnets exhibit the second basic type of magnetic order, which we can exploit to venture into new avenues in spintronics. This chapter investigates interfacial mechanisms in perpendicularly magnetised exchange biased systems of Pt/Co/IrMn and Pt/Co/FeMn. The transition from paramagnetic to antiferromagnetic order in the IrMn and FeMn layers is attained by varying the thicknesses. This chapter builds on the development work in Chapter 5, where it was shown that there is a (temperature-dependent) critical thickness below which antiferromagnetic order does not establish itself. In these multilayers, the aim is to promote and stabilise chiral spin states, such as homochiral Néel walls [154, 30, 41, 36, 43] and skyrmions [45, 38, 155, 36], through the Dzyaloshinskii-Moriya interaction. The efficiency of current-driven DW motion [34, 33, 121] can be increased by setting up a Néel configuration for DWs, while a vertical exchange field could help stabilise skyrmion bubbles.

The magnetic domain morphology of the ferromagnetic Co layer was investigated in these systems by magneto-optical imaging. It was demonstrated that the domain texture is influenced by the spin order of the AFM layers. This dependence is directly linked to the FM-AFM inter-layer exchange coupling and the anisotropy energy of the AFM layer.

The interfacial Dzyaloshinskii-Moriya interaction was also probed in these systems by both, Brillouin light scattering spectroscopy and the field-driven domain expansion technique. The measurements show that the DMI remains unchanged, within experimental uncertainty, for different phases of the AFM layers. From this observation it was concluded that the DMI is insensitive to both AFM spin order and exchange bias. The experimental results aligns with the current theoretical model of the interfacial DMI.

Resolving elementary mechanisms such as these is vital for the development of prospective spintronic devices engaging chiral magnetic configurations in FM-AFM heterostructures.

6.2 Domain morphology

In Chapter 5, it was demonstrated how the AFM layer thickness dictated its spin order and directly influenced the magnetic properties, such as the onset of EB, and the enhancement in coercivity, in multilayered systems incorporating AFM layers. Similarly, the AFM layer thickness profoundly affects the magnetic domain morphology, by influencing the anisotropy energy, and consequently the FM-AFM inter-layer coupling. Figure 6.1 shows the variation in domain structure as the IrMn layer thickness is varied. The variation can be directly correlated with thickness dependent magnetic properties of Figure 5.6. The domains were imaged with a Kerr microscope in the polar mode in order to sense out-of-plane magnetisation. Difference images were produced by subtracting images before and after the application of an OOP field. The fields applied closely correlate to the coercive fields. In some cases, the field values are close to the nucleation field, such as Figure 6.1(e). However, in other cases, they are slightly different than the nucleation field, such as in Figure 6.1(a), where the domain was allowed to expand.

At small thicknesses, the IrMn layer is in the paramagnetic phase lacking any spin order. This was investigated in Section 5.2.4, where at room temperature Pt/Co/IrMn stacks with 11 and 14 Å thin IrMn layers were found to be above the Néel temperature. In such a scenario, the domains are found to be large and threaded with disconnected networks of unreversed narrow domains. This is depicted in Figure 6.1(a) and (b), for 11 and 14 Å of IrMn, repectively. These narrow domains form as a propagating DW gets pinned at a defect site and prefers to bend around it, since it is energetically favourable, compared to flipping over the pinning site. These domains continue to exist since they are bounded by domain walls with the same chirality, which is stabilised by the DMI, and require large fields to be annihilated due to the presence of a large energy barrier [43]. These domains continue to grow as the DWs bounding them grow longer in length by regularly finding a pinning site. This results in the creation of new branches, or deviations from a linear path.

At ≈17 Å of IrMn, PM to AFM phase transition occurs, which is marked by the enhancement of coercivity in Figure 5.6. As a result of the AFM ordering, coupling is initiated at the FM/AFM interface and the domain morphology changes significantly, as shown in Figure 6.1(c). Now we observe the nucleation of isolated bubble domains with relatively smooth DWs, and do not observe the narrow domain networks. This is because the DWs are no longer getting pinned at defect sites due to the application of relatively larger fields to nucleate domains and propagate DWs, owing to the increased coercivity of the sample resulting from the FM/AFM coupling. In fact, as the IrMn layer thickness is increased further, the enhancement in coercivity continues, which results in a significant increase in the density of nucleation as even larger fields are now necessary to nucleate domains. This is observed in Figure 6.1(d-e).

At the critical thickness of ≈23 Å, the exchange bias starts to develop in the system, as shown in Figure 5.6, which brings about another change in the domain profile. At this point, the DWs start to become rough (Fig. 6.1(e-f)) due to increased pinning as AFM domains start to stabilise, which complicates the spin structure and increases disorder. Eventually, the DWs become even rougher as the EB becomes large and stable at thicker IrMn layer, as the anisotropy energy of the AFM layer becomes robust. This can be noticed in Figure 6.1(g-h).

The system of Pt/Co/FeMn has a similar dependence of its domain configuration as a function of the AFM layer FeMn. The changes in the domain morphology is presented in Figure 6.2, while the magnetic properties are summarised in Figure 5.16. At ≈15 Å of thickness, the FeMn layer is in the PM phase and the samples exhibit large domains (Figure 6.2(a)) with networks of narrow domains, similar to the IrMn system. The PM to AFM phase transition occurs at ≈25 Å of FeMn causing an enhancement in coercivity due to FM/AFM inter-layer exchange coupling. This results in the formation of bubble domains with smooth DWs, and without the network features, as shown in Figure 6.2(b). Further increasing the FeMn layer causes the coercivity to rise even more resulting in a substantial increase in nucleation density (Fig. 6.2(c-d)). For thicker FeMn layers, when the EB is large, the domains are too small to be resolved by the Kerr microscope. It would be interesting to investigate the presence of skyrmion bubbles at such thicknesses, using a higher resolution imaging technique.

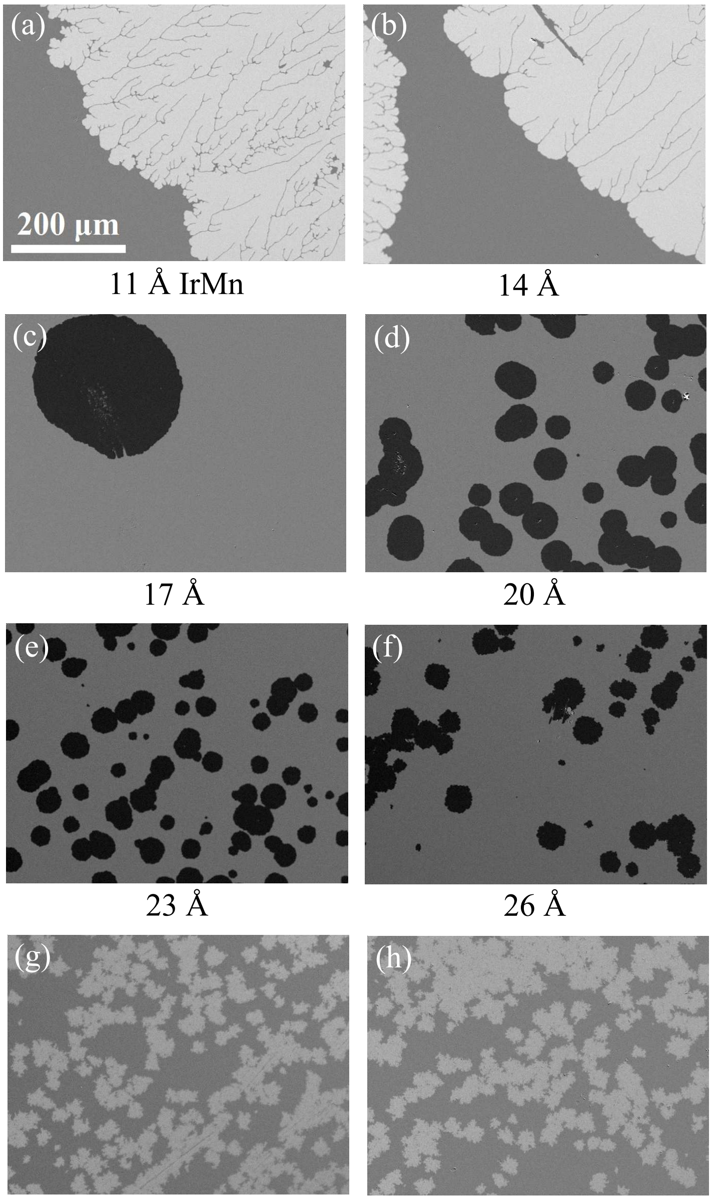

11 Å IrMn 14 Å

17 Å 20 Å

23 Å 26 Å

45 Å 50 Å

Figure 6.1: Kerr microscope difference images showing the propagation of magnetic domains by an out-of-plane field. The field pulses were applied for a few seconds, and ranged from 5-100 mT depending on the coercivity of the sample. In these images the bright/dark regions (relative to grey) represent the areas swept out by DWs during the field pulse. The domain morphology changes significantly as a function of IrMn layer thickness.

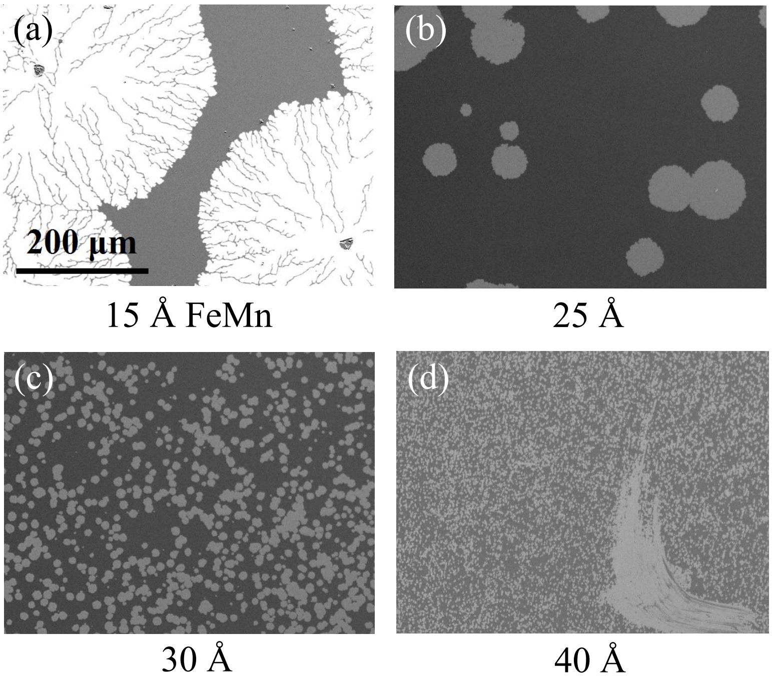

Figure 6.2: Kerr microscope difference images showing the changes in domain structure as a function of FeMn layer thickness.

Thus, in these systems the domain morphology is dependent on the FM-AFM inter-layer exchange coupling, which is in turn dependent on the spin order of the AFM layer. In the next sections, we investigate whether the Dzyaloshinskii-Moriya interaction has a similar dependence on the AFM spin order.

6.3 Determining the Dzyaloshinskii-Moriya interaction

The Dzyaloshinskii-Moriya interaction was measured primarily by Brillouin light scattering (BLS) spectroscopy, and also by the domain expansion method. However, only one sample exhibits domains suitable for the field-driven technique. Thus we discuss these measurements first, and then move on to BLS. We also review the differences between the two techniques in this section.

6.3.1 Field-driven domain expansion technique

The method of quantifying the DMI from the field-driven asymmetric expansion of magnetic domains has been elaborated in Chapter 4. This method relies on the nucleation, and subsequent propagation of bubble domains. Measuring the exchange biased samples using this method, difficulties were faced mainly on three fronts. Firstly, a high nucleation density in most samples offered a problem to find isolated bubble domains, and thus, not enough room for expansion to obtain a reliable value of the DW propagation velocity. Secondly, enhanced interfacial pinning in samples with a large EB caused small sections of a propagating DW to align at an angle, rather than perpendicularly, with respect to the applied IP field. This means that the DMI field, which acts on a DW locally, will not be aligned with the IP field, and thus the IP field at the minimum velocity might not be a true measure of the DMI field. This problem, however, is largely superseded by the first issue of dense nucleation. Thirdly and lastly, the coercivities of most of the films were relatively high and were around the limiting range of the custom home built coil that is used to generate the OOP field in this setup. This caused the magnet to heat up significantly, especially during repeated bubble expansions, heating up the sample and resulting in inconsistent DW velocities.

In spite of these obstacles, one sample where the IrMn layer is 17 Å thick was measured. In this sample, isolated bubble domains could be nucleated with enough room for propagation. Also, the coercivity was relatively low, so as to not heat up the coil. The bubble expansion experimental data, along with the fit, is shown in Figure 6.3. The DMI field obtained is 42 ± 3 mT, corresponding to a DMI constant of $D = -0.33 \pm 0.03\ \mathrm{mJ/m^2}$. The DWs in these systems have left-handed chirality. The OOP field used to drive the DWs was 18 mT, which is well within the creep field range for this sample. This was validated from the linear dependence of the natural logarithm of the DW velocity ($\ln v$) on $H_z^{-1/4}$. A plot of this is shown in Figure 6.4.

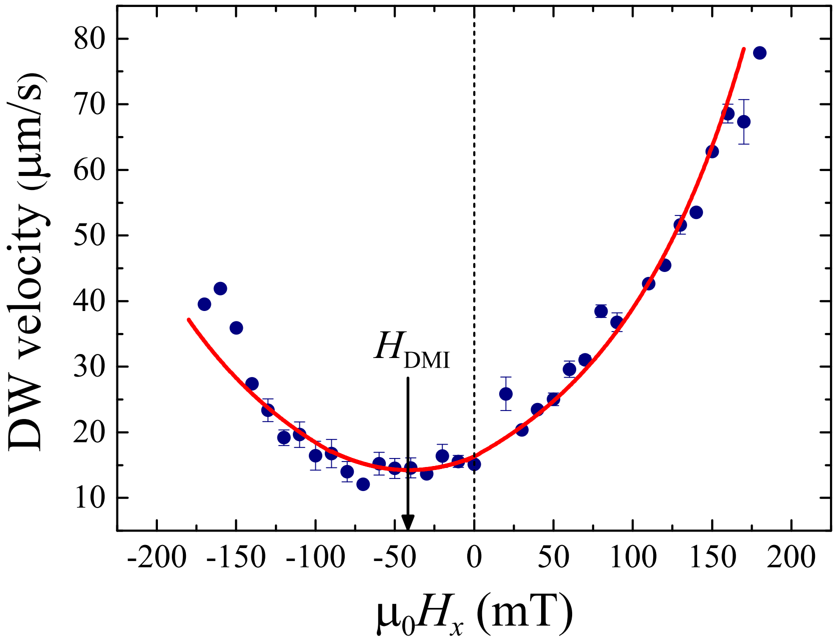

Figure 6.3: DW velocity as a function of IP field H_x from bubble expansion data for a sample of Pt(20 Å)/Co(10 Å)/IrMn(17 Å). The OOP field used to expand the domains was 18 mT. The error bars are from standard deviations of the average values. The solid lines are fits of the creep law (Equation 4.1). The minimum velocity point of the plot marks the DMI field H_DMI indicated by the black arrow.

Compared to Ta (in Chapter 4), the Pt underlayer generates a DMI which is opposite in sign and also much larger in magnitude. According to Ma *et al.* [156], the sign of the DMI is related to the 5*d* electron occupancy. The 5*d* bands of Ta are less than half filled, while those of Pt are more than half filled. This difference in band filling leads to opposite signs in the expectation value of spin-orbit coupling which results in the DMI to be opposite. The increase in magnitude of the DMI from Ta to Pt is due to the position of the Fermi level [156]. The increase in electron number (Ta $5d^3$ to Pt $5d^9$) moves the Fermi level towards the 5*d* states which have a dominant contribution to the DMI, resulting in an increase in the DMI strength.

To measure the DMI for all the other samples with different AFM thicknesses, BLS was used, and is explained in the next section.

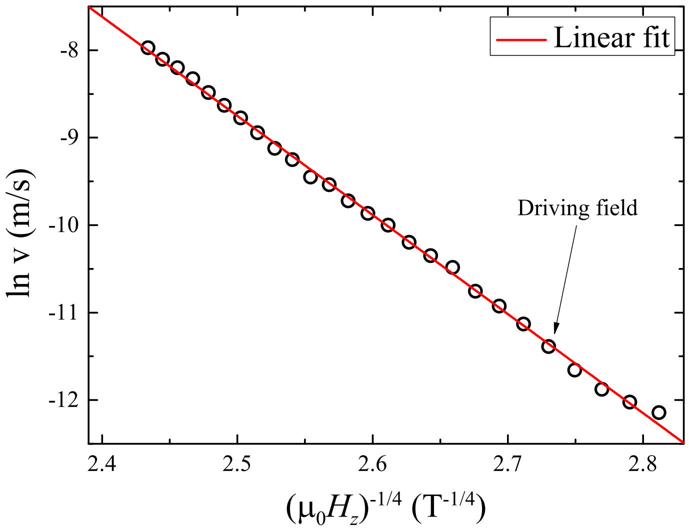

Figure 6.4: Plot of $\ln v$ vs $H_z^{-1/4}$. Linear behaviour (red solid line) confirms DW creep motion. The driving field for the DMI measurements was 18 mT, which is well within the creep regime. The uncertainty is smaller than the size of the data points.

6.3.2 Brillouin light scattering spectroscopy

The Brilloiun light scattering (BLS) spectroscopy measurements were performed by H. T. Nembach and J. M. Shaw at the National Institute of Standards and Technology, USA [157].

BLS is the inelastic scattering of a monochromatic light (from a laser) by excitations, such as phonons, magnons, etc. Through this method, the dispersion relation of these excitations are obtained by recording the excitation frequencies as a function of the scattering wavevector. The excitations occur in the GHz frequency regime, which is about four orders of magnitude smaller compared to the frequency of the probing light. Thus, to achieve high resolution, Fabry-Pérot interferometers are used.

To probe the DMI by BLS, we utilise the non-reciprocity of the DMI induced frequency shift and measure the spin wave frequencies for opposite magnetisation [63, 59, 60]. This means that since the energy contribution by the DMI is antisymmetric, spin waves with the same wavevector but propagating in opposite directions have different frequencies. The spin waves are probed in the Damon-Eshbach geometry, where the magnetisation of the film is saturated in-plane by an applied magnetic film and the spin waves undergo non-reciprocal propagation in the direction perpendicular to the magnetisation. The frequency shift is then given by

$$\Delta f = \left|\frac{g\mu_\mathrm{B}}{h}\right| \frac{2D_\mathrm{eff}}{M_\mathrm{s}}k = \left|\frac{g\mu_\mathrm{B}}{h}\right| \frac{2D_\mathrm{s}}{M_\mathrm{s}t_\mathrm{FM}}k, \tag{6.1}$$

where D_eff is the volumetric DMI constant, g is the spectroscopic g-factor taken to be 2.14 [158] for perpendicularly magnetised films, M_s is the saturation magnetisation, k is the magnitude of the wavevector of the spin waves, μ_B is the Bohr magneton, and h is Planck's constant. In the last equality, D_s is the interfacial DMI parameter which represents the DMI contribution from the top and bottom interfaces ($D_\mathrm{s} = D_\mathrm{eff}t_\mathrm{FM}$, where t_FM is the FM layer thickness). Thus, D_s should be independent of the FM layer thickness, if we consider the DMI to be a truly interfacial effect. The sign of the frequency shift depends on the direction of the magnetisation and the propagation direction of the spin waves. Figure 6.5 shows representative BLS spectra, for a sample of Pt(20 Å)/Co(10 Å)/IrMn(24 Å), where shifts in Stokes (negative frequencies) and anti-Stokes (positive frequencies) peaks can be observed, corresponding to $\Delta f = 0.90 \pm 0.05$ GHz resulting in an effective DMI of $D_\mathrm{eff} = -1.22 \pm 0.08$ mJ/m^2.

The saturation magnetisation M_s is measured by a SQUID-VSM. For each system, M_s was measured for multiple samples with different AFM layer thickness, but with the same Co layer thickness. From these an average value was determined with an uncertainty from the standard error of the average value. A representative SQUID-VSM moment vs IP field hysteresis loop is shown in Figure 6.6(a) for a sample of Pt(20 Å)/Co(10 Å)/IrMn(11 Å). M_s was then determined by normalising the saturation moment by the volume of the FM layer. Figure 6.6(b) is a plot of M_s of different samples with varying IrMn layer thickness. Figure 6.7 presents the same for the system of Pt/Co/FeMn.

For Pt/Co/IrMn, $M_\mathrm{s} = (1.36 \pm 0.05) \times 10^6$ A/m, which is similar to bulk Co value of 1.45×10^6 A/m. However, a high value for Pt/Co/FeMn of

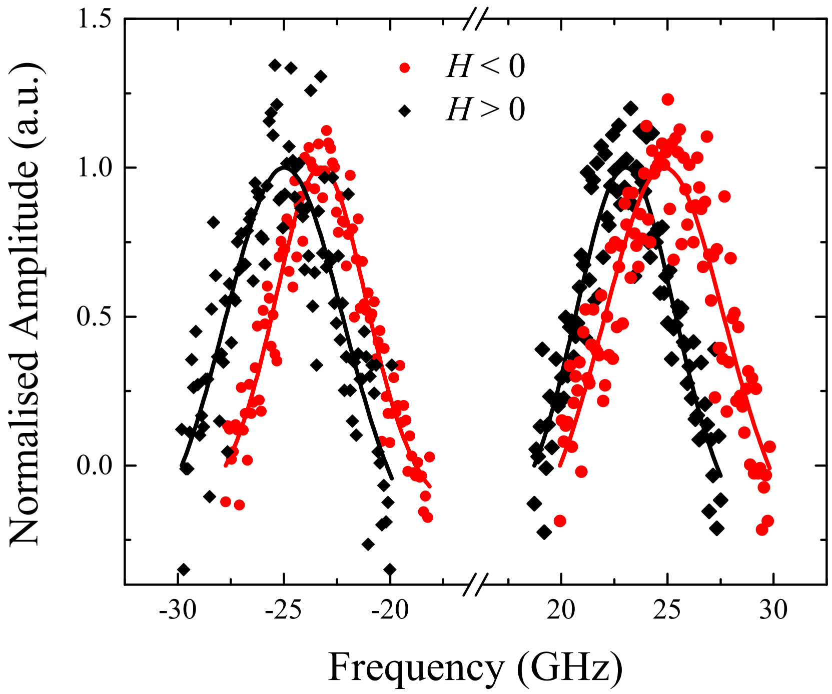

Figure 6.5: Normalised BLS spectra for a sample of Pt(20 Å)/Co(10 Å)/IrMn(24 Å) with perpendicular magnetic anisotropy. The solid lines are fits of the data using the Lorentzian transmission function of the tandem multi-pass interferometer in the BLS spectrometer

$M_s = (2.33 \pm 0.05) \times 10^6$ A/m was found. This discrepancy is possibly due to the formation of a monolayer of Fe at the Co/FeMn interface, reported by Antel *et al.* [159], which contributes to the total moment. Thus, the effective volume of the FM layer is increased by including a monolayer of Fe in order to account for this inconsistency, and this gives a value of $M_s = (1.57 \pm 0.04) \times 10^6$ A/m.

6.3.3 Discrepancy between the techniques

Although a qualitative agreement could be found between the DMI obtained from the two methods, we do observe a numerical inconsistency ($D_{\text{creep}} = -0.33 \pm 0.03$ mJ/m^2 and $D_{\text{BLS}} = -1.14 \pm 0.05$ mJ/m^2). Such divergence in DMI values between the two techniques is reported in a few

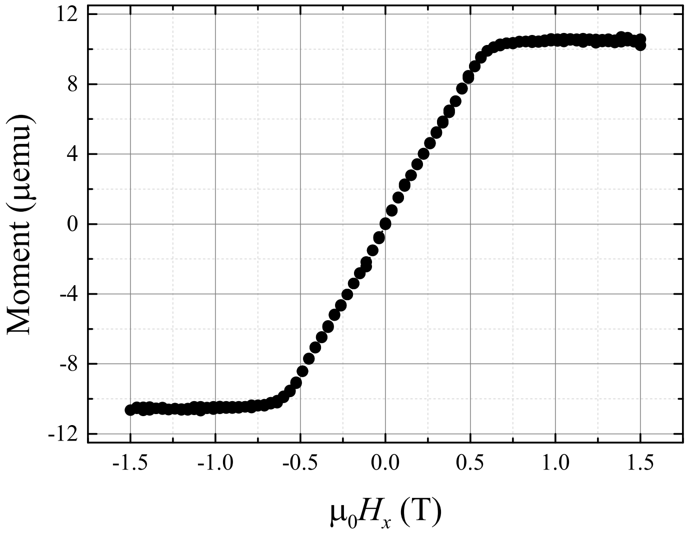

(a)

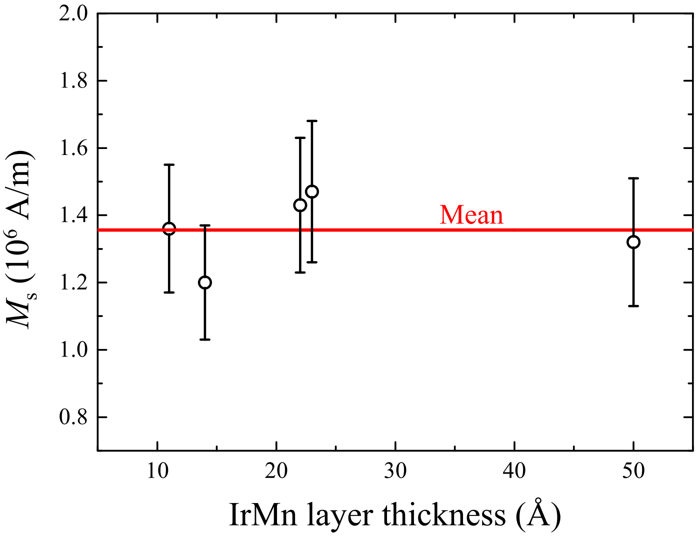

(b)

Figure 6.6: (a) SQUID-VSM moment vs IP field hysteresis loop of a perpendicularly magnetised Pt(20 Å)/Co(10 Å)/IrMn(11 Å) sample from which the saturation magnetisation M_s is obtained. (b) M_s of samples at different IrMn layer thickness; other layer thicknesses are the same as in (a). From these a mean value (red line) of $M_\mathrm{s} = (1.36 \pm 0.05) \times 10^6$ A/m is calculated. The dominant contribution to the error bars is the uncertainty in FM thickness, while the uncertainty in the mean value is from the standard error.

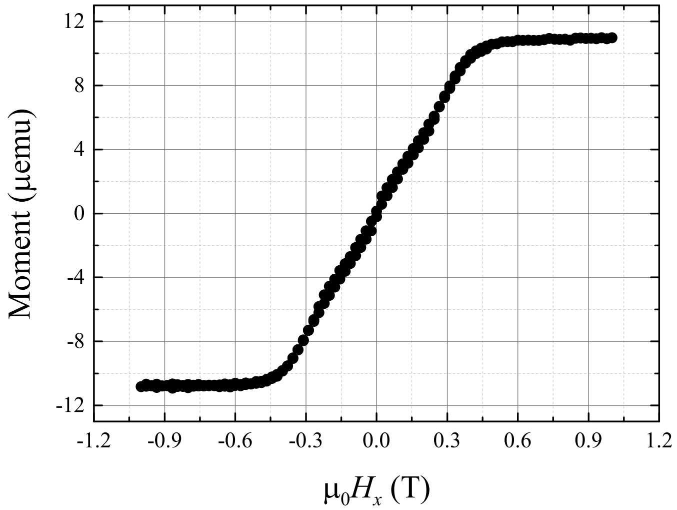

(a)

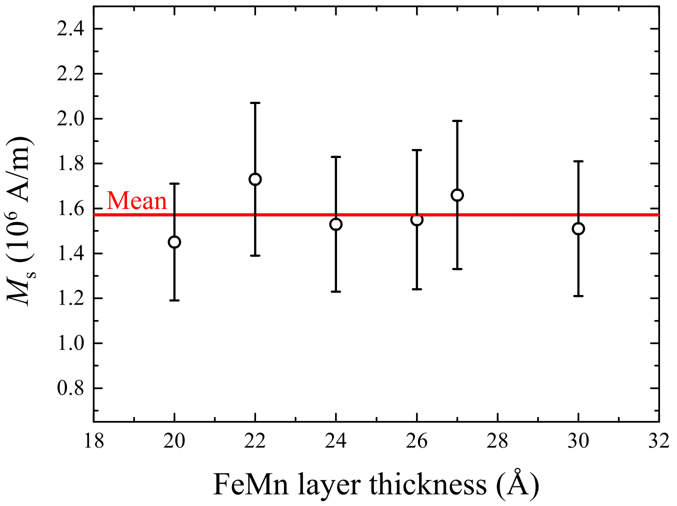

(b)

Figure 6.7: (a) SQUID-VSM moment vs IP field hysteresis loop of a perpendicularly magnetised Pt(20 Å)/Co(6 Å)/FeMn(24 Å) sample from which the saturation magnetisation M_s is obtained. In this case, an additional contribution of a monolayer of Fe to the volume of the FM layer was considered when calculating M_s. (b) M_s of samples at different FeMn layer thickness; other layer thicknesses are the same as in (a). From these a mean value (red line) of $M_s = (1.57 \pm 0.04) \times 10^6$ A/m is calculated. The dominant contribution to the error bars is the uncertainty in FM thickness, while the uncertainty in the mean value is from the standard error.

works [65, 64, 54], which also suggest plausible interpretations to this discrepancy. One possible explanation is that the modelling of DW propagation in the creep regime is more focused on the motion of DWs across pinning sites and neglects magnetisation dynamics, such as damping. Indeed it has been shown [64] that in strongly damped systems, the DMI values from the two methods show better agreement. Furthermore, creep motion involves thermally activated propagation from pinning sites which largely consist of physical regions such as grain boundaries, interfacial roughness, and defects, where the DMI could be locally reduced. Thus, the evaluation of the DMI from DW creep experiments will naturally lead to low values of DMI. Evaluation of the DMI from DW flow regime experiments [125, 54] tend to agree closely with BLS. Another potential explanation is that the measurement length scales are quite different in the two techniques [64]. In BLS, the DMI is probed over areas of 100 µm (typical beam of a laser) and involves spin waves of a few 100 nm. Thus, the DMI probed averages out over such distances. On the other hand, domain wall creep is concerned with length scales of 10s of nm, which is typical of the separation distance between pinning sites. Overall, the two processes are intrinsically very different and thus would require improved modelling to address the inconsistencies between them while evaluating the DMI.

6.4 Dependence of the DMI on spin order

To understand the effect of the AFM spin order on the DMI, the DMI of the Pt/Co/IrMn system was measured at four critical thicknesses of the antiferromagnetic IrMn layer. The measurements are summarised in Table 6.1 and graphically represented in Figure 6.8. The different thicknesses correspond to the different points when the system exhibits distinct magnetic properties which are strongly related to the AFM spin order. Sample (a) is when the IrMn layer is in its PM phase with no spin order, and thus no coupling at the Co/IrMn interface. Sample (b) is at the point of PM to AFM phase transition of the IrMn layer. Coupling is initiated at this point, however, there is no EB in the system yet. Sample (c) is at peak coercivity of the system, that is, when the EB starts to set in. Lastly, sample (d) is when there is a large EB in the system, brought about by a larger anisotropy energy of the AFM layer as being thicker.

Table 6.1: Comparison of the DMI at different phases of the AFM layers of the two investigated exchange coupled systems. The numbers in parentheses represent the nominal layer thickness in Å. The dominant contribution to the uncertainty in D_{eff} is the uncertainty in M_{s}, while for D_{s} there is also a contribution from the uncertainty in FM layer thickness, leading to a larger experimental error. For the FeMn system, the contribution of a monolayer of Fe to the volume of the FM layer and the M_{s} was taken into account when calculating D_{s}. Normally, experimental uncertainties should be rounded to one significant figure. However here, retaining two figures may be better, since rounding up to one figure would mean a substantial proportionate change in the uncertainty, as the leading digit is a 1 [160].

Sample	Spin order	EB	D_{eff} (mJ/m^2)	D_{s} (pJ/m)
(a) Pt(20)/Co(10)/IrMn(11)	PM	No	-1.14 ± 0.05	-1.14 ± 0.13
(b) Pt(20)/Co(10)/IrMn(17)	AFM	No	-1.14 ± 0.05	-1.14 ± 0.12
(c) Pt(20)/Co(10)/IrMn(24)	AFM	Yes	-1.22 ± 0.08	-1.22 ± 0.15
(d) Pt(20)/Co(10)/IrMn(50)	AFM	Yes	-1.11 ± 0.12	-1.11 ± 0.16
(e) Pt(20)/Co(6)/FeMn(10)	PM	No	-1.50 ± 0.08	-1.35 ± 0.17
(f) Pt(20)/Co(6)/FeMn(26)	AFM	No	-1.44 ± 0.08	-1.30 ± 0.16

From the experiments, we find that the magnitude of the DMI remains largely unchanged in all four cases from which it can be inferred that neither the AFM spin order nor the EB influences the mechanism of the DMI in this system. We also observe that the DMI does not change for the FeMn system. The DMI was measured when the FeMn layer was paramagnetic (sample (e)) and when it was antiferromagnetic (sample (f)). However, it was not possible to measure the DMI in this system with a large EB. This is because the Co layer in this system is very thin, and thus a thick FeMn layer on top of this very thin Co layer reduces the intensity of the scattered signal. Both the systems possess left-handed chirality.

The non-dependence of the DMI on the AFM spin order can be explained if we consider the three-site DMI model of Fert and Levy [7]. According to this model, the DMI is generated at a non-magnetic/FM interface, when an atom from the non-magnetic layer, due to the spin-orbit coupling (SOC) of its

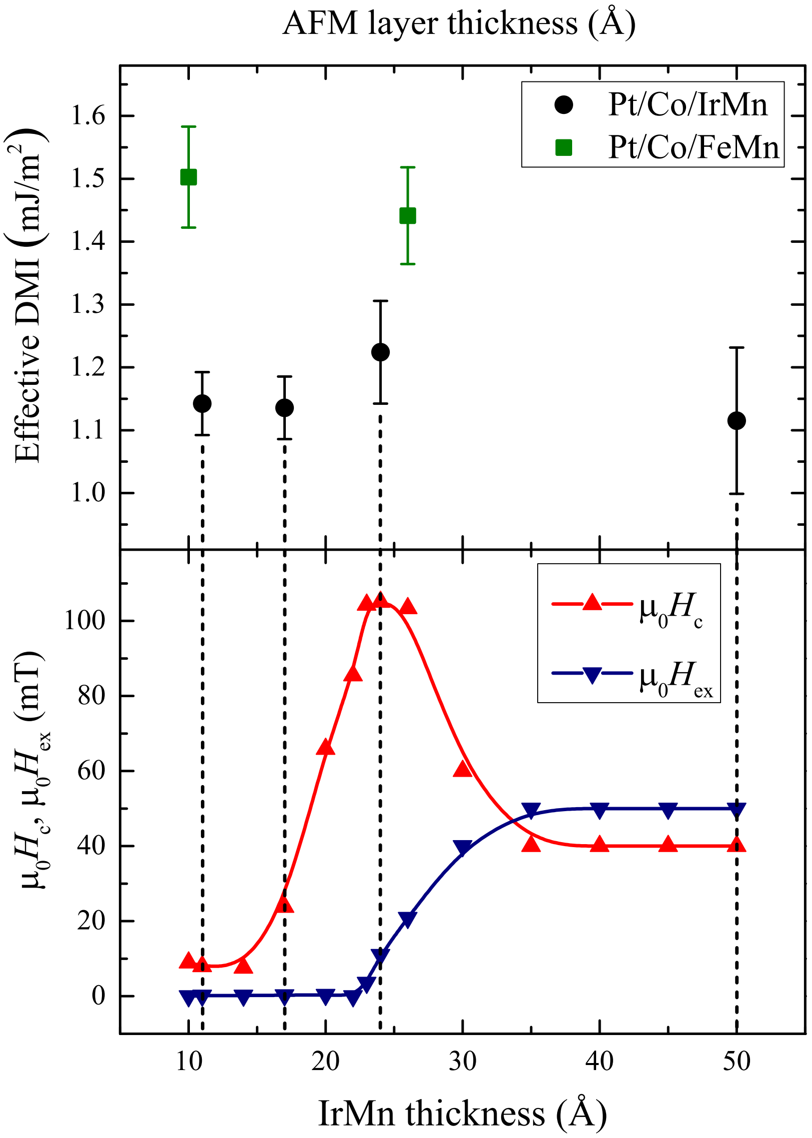

Figure 6.8: The top graph shows the effective DMI as a function of AFM layer thickness for the two systems of (in black) Pt(20 Å)/Co(10 Å)/IrMn(11, 17, 24, and 50 Å), and (in green) Pt(20 Å)/Co(6 Å)/FeMn(10 and 26 Å). The different thicknesses correspond to the different phases of the systems (indicated by dashed lines in the bottom graph for Pt/Co/IrMn). More information on the bottom graph can be found in Section 5.2.2.

electrons, mediates the exchange interaction between two magnetic atoms of the FM layer at the interface. Now, the SOC does not depend on the spin state but rather on the atomic number (which is why heavy elements are usually used as the non-magnetic layer to generate a large DMI). Hence, the DMI is not influenced by the spin order of the AFM layer. Our experiment is in agreement with this theoretical model.

It was shown previously that a FM/AFM system develops an EB field when the volume anisotropy energy of the AFM layer is sufficiently large to resist the torque from the FM layer. From the DMI measurements, we find that the EB does not seem to influence the DMI as it remains unchanged with and without the presence of an EB field. However, we should be cautious with this interpretation as the change in DMI at the CoFeB/IrMn interface as the IrMn film thickness is increased from 1 to 8 nm is reported [40] to be of the order of 0.1 mJ/m^2. Such a small value falls within our experimental uncertainty making it difficult to dismiss a similar change in our Co/IrMn system. The relatively large error for sample (d) is again due to the presence of a thick AFM IrMn layer.

6.5 Comparison of the DMI in the systems

The two systems have a different interfacial DMI D_s. Since the Pt/Co interface is common to both, we infer that the DMI is different at the Co/IrMn and the Co/FeMn interfaces. At these interfaces, we assume that the Mn atoms mostly contribute to the DMI, following the work from Ma *et al.* [40]. In this paper, the authors find the sign of the DMI in CoFeB/Ir and CoFeB/IrMn to be opposite, from which they draw the conclusion of a strong DMI contribution from Mn atoms at the CoFeB/IrMn interface. Thus, for our case, a variation in the DMI could be expected at the Co/IrMn and the Co/FeMn interfaces due to the difference in Mn concentration for the two AFMs used. This interpretation is valid for an ideal Co/FeMn interface. However, the formation of an Fe layer [159] at this interface prompts us to also consider the contribution of both ferromagnetic Fe and Co to the DMI. Further to this, formation of antiferromagnetic CoMn due to intermixing, could also contribute to the generation of the DMI. Lastly, it should be mentioned here that Nembach *et al.* [63] reported a non-trivial relationship between FM thickness and D_s and suggested that FM thickness could also influence the interfacial DMI.

It is worthwhile to mention here that the effective DMI D_eff in the two systems is sufficiently large, especially in the FeMn system, to promote chiral spin configurations. The values obtained are comparable to recent experiments which have seen homochiral Néel walls [161, 43, 62] and room temperature skyrmions [45, 38, 162, 155], and thus, these systems offer the potential to be technologically important.

6.6 Conclusions

In thin film multilayered systems, magnetisation processes are dominated by interface effects. With regard to this, interfacial mechanisms were investigated in exchange coupled systems of Pt/Co/IrMn and Pt/Co/FeMn exhibiting perpendicular magnetic anisotropy and perpendicular exchange bias.

The dependence of the magnetic domain morphology and the interfacial Dzyaloshinskii-Moriya interaction on the antiferromagnetic Néel order were studied. The spin order of the AFM layers was controlled by varying the thicknesses. The magnetic domains were investigated by magneto-optical imaging, while the DMI was measured mainly by Brillouin light scattering spectroscopy, and also by the field-driven domain expansion technique.

It was demonstrated that the domain structure in these systems is influenced by the AFM spin order. A change from large domains with unreversed networks to isolated bubbles with smooth DWs was observed at the point of the AFM phase transition. Then, at the onset of the exchange bias field, the DWs became rough due to enhanced pinning at the FM/AFM interface. These variations are related to the FM-AFM inter-layer exchange coupling and the volume anisotropy energy of the AFM layer.

On the other hand, the DMI was found to be not dictated by the AFM spin order. The DMI in these systems was measured at distinct thicknesses of the involved AFM layers, corresponding to different phases. The DMI remains unchanged, within experimental uncertainty, irrespective of the AFM spin order, and also with and without exchange bias. This observation is in agreement with theory. The DMI was also measured by the bubble expansion method and the obtained value was found to disagree with BLS. Possible underlying causes for this discrepancy was discussed.

Lastly, the experiments show that the DMI slightly differ in the two systems. This behaviour is linked to the different Mn concentration at the FM/AFM interface of the two systems, and also due to Fe segregation from the FeMn layer.

Chapter 7

Conclusion

7.1 Summary

When this project was conceived, the influence of the interfacial Dzyaloshinskii-Moriya interaction on magnetic textures was already established. However, many of its fundamental mechanisms remained to be understood. On that front, this thesis addressed two elementary aspects of the interfacial DMI: its dependence on the interfacial atomic arrangements, and its lack of response to antiferromagnetic spin order. The thesis also investigated the role of exchange coupling on the domain morphology and magnetic properties of perpendicularly exchange biased systems with a view to contribute to the emerging field of antiferromagnetic spintronics.

Perpendicularly magnetised Ta/CoFeB/MgO thin films were annealed systematically at different temperatures ranging from 210-280 °C in order to bring about incremental changes in the atomic order at the interfaces. DMI fields were measured post-annealing and was found to respond to these alterations of the atomic order. The DMI fields were measured using a magnetic field-driven domain wall creep method, where the energy symmetry of an expanding bubble domain is broken by the application of a static in-plane field. To ensure that DW motion occurred within the creep regime during the experimentation, different regimes of DW dynamics were scrutinised for the system.

The DMI measurements revealed that the system attains a maximum DMI of $D = 0.057 \pm 0.003$ mJ/m^2 at a temperature of around 230 °C. Possible underlying mechanisms for the observed trend in the DMI was deduced by linking to anisotropy field measurements, which was also found to follow a similar trend as a function of the annealing temperature. The anisotropy fields were measured magneto-optically utilising coherent rotation of magnetisation for a low field range. The initial rise of the DMI was due to an improved order of the atoms at the interface brought about by annealing. At higher annealing temperatures the DMI decreases, which is related to the diffusion of boron out of the CoFeB layer and consequent accumulation at the adjacent interfaces. These experiments demonstrate the sensitivity of the DMI to the interfacial atomic order; that an improved arrangement of atoms at the interface enhances the DMI, and vice versa.

The thesis also explored the DMI in systems containing an antiferromagnet layer. Heterostructures of Pt/Co/IrMn and Pt/Co/FeMn with perpendicular exchange bias were studied, where different phases of the AFM were accessed by controlling the thickness. The dependence of the magnetic properties, domain morphology and the DMI on the antiferromagnetic Néel order was investigated. A large exchange bias of 40 mT for Pt/Co/IrMn and 140 mT for Pt/Co/FeMn was obtained in the as-grown state. Magneto-optical imaging was employed to observe the domains, while the DMI was measured mainly by Brillouin light scattering spectroscopy, and also by the field-driven domain expansion technique.

Variations in the domain texture were observed, which are related to the FM-AFM inter-layer exchange coupling and the volume anisotropy energy of the AFM layer. At the point of the AFM phase transition the domain structure changes from large domains with unreversed networks to isolated bubbles with smooth DWs. Then, at the onset of the exchange bias field, the DWs become rough due to enhanced pinning at the FM/AFM interface. Contrary to this, the DMI in these systems is not influenced by the AFM spin order or EB, which is in agreement with theory. The experiments show that the DMI remains unchanged in these systems at distinct thicknesses of the AFM layers, corresponding to different phases. Lastly, the DMI is different in the two systems: $D = -1.14 \pm 0.05$ mJ/m^2 for Pt/Co/IrMn and $D = -1.50 \pm 0.08$ mJ/m^2 for Pt/Co/FeMn; the results are from when IrMn and FeMn layers are paramagnetic. The difference in DMI is due to different Mn concentration at the FM/AFM interface of the two systems, and also due to Fe segregation from the FeMn layer.

7.2 Outlook

Continuation of the work in this project is not only interesting, but also important. There are still a number of aspects which deserve further attention, particularly regarding the exchange coupled systems. As we have seen, the atoms at the interface are responsible for the generation of the DMI in multilayer systems. Thus, resolving the elemental composition at the FM/AFM interface of Pt/Co/(IrMn, FeMn) trilayers could provide more information on the origin of the DMI at such interfaces, particularly the Co/FeMn interface, where considerable Fe segregation occurs. Synchrotron experimentation utilising X-rays could be performed to identify the atoms at the interface. Photoemission electron microscopy could be performed in tandem with magnetic element specific imaging to investigate the resulting domain structure.

Antiferromagnetic materials possess excellent magnetotransport properties and are able to generate large torques on adjacent ferromagnetic layers to facilitate efficient current-driven motion of domain walls and skyrmions. Resolving the spin torques in the exchange biased systems of Pt/Co/(IrMn, FeMn) thus could prove to be beneficial. Furthermore, the dependence of these torques on the magnitude of exchange bias could also be useful to know. With this view, experimentation in these multilayers has already begun in quantifying the spin-orbit torques using harmonic Hall voltage measurements. Extensive nanofabrication procedures have been carried out to design the structures required for these experimentation.

Such investigations are important not only from a fundamental point of view, but also in terms of technological applications.

REFERENCES

[1] F. Englert and R. Brout, “Broken symmetry and the mass of gauge vector mesons,” *Physical Review Letters*, vol. 13, no. 9, p. 321, 1964.

[2] P. W. Higgs, “Broken symmetries and the masses of gauge bosons,” *Physical Review Letters*, vol. 13, no. 16, p. 508, 1964.

[3] W. T. B. Kelvin, *The molecular tactics of a crystal*. Clarendon Press, 1894.

[4] G. Volovik and M. Krusius, “Chiral quantum textures,” *Physics*, vol. 5, p. 130, 2012.

[5] I. Dzyaloshinsky, “A thermodynamic theory of "weak" ferromagnetism of antiferromagnetics,” *Journal of Physics and Chemistry of Solids*, vol. 4, no. 4, pp. 241–255, 1958.

[6] T. Moriya, “Anisotropic superexchange interaction and weak ferromagnetism,” *Physical Review*, vol. 120, no. 1, p. 91, 1960.

[7] A. Fert and P. M. Levy, “Role of anisotropic exchange interactions in determining the properties of spin-glasses,” *Physical Review Letters*, vol. 44, no. 23, p. 1538, 1980.

[8] A. Fert, “Magnetic and transport properties of metallic multilayers,” in *Materials Science Forum*, vol. 59, pp. 439–480, Trans Tech Publ, 1990.

[9] S. Mangin, D. Ravelosona, J. Katine, M. Carey, B. Terris, and E. E. Fullerton, “Current-induced magnetization reversal in nanopillars with perpendicular anisotropy,” *Nature Materials*, vol. 5, no. 3, p. 210, 2006.

[10] D. A. Allwood, G. Xiong, C. Faulkner, D. Atkinson, D. Petit, and R. Cowburn, "Magnetic domain-wall logic," *Science*, vol. 309, no. 5741, pp. 1688–1692, 2005.

[11] S. Tehrani, J. M. Slaughter, M. Deherrera, B. N. Engel, N. D. Rizzo, J. Salter, M. Durlam, R. W. Dave, J. Janesky, B. Butcher, *et al.*, "Magnetoresistive random access memory using magnetic tunnel junctions," *Proceedings of the IEEE*, vol. 91, no. 5, pp. 703–714, 2003.

[12] I. Žutić, J. Fabian, and S. D. Sarma, "Spintronics: Fundamentals and applications," *Reviews of Modern Physics*, vol. 76, no. 2, p. 323, 2004.

[13] C. Chappert, A. Fert, and F. N. Van Dau, "The emergence of spin electronics in data storage," *Nature Materials*, vol. 6, no. 11, p. 813, 2007.

[14] A. Brataas, A. D. Kent, and H. Ohno, "Current-induced torques in magnetic materials," *Nature Materials*, vol. 11, no. 5, p. 372, 2012.

[15] M. N. Baibich, J. M. Broto, A. Fert, F. N. Van Dau, F. Petroff, P. Etienne, G. Creuzet, A. Friederich, and J. Chazelas, "Giant magnetoresistance of (001)Fe/(001)Cr magnetic superlattices," *Physical Review Letters*, vol. 61, no. 21, p. 2472, 1988.

[16] G. Binasch, P. Grünberg, F. Saurenbach, and W. Zinn, "Enhanced magnetoresistance in layered magnetic structures with antiferromagnetic interlayer exchange," *Physical Review B*, vol. 39, no. 7, p. 4828, 1989.

[17] B. Dieny, "Giant magnetoresistance in spin-valve multilayers," *Journal of Magnetism and Magnetic Materials*, vol. 136, no. 3, pp. 335–359, 1994.

[18] A. D. Kent and D. C. Worledge, "A new spin on magnetic memories," *Nature Nanotechnology*, vol. 10, no. 3, p. 187, 2015.

[19] H.-S. P. Wong and S. Salahuddin, "Memory leads the way to better computing," *Nature Nanotechnology*, vol. 10, no. 3, p. 191, 2015.

[20] X. Yao, J. Harms, A. Lyle, F. Ebrahimi, Y. Zhang, and J.-P. Wang, "Magnetic tunnel junction-based spintronic logic units operated by spin

transfer torque," *IEEE Transactions on Nanotechnology*, vol. 11, no. 1, pp. 120–126, 2012.

[21] S. Wolf, D. Awschalom, R. Buhrman, J. Daughton, S. Von Molnar, M. Roukes, A. Y. Chtchelkanova, and D. Treger, "Spintronics: a spin-based electronics vision for the future," *Science*, vol. 294, no. 5546, pp. 1488–1495, 2001.

[22] W. Heisenberg, "Mehrkörperproblem und resonanz in der quantenmechanik," *Zeitschrift für Physik*, vol. 38, no. 6-7, pp. 411–426, 1926.

[23] P. A. M. Dirac, "On the theory of quantum mechanics," *Proc. R. Soc. Lond. A*, vol. 112, no. 762, pp. 661–677, 1926.

[24] M. Uchida, Y. Onose, Y. Matsui, and Y. Tokura, "Real-space observation of helical spin order," *Science*, vol. 311, no. 5759, pp. 359–361, 2006.

[25] U. Rößler, A. Bogdanov, and C. Pfleiderer, "Spontaneous skyrmion ground states in magnetic metals," *Nature*, vol. 442, no. 7104, p. 797, 2006.

[26] S. Mühlbauer, B. Binz, F. Jonietz, C. Pfleiderer, A. Rosch, A. Neubauer, R. Georgii, and P. Böni, "Skyrmion lattice in a chiral magnet," *Science*, vol. 323, no. 5916, pp. 915–919, 2009.

[27] X. Yu, Y. Onose, N. Kanazawa, J. Park, J. Han, Y. Matsui, N. Nagaosa, and Y. Tokura, "Real-space observation of a two-dimensional skyrmion crystal," *Nature*, vol. 465, no. 7300, p. 901, 2010.

[28] M. Bode, M. Heide, K. Von Bergmann, P. Ferriani, S. Heinze, G. Bihlmayer, A. Kubetzka, O. Pietzsch, S. Blügel, and R. Wiesendanger, "Chiral magnetic order at surfaces driven by inversion asymmetry," *Nature*, vol. 447, no. 7141, p. 190, 2007.

[29] S. Meckler, N. Mikuszeit, A. Preßler, E. Vedmedenko, O. Pietzsch, and R. Wiesendanger, "Real-space observation of a right-rotating inhomogeneous cycloidal spin spiral by spin-polarized scanning tunneling

microscopy in a triple axes vector magnet," *Physical Review Letters*, vol. 103, no. 15, p. 157201, 2009.

[30] G. Chen, J. Zhu, A. Quesada, J. Li, A. T. N'Diaye, Y. Huo, T. P. Ma, Y. Chen, H. Y. Kwon, C. Won, *et al.*, "Novel chiral magnetic domain wall structure in Fe/Ni/Cu(001) films," *Physical Review Letters*, vol. 110, no. 17, p. 177204, 2013.

[31] N. Nakajima, T. Koide, T. Shidara, H. Miyauchi, H. Fukutani, A. Fujimori, K. Iio, T. Katayama, M. Nỳvlt, and Y. Suzuki, "Perpendicular magnetic anisotropy caused by interfacial hybridization via enhanced orbital moment in Co/Pt multilayers: Magnetic circular x-ray dichroism study," *Physical Review Letters*, vol. 81, no. 23, p. 5229, 1998.

[32] S. S. Parkin, M. Hayashi, and L. Thomas, "Magnetic domain-wall racetrack memory," *Science*, vol. 320, no. 5873, pp. 190–194, 2008.

[33] S. Emori, U. Bauer, S.-M. Ahn, E. Martinez, and G. S. Beach, "Current-driven dynamics of chiral ferromagnetic domain walls," *Nature Materials*, vol. 12, no. 7, pp. 611–616, 2013.

[34] K.-S. Ryu, L. Thomas, S.-H. Yang, and S. Parkin, "Chiral spin torque at magnetic domain walls," *Nature Nanotechnology*, vol. 8, no. 7, pp. 527–533, 2013.

[35] S.-G. Je, D.-H. Kim, S.-C. Yoo, B.-C. Min, K.-J. Lee, and S.-B. Choe, "Asymmetric magnetic domain-wall motion by the Dzyaloshinskii-Moriya interaction," *Physical Review B*, vol. 88, no. 21, p. 214401, 2013.

[36] A. Hrabec, N. Porter, A. Wells, M. Benitez, G. Burnell, S. McVitie, D. McGrouther, T. Moore, and C. Marrows, "Measuring and tailoring the Dzyaloshinskii-Moriya interaction in perpendicularly magnetized thin films," *Physical Review B*, vol. 90, no. 2, p. 020402, 2014.

[37] S. Pizzini, J. Vogel, S. Rohart, L. Buda-Prejbeanu, E. Jué, O. Boulle, I. M. Miron, C. Safeer, S. Auffret, G. Gaudin, *et al.*, "Chirality-induced asymmetric magnetic nucleation in Pt/Co/AlO$_x$ ultrathin

microstructures," *Physical Review Letters*, vol. 113, no. 4, p. 047203, 2014.

[38] O. Boulle, J. Vogel, H. Yang, S. Pizzini, D. d. S. Chaves, A. Locatelli, T. O. M. A. Sala, L. D. Buda-Prejbeanu, O. Klein, M. Belmeguenai, *et al.*, "Room temperature chiral magnetic skyrmion in ultrathin magnetic nanostructures," *Nature Nanotechnology*, vol. 11, no. 5, p. 449, 2016.

[39] A. Belabbes, G. Bihlmayer, S. Blügel, and A. Manchon, "Oxygen-enabled control of Dzyaloshinskii-Moriya interaction in ultra-thin magnetic films," *Scientific Reports*, vol. 6, 2016.

[40] X. Ma, G. Yu, S. A. Razavi, S. S. Sasaki, X. Li, K. Hao, S. H. Tolbert, K. L. Wang, and X. Li, "Dzyaloshinskii-Moriya interaction across antiferromagnet-ferromagnet interface," *Physical Review Letters*, vol. 119, no. 2, p. 027202, 2017.

[41] A. Thiaville, S. Rohart, É. Jué, V. Cros, and A. Fert, "Dynamics of Dzyaloshinskii domain walls in ultrathin magnetic films," *EPL (Europhysics Letters)*, vol. 100, no. 5, p. 57002, 2012.

[42] G. Chen, T. Ma, H. Kwon, C. Won, Y. Wu, A. K. Schmid, *et al.*, "Tailoring the chirality of magnetic domain walls by interface engineering," *Nature Communications*, vol. 4, p. 2671, 2013.

[43] M. Benitez, A. Hrabec, A. Mihai, T. Moore, G. Burnell, D. McGrouther, C. Marrows, and S. McVitie, "Magnetic microscopy and topological stability of homochiral néel domain walls in a Pt/Co/AlO$_x$ trilayer," *Nature Communications*, vol. 6, 2015.

[44] A. Fert, V. Cros, and J. Sampaio, "Skyrmions on the track," *Nature Nanotechnology*, vol. 8, no. 3, pp. 152–156, 2013.

[45] C. Moreau-Luchaire, C. Moutafis, N. Reyren, J. Sampaio, C. Vaz, N. Van Horne, K. Bouzehouane, K. Garcia, C. Deranlot, P. Warnicke,

et al., “Additive interfacial chiral interaction in multilayers for stabilization of small individual skyrmions at room temperature,” *Nature Nanotechnology*, vol. 11, no. 5, pp. 444–448, 2016.

[46] A. Fert, N. Reyren, and V. Cros, “Magnetic skyrmions: advances in physics and potential applications,” *Nature Reviews Materials*, vol. 2, p. 17031, 2017.

[47] M. Hayashi, L. Thomas, R. Moriya, C. Rettner, and S. S. Parkin, “Current-controlled magnetic domain-wall nanowire shift register,” *Science*, vol. 320, no. 5873, pp. 209–211, 2008.

[48] L. Liu, C.-F. Pai, Y. Li, H. Tseng, D. Ralph, and R. Buhrman, “Spin-torque switching with the giant spin hall effect of tantalum,” *Science*, vol. 336, no. 6081, pp. 555–558, 2012.

[49] V. Tshitoyan, C. Ciccarelli, A. Mihai, M. Ali, A. Irvine, T. Moore, T. Jungwirth, and A. Ferguson, “Electrical manipulation of ferromagnetic NiFe by antiferromagnetic IrMn,” *Physical Review B*, vol. 92, no. 21, p. 214406, 2015.

[50] P. Ferriani, K. Von Bergmann, E. Vedmedenko, S. Heinze, M. Bode, M. Heide, G. Bihlmayer, S. Blügel, and R. Wiesendanger, “Atomic-scale spin spiral with a unique rotational sense: Mn monolayer on W(001),” *Physical Review Letters*, vol. 101, no. 2, p. 027201, 2008.

[51] H. Yang, A. Thiaville, S. Rohart, A. Fert, and M. Chshiev, “Anatomy of Dzyaloshinskii-Moriya interaction at Co/Pt interfaces,” *Physical Review Letters*, vol. 115, no. 26, p. 267210, 2015.

[52] D.-Y. Kim, D.-H. Kim, J. Moon, and S.-B. Choe, “Determination of magnetic domain-wall types using Dzyaloshinskii-Moriya-interaction-induced domain patterns,” *Applied Physics Letters*, vol. 106, no. 26, p. 262403, 2015.

[53] R. Lavrijsen, D. Hartmann, A. van den Brink, Y. Yin, B. Barcones, R. Duine, M. Verheijen, H. Swagten, and B. Koopmans, “Asymmetric magnetic bubble expansion under in-plane field in Pt/Co/Pt: Effect

of interface engineering," *Physical Review B*, vol. 91, no. 10, p. 104414, 2015.

[54] M. Vaňatka, J.-C. Rojas-Sánchez, J. Vogel, M. Bonfim, M. Belmeguenai, Y. Roussigné, A. Stashkevich, A. Thiaville, and S. Pizzini, "Velocity asymmetry of Dzyaloshinskii domain walls in the creep and flow regimes," *Journal of Physics: Condensed Matter*, vol. 27, no. 32, p. 326002, 2015.

[55] E. Jué, C. Safeer, M. Drouard, A. Lopez, P. Balint, L. Buda-Prejbeanu, O. Boulle, S. Auffret, A. Schuhl, A. Manchon, *et al.*, "Chiral damping of magnetic domain walls," *Nature Materials*, 2015.

[56] C. A. Akosa, I. M. Miron, G. Gaudin, and A. Manchon, "Phenomenology of chiral damping in noncentrosymmetric magnets," *Physical Review B*, vol. 93, no. 21, p. 214429, 2016.

[57] D. Lau, V. Sundar, J.-G. Zhu, and V. Sokalski, "Energetic molding of chiral magnetic bubbles," *Physical Review B*, vol. 94, no. 6, p. 060401, 2016.

[58] J. Pellegren, D. Lau, and V. Sokalski, "Dispersive stiffness of Dzyaloshinskii domain walls," *Physical Review Letters*, vol. 119, no. 2, p. 027203, 2017.

[59] J.-H. Moon, S.-M. Seo, K.-J. Lee, K.-W. Kim, J. Ryu, H.-W. Lee, R. D. McMichael, and M. D. Stiles, "Spin-wave propagation in the presence of interfacial Dzyaloshinskii-Moriya interaction," *Physical Review B*, vol. 88, no. 18, p. 184404, 2013.

[60] K. Di, V. L. Zhang, H. S. Lim, S. C. Ng, M. H. Kuok, J. Yu, J. Yoon, X. Qiu, and H. Yang, "Direct observation of the Dzyaloshinskii-Moriya interaction in a Pt/Co/Ni film," *Physical Review Letters*, vol. 114, no. 4, p. 047201, 2015.

[61] J. Cho, N.-H. Kim, S. Lee, J.-S. Kim, R. Lavrijsen, A. Solignac, Y. Yin, D.-S. Han, N. J. van Hoof, H. J. Swagten, *et al.*, "Thickness depend-

ence of the interfacial Dzyaloshinskii-Moriya interaction in inversion symmetry broken systems," *Nature Communications*, vol. 6, 2015.

[62] M. Belmeguenai, J.-P. Adam, Y. Roussigné, S. Eimer, T. Devolder, J.-V. Kim, S. M. Cherif, A. Stashkevich, and A. Thiaville, "Interfacial Dzyaloshinskii-Moriya interaction in perpendicularly magnetized Pt/Co/AlO$_x$ ultrathin films measured by Brillouin light spectroscopy," *Physical Review B*, vol. 91, no. 18, p. 180405, 2015.

[63] H. T. Nembach, J. M. Shaw, M. Weiler, E. Jué, and T. J. Silva, "Linear relation between heisenberg exchange and interfacial Dzyaloshinskii–Moriya interaction in metal films," *Nature Physics*, vol. 11, no. 10, p. 825, 2015.

[64] R. Soucaille, M. Belmeguenai, J. Torrejon, J.-V. Kim, T. Devolder, Y. Roussigné, S.-M. Chérif, A. Stashkevich, M. Hayashi, and J.-P. Adam, "Probing the Dzyaloshinskii-Moriya interaction in CoFeB ultrathin films using domain wall creep and Brillouin light spectroscopy," *Physical Review B*, vol. 94, no. 10, p. 104431, 2016.

[65] D.-S. Han, N.-H. Kim, J.-S. Kim, Y. Yin, J.-W. Koo, J. Cho, S. Lee, M. Kläui, H. J. Swagten, B. Koopmans, *et al.*, "Asymmetric hysteresis for probing Dzyaloshinskii–Moriya interaction," *Nano Letters*, vol. 16, no. 7, pp. 4438–4446, 2016.

[66] R. Yanes, J. Jackson, L. Udvardi, L. Szunyogh, and U. Nowak, "Exchange bias driven by Dzyaloshinskii-Moriya interactions," *Physical Review Letters*, vol. 111, no. 21, p. 217202, 2013.

[67] R. Hiramatsu, K.-J. Kim, Y. Nakatani, T. Moriyama, and T. Ono, "Proposal for quantifying the Dzyaloshinsky–Moriya interaction by domain walls annihilation measurement," *Japanese Journal of Applied Physics*, vol. 53, no. 10, p. 108001, 2014.

[68] D. Ravelosona, D. Lacour, J. Katine, B. Terris, and C. Chappert, "Nanometer scale observation of high efficiency thermally assisted current-driven domain wall depinning," *Physical Review Letters*, vol. 95, no. 11, p. 117203, 2005.

[69] D. C. Ralph and M. D. Stiles, "Spin transfer torques," *Journal of Magnetism and Magnetic Materials*, vol. 320, no. 7, pp. 1190–1216, 2008.

[70] D. Ravelosona, S. Mangin, Y. Lemaho, J. Katine, B. Terris, and E. E. Fullerton, "Domain wall creation in nanostructures driven by a spin-polarized current," *Physical Review Letters*, vol. 96, no. 18, p. 186604, 2006.

[71] L. Berger, "Low-field magnetoresistance and domain drag in ferromagnets," *Journal of Applied Physics*, vol. 49, no. 3, pp. 2156–2161, 1978.

[72] I. M. Miron, G. Gaudin, S. Auffret, B. Rodmacq, A. Schuhl, S. Pizzini, J. Vogel, and P. Gambardella, "Current-driven spin torque induced by the Rashba effect in a ferromagnetic metal layer," *Nature Materials*, vol. 9, no. 3, pp. 230–234, 2010.

[73] I. M. Miron, T. Moore, H. Szambolics, L. D. Buda-Prejbeanu, S. Auffret, B. Rodmacq, S. Pizzini, J. Vogel, M. Bonfim, A. Schuhl, *et al.*, "Fast current-induced domain-wall motion controlled by the Rashba effect," *Nature Materials*, vol. 10, no. 6, pp. 419–423, 2011.

[74] T. A. Moore, I. Miron, G. Gaudin, G. Serret, S. Auffret, B. Rodmacq, A. Schuhl, S. Pizzini, J. Vogel, and M. Bonfim, "High domain wall velocities induced by current in ultrathin Pt/Co/AlO$_x$ wires with perpendicular magnetic anisotropy," *Applied Physics Letters*, vol. 93, no. 26, p. 262504, 2008.

[75] Y. A. Bychkov and E. I. Rashba, "Oscillatory effects and the magnetic susceptibility of carriers in inversion layers," *Journal of physics C: Solid state physics*, vol. 17, no. 33, p. 6039, 1984.

[76] M. Dyakonov and V. Perel, "Current-induced spin orientation of electrons in semiconductors," *Physics Letters A*, vol. 35, no. 6, pp. 459–460, 1971.

[77] G. Dresselhaus, "Spin-orbit coupling effects in zinc blende structures," *Physical Review*, vol. 100, no. 2, p. 580, 1955.

[78] M. Heide, G. Bihlmayer, and S. Blügel, "Dzyaloshinskii-Moriya interaction accounting for the orientation of magnetic domains in ultrathin films: Fe/W(110)," *Physical Review B*, vol. 78, no. 14, p. 140403, 2008.

[79] M. L. Néel, "Propriétés magnétiques des ferrites; ferrimagnétisme et antiferromagnétisme," in *Annales de Physique*, vol. 12, pp. 137–198, 1948.

[80] T. Jungwirth, X. Marti, P. Wadley, and J. Wunderlich, "Antiferromagnetic spintronics," *Nature Nanotechnology*, vol. 11, no. 3, p. 231, 2016.

[81] C. Marrows, "Three-dimensional exchange bias in $\{\mathrm{Co/Pd}\}_N$/FeMn," *Physical Review B*, vol. 68, no. 1, p. 012405, 2003.

[82] P. Němec, M. Fiebig, T. Kampfrath, and A. V. Kimel, "Antiferromagnetic opto-spintronics," *Nature Physics*, p. 1, 2018.

[83] J. Sinova, S. O. Valenzuela, J. Wunderlich, C. Back, and T. Jungwirth, "Spin Hall effects," *Reviews of Modern Physics*, vol. 87, no. 4, p. 1213, 2015.

[84] T. Satoh, S.-J. Cho, R. Iida, T. Shimura, K. Kuroda, H. Ueda, Y. Ueda, B. Ivanov, F. Nori, and M. Fiebig, "Spin oscillations in antiferromagnetic nio triggered by circularly polarized light," *Physical Review Letters*, vol. 105, no. 7, p. 077402, 2010.

[85] J. Železnỳ, P. Wadley, K. Olejník, A. Hoffmann, and H. Ohno, "Spin transport and spin torque in antiferromagnetic devices," *Nature Physics*, p. 1, 2018.

[86] V. Baltz, A. Manchon, M. Tsoi, T. Moriyama, T. Ono, and Y. Tserkovnyak, "Antiferromagnetic spintronics," *Reviews of Modern Physics*, vol. 90, no. 1, p. 015005, 2018.

[87] W. H. Meiklejohn and C. P. Bean, "New magnetic anisotropy," *Physical Review*, vol. 102, no. 5, p. 1413, 1956.

[88] M. Blamire and B. Hickey, "Magnetic materials: Compensating for bias," *Nature Materials*, vol. 5, no. 2, p. 87, 2006.

[89] P. Wadley, B. Howells, J. Železnỳ, C. Andrews, V. Hills, R. P. Campion, V. Novák, K. Olejník, F. Maccherozzi, S. Dhesi, *et al.*, "Electrical switching of an antiferromagnet," *Science*, vol. 351, no. 6273, pp. 587–590, 2016.

[90] K. Olejník, V. Schuler, X. Martí, V. Novák, Z. Kašpar, P. Wadley, R. P. Campion, K. W. Edmonds, B. L. Gallagher, J. Garcés, *et al.*, "Antiferromagnetic cumnas multi-level memory cell with microelectronic compatibility," *Nature Communications*, vol. 8, p. 15434, 2017.

[91] S. Manz, M. Matsubara, T. Lottermoser, J. Büchi, A. Iyama, T. Kimura, D. Meier, and M. Fiebig, "Reversible optical switching of antiferromagnetism in $TbMnO_3$," *Nature Photonics*, vol. 10, no. 10, p. 653, 2016.

[92] S. Fukami, C. Zhang, S. DuttaGupta, A. Kurenkov, and H. Ohno, "Magnetization switching by spin-orbit torque in an antiferromagnet-ferromagnet bilayer system," *Nature Materials*, vol. 15, no. 5, pp. 535–541, 2016.

[93] Y.-W. Oh, S.-h. C. Baek, Y. Kim, H. Y. Lee, K.-D. Lee, C.-G. Yang, E.-S. Park, K.-S. Lee, K.-W. Kim, G. Go, *et al.*, "Field-free switching of perpendicular magnetization through spin–orbit torque in antiferromagnet/ferromagnet/oxide structures," *Nature Nanotechnology*, vol. 11, no. 10, pp. 878–884, 2016.

[94] A. van den Brink, G. Vermijs, A. Solignac, J. Koo, J. Kohlhepp, H. Swagten, and B. Koopmans, "Field-free magnetization reversal by spin-hall effect and exchange bias," *Nature Communications*, vol. 7, 2016.

[95] L. Liu, T. Moriyama, D. Ralph, and R. Buhrman, "Spin-torque ferromagnetic resonance induced by the spin Hall effect," *Physical Review Letters*, vol. 106, no. 3, p. 036601, 2011.

[96] S.-H. Yang, K.-S. Ryu, and S. Parkin, “Domain-wall velocities of up to 750 ms^{-1} driven by exchange-coupling torque in synthetic antiferromagnets,” *Nature Nanotechnology*, vol. 10, no. 3, pp. 221–226, 2015.

[97] B. D. Cullity and C. D. Graham, *Introduction to magnetic materials*. John Wiley & Sons, 2011.

[98] R. Skomski, *Simple models of magnetism*. Oxford University Press on Demand, 2008.

[99] W. Pauli, “Über den zusammenhang des abschlusses der elektronengruppen im atom mit der komplexstruktur der spektren,” *Zeitschrift für Physik*, vol. 31, no. 1, pp. 765–783, 1925.

[100] E. C. Stoner *et al.*, “Collective electron ferromagnetism,” *Proc. R. Soc. Lond. A*, vol. 165, no. 922, pp. 372–414, 1938.

[101] B. Cui, C. Song, G. Wang, Y. Wang, F. Zeng, and F. Pan, “Perpendicular magnetic anisotropy in CoFeB/X (X= MgO, Ta, W, Ti, and Pt) multilayers,” *Journal of Alloys and Compounds*, vol. 559, pp. 112–115, 2013.

[102] F. Bloch, “Zur theorie des austauschproblems und der remanenzerscheinung der ferromagnetika,” in *Zur Theorie des Austauschproblems und der Remanenzerscheinung der Ferromagnetika*, pp. 295–335, Springer, 1932.

[103] S. Lemerle, J. Ferré, C. Chappert, V. Mathet, T. Giamarchi, and P. Le Doussal, “Domain wall creep in an ising ultrathin magnetic film,” *Physical Review Letters*, vol. 80, no. 4, p. 849, 1998.

[104] P. Metaxas, J. Jamet, A. Mougin, M. Cormier, J. Ferré, V. Baltz, B. Rodmacq, B. Dieny, and R. Stamps, “Creep and flow regimes of magnetic domain-wall motion in ultrathin Pt/Co/Pt films with perpendicular anisotropy,” *Physical Review Letters*, vol. 99, no. 21, p. 217208, 2007.

[105] J. Gorchon, S. Bustingorry, J. Ferré, V. Jeudy, A. B. Kolton, and T. Giamarchi, “Pinning-dependent field-driven domain wall dynam-

ics and thermal scaling in an ultrathin Pt/Co/Pt magnetic film," *Physical Review Letters*, vol. 113, no. 2, p. 027205, 2014.

[106] V. Repain, M. Bauer, J.-P. Jamet, J. Ferré, A. Mougin, C. Chappert, and H. Bernas, "Creep motion of a magnetic wall: Avalanche size divergence," *EPL (Europhysics Letters)*, vol. 68, no. 3, p. 460, 2004.

[107] S. Bustingorry, A. Kolton, and T. Giamarchi, "Thermal rounding of the depinning transition in ultrathin Pt/Co/Pt films," *Physical Review B*, vol. 85, no. 21, p. 214416, 2012.

[108] N. L. Schryer and L. R. Walker, "The motion of 180° domain walls in uniform dc magnetic fields," *Journal of Applied Physics*, vol. 45, no. 12, pp. 5406–5421, 1974.

[109] K. Wasa, M. Kitabatake, and H. Adachi, *Thin film materials technology: sputtering of control compound materials*. Springer Science & Business Media, 2004.

[110] S. Foner, "Versatile and sensitive vibrating-sample magnetometer," *Review of Scientific Instruments*, vol. 30, no. 7, pp. 548–557, 1959.

[111] N. A. Porter, "Magnetoresistance in n-type silicon," *Doctoral thesis, School of Physics and Astronomy, University of Leeds*, 2017.

[112] R. Fagaly, "Superconducting quantum interference device instruments and applications," *Review of Scientific Instruments*, vol. 77, no. 10, p. 101101, 2006.

[113] W. H. Bragg and W. L. Bragg, "The reflection of x-rays by crystals," *Proc. R. Soc. Lond. A*, vol. 88, no. 605, pp. 428–438, 1913.

[114] H. Kiessig, "Untesuchungen zur totalreflektion von röntgenstrahlen, und interferenzen von röntgenstrahlen an dunnen schichten," *Ann. Phys.*, vol. 10, pp. 769–788, 1931.

[115] J. Kerr, "On rotation of the plane of polarization by reflection from the pole of a magnet," *The London, Edinburgh, and Dublin Philosophical Magazine and Journal of Science*, vol. 3, no. 19, pp. 321–343, 1877.

[116] J. Zak, E. Moog, C. Liu, and S. Bader, "Fundamental magneto-optics," *Journal of Applied Physics*, vol. 68, no. 8, pp. 4203–4207, 1990.

[117] R. Schäfer, ""Investigation of domains and dynamics of domain walls by the magneto-optical Kerr effect", in "The Handbook of Magnetism and Advanced Magnetic Materials", edited by H. Kronmüller and S. S. P. Parkin," *Wiley*, 2017.

[118] G. Daalderop, F. Mueller, R. Albers, and A. Boring, "Theory of the magneto-optic Kerr-effect in NiUSn," *Journal of Magnetism and Magnetic Materials*, vol. 74, no. 2, pp. 211–218, 1988.

[119] D. Allwood, G. Xiong, M. Cooke, and R. Cowburn, "Magneto-optical Kerr effect analysis of magnetic nanostructures," *Journal of Physics D: Applied Physics*, vol. 36, no. 18, p. 2175, 2003.

[120] P. Kasiraj, R. Shelby, J. Best, and D. Horne, "Magnetic domain imaging with a scanning Kerr effect microscope," *IEEE Transactions on Magnetics*, vol. 22, no. 5, pp. 837–839, 1986.

[121] R. L. Conte, A. Hrabec, A. Mihai, T. Schulz, S.-J. Noh, C. Marrows, T. Moore, and M. Kläui, "Spin-orbit torque-driven magnetization switching and thermal effects studied in Ta/CoFeB/MgO nanowires," *Applied Physics Letters*, vol. 105, no. 12, p. 122404, 2014.

[122] R. L. Conte, E. Martinez, A. Hrabec, A. Lamperti, T. Schulz, L. Nasi, L. Lazzarini, R. Mantovan, F. Maccherozzi, S. Dhesi, *et al.*, "Role of B diffusion in the interfacial Dzyaloshinskii-Moriya interaction in Ta/$Co_{20}Fe_{60}B_{20}$/MgO nanowires," *Physical Review B*, vol. 91, no. 1, p. 014433, 2015.

[123] C. Burrowes, N. Vernier, J.-P. Adam, L. H. Diez, K. Garcia, I. Barisic, G. Agnus, S. Eimer, J.-V. Kim, T. Devolder, *et al.*, "Low depinning fields in Ta-CoFeB-MgO ultrathin films with perpendicular magnetic anisotropy," *Applied Physics Letters*, vol. 103, no. 18, p. 182401, 2013.

[124] W. Zhao, T. Devolder, Y. Lakys, J.-O. Klein, C. Chappert, and P. Mazoyer, "Design considerations and strategies for high-reliable

STT-MRAM," *Microelectronics Reliability*, vol. 51, no. 9, pp. 1454–1458, 2011.

[125] J. Torrejon, J. Kim, J. Sinha, S. Mitani, M. Hayashi, M. Yamanouchi, and H. Ohno, "Interface control of the magnetic chirality in CoFeB/MgO heterostructures with heavy-metal underlayers," *Nature Communications*, vol. 5, 2014.

[126] S. Cardoso, C. Cavaco, R. Ferreira, L. Pereira, M. Rickart, P. Freitas, N. Franco, J. Gouveia, and N. Barradas, "Characterization of CoFeB electrodes for tunnel junctions," *Journal of applied physics*, vol. 97, no. 10, pp. 10C916–10C916, 2005.

[127] A. W. J. Wells, "Interface morphology and Dzyaloshinskii-Moriya interaction in Pt/Co thin films," *Doctoral thesis, School of Physics and Astronomy, University of Leeds*, 2017.

[128] P. Chauve, T. Giamarchi, and P. Le Doussal, "Creep and depinning in disordered media," *Physical Review B*, vol. 62, no. 10, p. 6241, 2000.

[129] K.-J. Kim, J.-C. Lee, S.-M. Ahn, K.-S. Lee, C.-W. Lee, Y. J. Cho, S. Seo, K.-H. Shin, S.-B. Choe, and H.-W. Lee, "Interdimensional universality of dynamic interfaces," *Nature*, vol. 458, no. 7239, pp. 740–742, 2009.

[130] C. O. Avci, K. Garello, C. Nistor, S. Godey, B. Ballesteros, A. Mugarza, A. Barla, M. Valvidares, E. Pellegrin, A. Ghosh, *et al.*, "Field-like and antidamping spin-orbit torques in as-grown and annealed Ta/CoFeB/MgO layers," *Physical Review B*, vol. 89, no. 21, p. 214419, 2014.

[131] P. M. Shepley, "Effect of piezoelectric strain on the magnetic properties of Pt/Co thin films," *Doctoral thesis, School of Physics and Astronomy, University of Leeds*, 2015.

[132] H. Bouchikhaoui, P. Stender, D. Akemeier, D. Baither, K. Hono, A. Hütten, and G. Schmitz, "On the role of Ta cap in the recrystallization process of CoFeB layers," *Applied Physics Letters*, vol. 103, no. 14, p. 142412, 2013.

[133] D. Worledge, G. Hu, D. W. Abraham, J. Sun, P. Trouilloud, J. Nowak, S. Brown, M. Gaidis, E. O'sullivan, and R. Robertazzi, "Spin torque switching of perpendicular Ta | CoFeB | MgO-based magnetic tunnel junctions," *Applied Physics Letters*, vol. 98, no. 2, p. 022501, 2011.

[134] R. Duine, "Spintronics: An alternating alternative," *Nature Materials*, vol. 10, no. 5, pp. 344–345, 2011.

[135] S. Fukami, T. Suzuki, K. Nagahara, N. Ohshima, Y. Ozaki, S. Saito, R. Nebashi, N. Sakimura, H. Honjo, K. Mori, *et al.*, "Low-current perpendicular domain wall motion cell for scalable high-speed MRAM," in *2009 Symposium on VLSI Technology*, 2009.

[136] W. Zhang, W. Han, S.-H. Yang, Y. Sun, Y. Zhang, B. Yan, and S. S. Parkin, "Giant facet-dependent spin-orbit torque and spin Hall conductivity in the triangular antiferromagnet $\mathrm{IrMn_3}$," *Science Advances*, vol. 2, no. 9, p. e1600759, 2016.

[137] S. Maat, K. Takano, S. Parkin, and E. E. Fullerton, "Perpendicular exchange bias of Co/Pt multilayers," *Physical Review Letters*, vol. 87, no. 8, p. 087202, 2001.

[138] F. Garcia, G. Casali, S. Auffret, B. Rodmacq, and B. Dieny, "Exchange bias in $(\mathrm{Pt/Co_{0.9}Fe_{0.1}})_n$/FeMn multilayers with perpendicular magnetic anisotropy," *Journal of Applied Physics*, vol. 91, no. 10, pp. 6905–6907, 2002.

[139] J. Sort, V. Baltz, F. Garcia, B. Rodmacq, and B. Dieny, "Tailoring perpendicular exchange bias in [Pt/Co]-IrMn multilayers," *Physical Review B*, vol. 71, no. 5, p. 054411, 2005.

[140] W. Zhang, M. B. Jungfleisch, W. Jiang, J. E. Pearson, A. Hoffmann, F. Freimuth, and Y. Mokrousov, "Spin Hall effects in metallic antiferromagnets," *Physical Review Letters*, vol. 113, no. 19, p. 196602, 2014.

[141] L. Liu, O. Lee, T. Gudmundsen, D. Ralph, and R. Buhrman, "Current-induced switching of perpendicularly magnetized magnetic layers

using spin torque from the spin Hall effect," *Physical Review Letters*, vol. 109, no. 9, p. 096602, 2012.

[142] M. Ali, C. Marrows, and B. Hickey, "Onset of exchange bias in ultrathin antiferromagnetic layers," *Physical Review B*, vol. 67, no. 17, p. 172405, 2003.

[143] J. Sort, B. Dieny, M. Fraune, C. Koenig, F. Lunnebach, B. Beschoten, and G. Güntherodt, "Perpendicular exchange bias in antiferromagnetic-ferromagnetic nanostructures," *Applied Physics Letters*, vol. 84, no. 18, pp. 3696–3698, 2004.

[144] N. Aley, G. Vallejo-Fernandez, R. Kroeger, B. Lafferty, J. Agnew, Y. Lu, and K. O'Grady, "Texture effects in IrMn/CoFe exchange bias systems," *IEEE Transactions on Magnetics*, vol. 44, no. 11, pp. 2820–2823, 2008.

[145] R. Jungblut, R. Coehoorn, M. Johnson, J. Aan de Stegge, and A. Reinders, "Orientational dependence of the exchange biasing in molecular-beam-epitaxy-grown $Ni_{80}Fe_{20}/Fe_{50}Mn_{50}$ bilayers," *Journal of Applied Physics*, vol. 75, no. 10, pp. 6659–6664, 1994.

[146] C.-J. Lin, G. Gorman, C. Lee, R. Farrow, E. Marinero, H. Do, H. Notarys, and C. Chien, "Magnetic and structural properties of Co/Pt multilayers," *Journal of Magnetism and Magnetic Materials*, vol. 93, pp. 194–206, 1991.

[147] M. Wormington, C. Panaccione, K. M. Matney, and D. K. Bowen, "Characterization of structures from x-ray scattering data using genetic algorithms," *Philosophical Transactions of the Royal Society of London A: Mathematical, Physical and Engineering Sciences*, vol. 357, no. 1761, pp. 2827–2848, 1999.

[148] S. Dutta, K. Sankaran, K. Moors, G. Pourtois, S. Van Elshocht, J. Bömmels, W. Vandervorst, Z. Tőkei, and C. Adelmann, "Thickness dependence of the resistivity of platinum-group metal thin films," *Journal of Applied Physics*, vol. 122, no. 2, p. 025107, 2017.

[149] M. Ali, C. H. Marrows, M. Al-Jawad, B. J. Hickey, A. Misra, U. Nowak, and K.-D. Usadel, "Antiferromagnetic layer thickness dependence of the IrMn/Co exchange-bias system," *Physical Review B*, vol. 68, no. 21, p. 214420, 2003.

[150] T. Ambrose and C. Chien, "Finite-size effects and uncompensated magnetization in thin antiferromagnetic CoO layers," *Physical Review Letters*, vol. 76, no. 10, p. 1743, 1996.

[151] T. Ambrose and C. Chien, "Dependence of exchange coupling on antiferromagnetic layer thickness in NiFe/CoO bilayers," *Journal of Applied Physics*, vol. 83, no. 11, pp. 6822–6824, 1998.

[152] C. Binek, "Training of the exchange-bias effect: A simple analytic approach," *Physical Review B*, vol. 70, no. 1, p. 014421, 2004.

[153] T. Hauet, J. Borchers, P. Mangin, Y. Henry, and S. Mangin, "Training effect in an exchange bias system: The role of interfacial domain walls," *Physical Review Letters*, vol. 96, no. 6, p. 067207, 2006.

[154] R. Khan, P. Shepley, A. Hrabec, A. Wells, B. Ocker, C. Marrows, and T. Moore, "Effect of annealing on the interfacial Dzyaloshinskii-Moriya interaction in Ta/CoFeB/MgO trilayers," *Applied Physics Letters*, vol. 109, no. 13, p. 132404, 2016.

[155] S. Woo, K. Litzius, B. Krüger, M.-Y. Im, L. Caretta, K. Richter, M. Mann, A. Krone, R. M. Reeve, M. Weigand, *et al.*, "Observation of room-temperature magnetic skyrmions and their current-driven dynamics in ultrathin metallic ferromagnets," *Nature Materials*, vol. 15, no. 5, p. 501, 2016.

[156] X. Ma, G. Yu, C. Tang, X. Li, C. He, J. Shi, K. L. Wang, and X. Li, "Interfacial Dzyaloshinskii-Moriya Interaction: Effect of 5*d* band filling and correlation with spin mixing conductance," *Physical Review Letters*, vol. 120, no. 15, p. 157204, 2018.

[157] Brilloiun light scattering spectroscopy measurements were performed by H. T. Nembach and J. M. Shaw, Quantum Electromagnetics Divi-

sion, National Institute of Standards and Technology, Boulder, Colorado 80305, USA.

[158] M. A. Schoen, J. Lucassen, H. T. Nembach, T. Silva, B. Koopmans, C. H. Back, and J. M. Shaw, "Magnetic properties of ultrathin 3d transition-metal binary alloys. I. spin and orbital moments, anisotropy, and confirmation of slater-pauling behavior," *Physical Review B*, vol. 95, no. 13, p. 134410, 2017.

[159] W. Antel, F. Perjeru, and G. Harp, "Spin structure at the interface of exchange biased FeMn/Co bilayers," *Physical Review Letters*, vol. 83, no. 7, p. 1439, 1999.

[160] J. R. Taylor, *An introduction to error analysis: Mill Valley*. California, University Science Books, 1982.

[161] J.-P. Tetienne, T. Hingant, L. Martínez, S. Rohart, A. Thiaville, L. H. Diez, K. Garcia, J.-P. Adam, J.-V. Kim, J.-F. Roch, *et al.*, "The nature of domain walls in ultrathin ferromagnets revealed by scanning nanomagnetometry," *Nature Communications*, vol. 6, p. 6733, 2015.

[162] K. Zeissler, M. Mruczkiewicz, S. Finizio, J. Raabe, P. Shepley, A. Sadovnikov, S. Nikitov, K. Fallon, S. McFadzean, S. McVitie, *et al.*, "Pinning and hysteresis in the field dependent diameter evolution of skyrmions in Pt/Co/Ir superlattice stacks," *Scientific reports*, vol. 7, no. 1, p. 15125, 2017.